# Forced Convective Heat Transfer of Nitrate Salts at High Reynolds Numbers and High Heat Flux in a Smooth and a Spirally Grooved Tube

Experimentelle Analyse der erzwungenen konvektiven Wärmeübertragung von Nitratsalzen bei hohen Reynoldszahlen und hohen Wärmeströmen in einem glatten und einem spiralförmig gedrallten Rohr

Von der Fakultät für Maschinenwesen der Rheinisch-Westfälischen Technischen Hochschule Aachen zur Erlangung des akademischen Grades einer Doktorin der Ingenieurwissenschaften genehmigte Dissertation

vorgelegt von

Cathy Martine Lina Frantz

Berichter:

Univ.-Prof. Dr.-Ing. Bernhard Hoffschmidt

Univ.-Prof. Dr.-Ing. Reinhold Kneer

Tag der mündlichen Prüfung: 23.05.2025

Diese Dissertation ist auf den Internetseiten der Universitätsbibliothek online verfügbar.

*Those who fall in love with practice without science are like a sailor who steers a ship without a helm or compass, and who never can be certain wither he is going.*

Leonardo da Vinci

*It is easier to write ten volumes on theoretical principles than to put one principle into practice.*

Leo Tolstoy

# *Abstract*

**Forced convective heat transfer of nitrate salts at high Reynolds numbers and high heat flux in a smooth and a spirally grooved tube**

by Cathy Frantz

The forced convective heat transfer of a molten nitrate salt in a circular smooth tube and a spirally grooved tube is experimentally investigated using a water-cooled induction heater.

The novel experimental setup is first validated using water as the main fluid, as its heat transfer is well-known. The final experiments for both tubes are carried out with the so-called nitrate salt "Solar Salt" (60% $NaNO_3$ 40% $KNO_3$) at fluid bulk temperatures ranging between 300 °C and 550 °C. Consequently, Prandtl numbers range from 10 to 3.7.

For the smooth tube experiments, the salt mass flow is varied to cover Reynolds numbers ranging from 14000 up to 222000. Furthermore, the experiments are conducted with different heat fluxes ranging between 330 kW/m² up to 930 kW/m². To investigate the impact of local overheating of the salt above its chemical stability limit (i.e. 600 °C), the mean Nusselt number is evaluated for inner wall temperatures up to 633 °C. Mean Nusselt numbers are reported and compared to the well-known Gnielinski correlation.

The measurements for the spirally grooved tube are carried out for a tube with a relative groove height $e/d_i$=0.017, a relative groove pitch $p/d_i$ =0.913 and groove angle α=73.8° using the same water-cooled induction heater setup. The data is provided for Reynolds numbers ranging between 11000 up to 285000 and for flux densities between 330 and 930 kW/m². The setup achieves inner wall temperatures up to 633 °C, thus providing data on the behavior of the forced convective heat transfer as a function of inner wall temperature. The mean Nusselt number and friction factor as a function of Reynolds and Prandtl number are reported and compared to the measurement results yielded with the circular smooth tube as well as correlations and data from the literature.

# *Kurzfassung*

**Erzwungene konvektive Wärmeübertragung von Nitratsalzen bei hohen Reynoldszahlen und hohen Wärmeströmen in einem glatten und einem spiralförmig gedrallten Rohr**

von Cathy Frantz

Der erzwungene konvektive Wärmeübergang von flüssigem Nitratsalz in einem kreisförmigen Glattrohr und einem spiralförmig mit Nuten versehenem Rohr wird experimentell mithilfe eines Testaufbau mit einem wassergekühlten Induktionsheizer untersucht.

Der neuartige Versuchsaufbau wird zunächst mit Wasser als Wärmeübergangsmedium validiert, da der erzwungene konvektive Wärmeübergang von Wasser in Glattrohren bekannt ist. Die Versuche für beide Rohrtypen werden anschließend mit dem binären Nitratsalz "Solar Salt" (60% $NaNO_3$ 40% $KNO_3$) bei mittleren Fluidtemperaturen zwischen 300 °C und 550 °C durchgeführt. Folglich reichen die Prandtl-Zahlen von 10 bis 3.7.

Innerhalb der Glattrohrexperimente werden durch Variation des mittleren Salzmassenstroms Reynoldszahlen von 14000 bis 222000 abgedeckt. Darüber hinaus werden die Experimente mit Wärmeströmen zwischen 330 kW/m² und 930 kW/m² durchgeführt. Um den Einfluss einer lokalen Überhitzung des Salzes über seine chemische Stabilitätsgrenze (d.h. 600 °C) zu untersuchen, wird die mittlere Nusselt-Zahl für Innenwandtemperaturen bis 633 °C ausgewertet. Als Ergebnis wird die mittlere Nusselt-Zahl ermittelt und mit der aus der Literatur bekannten Gnielinski-Korrelation verglichen.

Des Weiteren wird mit dem gleichen Aufbau der erzwungene konvektive Wärmeübergang von Solar Salt in einem spiralförmig gedrallten Rohr mit einer relativen Drallhöhe $e/d_i$=0.017, einem relativen Rippenabstand von $p/d_i$=0.913 und einem Drallwinkel $\alpha$=73.8° untersucht. Die Versuche werden für Reynolds-Zahlen zwischen 11000 und 285000 und für Flussdichten zwischen 330 kW/m² und 930 kW/m² durchgeführt. Mit dem Aufbau werden Innenwandtemperaturen von bis zu 633 °C erreicht, wodurch eine erweiterte Datenbasis über das Verhalten des erzwungenen konvektiven Wärmeübergangs in Abhängigkeit von der Innenwandtemperatur gewonnen wird. Ergebnis der Untersuchung sind die mittlere Nusselt-Zahl und der Widerstandsbeiwert in Abhängigkeit von Reynolds- und Prandtl-Zahl und der Abgleich mit den Messergebnissen aus den Glattrohrversuchen, sowie mit Korrelationen und Daten aus der Literatur.

# *Acknowledgements*

This work has been funded by the “German Federal Ministry for Economic Affairs and Climate Action” (0324327A)

Federal Ministry
for Economic Affairs
and Climate Action

I would also like to take this opportunity to thank everyone involved for their great support:

Prof. Hoffschmidt for the supervision and invaluable advice during my PhD study.

Prof. Pitz-Paal and Prof. Sattler for their important comments.

Reiner and Marc, who made sure by their many inquiries that I did justice to the scientific claim of this work.

The HPMS-II work package 4 team: Sven, Stefan & Peter, who supported me very actively from the first drawing to the plant operation.

Thomas and Christian, who provided me with the TESIS:com plant.

Miriam who kept my financial and scheduling back.

Fabio, who organized even the most complicated business trip marathon absolutely flawlessly, so that I always had a roof over my head.

My parents Edith and Jean-Marc, who enabled me to receive a great education, without which this work would never had been possible.

Finally, I would like to express my gratitude to my husband Fabian. Without his tremendous understanding and encouragement in the past few years, it would have been impossible for me to complete this thesis.

Thank you!

# Table of Contents

**1 Introduction 1**

**2 Fundamentals 3**

2.1 Conduction ... 3

2.2 Convection ... 3

2.3 Friction Factor ... 8

2.4 Induction Heating ... 9

**3 State of the Art 13**

3.1 Conditions in Central Solar Receiver Absorber Tubes ... 13

3.2 Forced Convective Heat Transfer in Circular Smooth Tubes ... 16

3.3 Forced Convective Heat Transfer in Enhanced Tubes ... 20

3.4 Solar Salt Decomposition ... 25

3.5 Material Properties ... 28

**4 Experimental Setup and Evaluation 36**

4.1 Selection of Heating Concept ... 36

4.2 Experimental Setup ... 43

4.3 Deduction of Nusselt Number ... 47

4.3.1 Calorimetric method ... 49

4.3.2 Electrical method ... 51

4.4 Reference Nusselt Number ... 53

4.5 Deduction of Friction Factor ... 54

4.6 Test Procedure and Measurement Plan ... 55

4.7 Uncertainty analysis ... 57

4.7.1 Results Uncertainty Analysis of the Water Setup ... 57

4.7.2 Results Uncertainty Analysis of the Solar Salt Setup ... 59

**5 Results and Discussion 62**

5.1 Validation experiments with water ... 62

5.2 Smooth circular tube with Solar Salt ... 63

5.3 Spirally grooved tube with Solar Salt ..... 68
5.3.1 Nusselt number ..... 68
5.3.2 Friction factor ..... 73

**6 Conclusion** **77**

**7 Bibliography** **79**

**Appendix** **89**

A. Flow Conditions in Central Solar Receivers ..... 92

B. Thermophysical Properties of Water and Test Tube ..... 93
B.1. Thermophysical Properties of Liquid Water ..... 93
B.2. Thermophysical Properties of the Test Tube ..... 94

C. Preliminary Experiments ..... 97
C.1. Single electrode experiment ..... 97
C.2. Cyclic voltammetry experiment ..... 98

D. Test Setup and Test Matrix ..... 100
D.1. Test Section ..... 100
D.2. Solar Salt Test Setup ..... 101
D.3. Water Test Setup ..... 106

E. Enhanced tube geometry ..... 109

F. Measurement equipment and uncertainty ..... 112
F.1. Assumptions for Uncertainty of Outer Wall Tube Temperature $T_{t,o}$ ... 112
F.2. Assumptions for Uncertainty of Main Fluid Mass Flow in Salt Setup . 114
F.3. Assumptions for Uncertainty of Phase Angle $\varphi$ ..... 118

G. Additional calculations ..... 120
G.1. Heating of the Solar Salt and water in the test section through induction heating ..... 120
G.2. Impact of Transient Heat Conduction ..... 121
G.3. Deduction of Peripheral Pressure Difference $\Delta p_{per}$ ..... 123

# List of Figures

Figure 2-1: Definition of cylindrical coordinates ..... 3

Figure 2-2: Velocity boundary layer development on a flat plate [14] ..... 5

Figure 2-3: Velocity (bottom) and thermal (top) boundary layer development in a tube (laminar flow) ..... 6

Figure 2-4: Comparison of prediction of mean Nusselt number by the Gnielinski and Sieder-Tate correlation with the Dittus-Boelter equation for different assumptions of Re, Pr and film temperatures [22] ..... 8

Figure 2-5: Friction factor for fully developed flow in a circular tube [22] ..... 9

Figure 2-6: Schematic illustration of the magnetic field and current induced by a solenoid coil carrying an AC current in a cylindrical workpiece [23] ..... 10

Figure 2-7: Qualitative variation of the current, the strength of the magnetic field and the eddy current induced in a conductive workpiece (sleeve) induced by a solenoid coil carrying an AC current. ..... 10

Figure 2-8: Distribution of relative current density $J/J_{t,o}$ and relative power density $w/w_{t,o}$ as a function of distance from the workpiece surface for a semi-infinite body [25] ..... 11

Figure 2-9: Current density distribution $J_r/J_{t,o}$ in a solid cylinder as a function of normalised radius for different relative outer radius $r_o$. The dashed line shows the distribution expected for a semi-infinite body [23] ..... 11

Figure 3-1: Left: Solar Two molten salt Receiver, Daggett, California [27]; Right: Schematic structure of receiver panel [2] ..... 13

Figure 3-2: Exemplary mean and peak flux density of a 140 and 700 $MW_{th}$ external receiver (operation with full solar load) [10] ..... 15

Figure 3-3: Reynolds number range of experimental data for the forced convective heat transfer of molten salts in circular tubes by author and salt type. The dashed box represents the receiver design space [22] ..... 20

Figure 3-4: Left: Geometry definition of spirally grooved tube; Right: Specimen of the test tube used in this work [59] ..... 21

Figure 3-5: Left: Nusselt number ratio Nua/Nu0 of different authors [56], [73], [74], [75] compared to the respective ratios predicted by the general correlation of Ravigururajan [7] (equation (3.2)). Right: friction factor ratio ζa/ζ0 of different authors [74] and [75]

compared to the respective ratios predicted by the general correlation of Ravigururajan [7] (equation (3.1)) (adapted from [59]) ..... 24

Figure 3-6: Corrosion rates of several Ni-base alloys (left) and austenitic steels (right) in Solar Salt as a fucntion of temperature [84] ..... 27

Figure 3-7: Specific heat capacity as a function of temperature for different compositions of $NaNO_3$-$KNO_3$ [92] ..... 29

Figure 3-8: Specific heat capacity Solar Salt – Left: Values from the literature as a function of temperature; Right: Mean specific heat capacity over the full temperature range by author. For values marked with (*) no uncertainty of measurement is stated and ±10% is assumed (adapted from [22]) ..... 31

Figure 3-9: Density of Solar Salt as a function of temperature for various authors [22] ..... 32

Figure 3-10: Dynamic viscosity of nitrate salt as a function of salt temperature: data marked with (*) are for equimolar $NaNO_3$-$KNO_3$; other data are for Solar Salt [22] ..... 34

Figure 3-11: Specific electrical resistivity for two different compositions of $NaNO_3$ and $KNO_3$ according to [95] and Solar Salt as a function of temperature ..... 35

Figure 4-1: Hydrogen and nickel oxide formation in single electrode water test ..... 37

Figure 4-2: Measurement results of single electrode water test. Left: Total measured current as a function of applied potential difference for three different saline solutions. Right: Measured additional current as a function of salt concentration for different applied voltages ..... 38

Figure 4-3: Results of cyclic voltammetry experiment with Alloy625 electrodes and Solar Salt ..... 39

Figure 4-4: Left: Alloy625 electrodes before and after cyclic voltammetry test; Right: Solar Salt after cyclic voltammetry test before completely freezing ..... 39

Figure 4-5: Schematic representation of the main test section ..... 43

Figure 4-6: Overview of corrosion rates of steel types 1.4878 and 1.4541 in Solar Salt as a function of immersion time of different authors [110], [111], [112] ..... 44

Figure 4-7: Simplified piping and instrumentation diagram of the experimental system Solar Salt loop ..... 46

Figure 4-8: molten salt test setup with generator, induction heater and heat rejection ..... 46

Figure 4-9: Position and boundary condition of differential control volume $dr \cdot rd\theta \cdot dx$ ..... 47

Figure 4-10: Heat flows and system boundaries of the energy balance according to the "calorimetric method" [22] ..... 50

Figure 4-11: Heat flows and system boundaries of the energy balance according to the "electrical method" ..... 52

Figure 4-12: Exemplary distribution of uncertainty contributions of σNumcal for water test (calorimetric method, test case WAT_m2_q700 [IV]) ..... 58

Figure 4-13: Exemplary distribution of uncertainty contributions of σNumel for water test (electrical method, test case WAT_m2_q700 [IV]) ..... 58

Figure 4-14: Exemplary distribution of uncertainty contributions of σNumcal for salt test [V] (calorimetric method, test case SALT_SG_T300_m3_q700) ..... 60

Figure 4-15: Exemplary distribution of uncertainty contributions of σNumel for water test [V] (electrical method, test case SALT_SG_T300_m3_q700) ..... 60

Figure 5-1: Normalized Nusselt number as a function of Reynolds number of the validation tests with water compared to the Gnielinski correlation (Re: 43000 to 305000, Pr: 4 to 9) [22] ..... 62

Figure 5-2: Measured Nusselt number compared to the Nusselt number predicted by the Gnielinski correlation of the validation tests with water (Re: 43000 to 305000, Pr: 4 to 9) [22] ..... 63

Figure 5-3: Measured mean Nusselt number of Solar Salt as a function of Reynolds number and salt temperature (Re: 14000 to 222000; Pr: 3.8 to 10) and values expected by Gnielinski for 3 different Prandtl numbers [22] ..... 64

Figure 5-4: Deviation of power transferred to tube using the calorimetric and the electrical method as a function of Re (Re: 14000 to 222000; Pr: 3.8 to 10) [22] ..... 64

Figure 5-5: Normalized mean Nusselt number of Solar Salt as a function of Re number for all salt temperatures (Re: 14000…222000; Pr: 3.8…10) ..... 65

Figure 5-6: Mean measured Nusselt number of Solar Salt over mean expected Nusselt number (Gnielinski) for different salt temperatures (Re: 14000 to 222000; Pr: 3.8 to 10) [22] ..... 66

Figure 5-7: Mean measured Nusselt number as a function of predicted Nusselt number for bulk salt temperatures at 550°C (Re: 25000 to 220000, Pr≈4) [22] ..... 67

Figure 5-8: Deviation of measured mean Nu number from expected mean Nusselt number calculated by Gnielinski as a function of the inner wall temperature (Re: 14000 to 222000; Pr: 3.8 to 10) [22] ..... 67

Figure 5-9: Mean Nusselt number of Solar Salt as a function of Reynolds number and salt temperature (Re: 11000 to 285000; Pr: 3.7 to 10) and values calculated with equation (5.2) assuming a constant Prandtl and inner wall temperature [59] ..... 69

Figure 5-10: Deviation of power transferred to tube using the calorimetric and the electrical method as a function of Re (Re: 11000 to 285000; Pr: 3.7 to 10) [59] ..... 69

Figure 5-11: Measured mean Nusselt number of Solar Salt as a function of mean Nusselt number predicted by Gnielinski correlation (Re: 11000 to 285000; Pr: 3.7 to 10) [59] ..... 70

Figure 5-12: Measured mean Nusselt number and mean Nusselt number predicted by several correlations as a function of the Nusselt number predicted by equation (5.2) (Re: 11000…285000; Pr: 3.7…10) [59] ..... 71

Figure 5-13: Measured and expected Nusselt number ratio NuaNu0 of two different authors as a function of Reynolds number (Re: 11000 to 285000; Pr: 3.7 to 10) [59] ..... 72

Figure 5-14: Deviation of measured mean Nu number (spirally grooved tube) from the Gnielinski mean Nusselt number (smooth tube) as a function of the inner wall temperature (Re: 11000…285000; Pr: 3.7…10) ..... 73

Figure 5-15: Pressure difference over test section as a function of salt temperature for a smooth and the spirally enhanced tube (Re: 11000 to 285000; Pr: 3.7 to 10) (adapted from [59]) ..... 74

Figure 5-16: Friction factor of smooth and spirally grooved tube and respective fitted power functions as a function of Reynolds number [59] ..... 75

Figure 5-17: Friction factor ratio deduced by two approaches from the measurement data and by a general correlation as a function of Reynolds number [59] ..... 76

# List of Tables

Table 2-1: Convection correlations for turbulent flow in a smooth circular tube ..... 7

Table 3-1: State of the art conditions in Central Solar Receiver Absorber Tubes ..... 16

Table 3-2: Correlations and geometric specifications from literature..... 24

Table 3-3: Basic properties Solar Salt..... 28

Table 3-4: Reported mean specific heat capacities by several authors ..... 30

Table 4-1: Overview of selection criteria of heating concepts..... 42

Table 4-2: Geometric specification main test section ..... 45

Table 4-3: Goal test matrix molten salt test setup with smooth and spirally grooved tube..... 56

Table 4-4: Overview of range of main measurement quantities and derived quantities ..... 56

Table 4-5: Summary of combined measurement uncertainty of the water setup ..... 59

Table 4-6: Summary of combined measurement uncertainty of the Solar Salt setup ..... 61

# List of Symbols and Indices

| Symbol | Unit | Definition |
|---|---|---|
| $\boldsymbol{B}$ | (T) | Magnetic flux density (vector field) |
| $c_p$ | (J/(kg·K)) | Specific heat capacity |
| $\boldsymbol{D}$ | (C/m²) | Electric displacement field |
| d | (m) | Diameter of test section tube |
| $\boldsymbol{E}$ | (V/m) | Electric field strength (vector field) |
| $e$ | (m) | Groove height enhanced tube |
| $f$ | (Hz) | Frequency of AC current |
| $\boldsymbol{H}$ | (A/m) | Magnetic field strength (vector field) |
| h | (W/(m²·K)) | Convective heat transfer coefficient |
| $I_{RMS}$ | (A) | Root mean square current |
| $J$ | (A/m²) | Current density |
| $K$ | (mm) | Roughness factor |
| $L_{e,h}$ | (m) | Hydraulic entrance length |
| $L_{e,th}$ | (m) | Thermal entrance length |
| $l_{heat}$ | (m) | Heating length |
| $\dot{m}$ | (kg/s) | Mass flow |
| $Nu_m$ | (-) | Mean Nusselt number over heating section |
| $Nu_x$ | (-) | Nusselt number at the axial location x |
| $Pe$ | (-) | Péclet number |
| $P_{el}$ | (W) | Active power |
| $Pr$ | (-) | Prandtl number at bulk temperature |
| $Pr_{t,i}$ | (-) | Prandtl number at inner tube wall temperature ($r$=$r_i$) |
| $p$ | (m) | Groove pitch enhanced tube |
| $\dot{q}$ | (W/m²) | Flux density |
| $R$ | (J/(K·mol)) | Universal gas constant (8.31441 J/K/mol [1]) |
| $Re$ | (-) | Reynolds number |
| $r$ | (m) | radial coordinate of cylindrical coordinate system (see Figure 2-1) |
| $r_i;\ r_o$ | (m) | i: inner radius tube test section; o: outer radius tube test section |
| $r_{ind}$ | (m) | Inner radius of inductor coil |

| Symbol | Unit | Definition |
|---|---|---|
| $\boldsymbol{S}$ | (W/m²) | Poynting vector |
| $T$ | (°C) | Temperature |
| $t$ | (m) | Thickness |
| $U_{RMS}$ | (V) | Root mean square voltage |
| $\bar{u}$ | (m/s) | Mean velocity of the flow over cross-sectional area |
| $V$ | (m³) | Volume |
| $\dot{V}$ | (m³/s) | Volumetric flow rate |
| $w$ | (W/m³) | Volumetric heating density of the tube |
| $x$ | (m) | Axial coordinate of cylindrical coordinate system (see Figure 2-1) |

## Greek Letters

| Symbol | Unit | Definition |
|---|---|---|
| $\alpha$ | (°) | Pitch angle enhanced tube |
| $\beta$ | (°) | contact angle of the roughness profile (see Figure 3-4) |
| $\Delta\vartheta_{ln}$ | (K) | Logarithmic temperature difference |
| $\Delta p$ | (Pa) | Pressure difference |
| $\delta$ | (m) | Penetration depth |
| $\zeta$ | (-) | Friction factor |
| $\theta$ | (rad) | azimuth coordinate of cylindrical coordinate system (see Figure 2-1) |
| $\lambda$ | (W/(m·K)) | Thermal conductivity |
| $\mu_0$ | (H/m) | permeability of vacuum: $4\pi \times 10^{-7}$ H/m |
| $\mu_r$ | (-) | Relative magnetic permeability |
| $\nu$ | (m²/s) | Kinematic viscosity |
| $\rho$ | (kg/m³) | Density |
| $\rho_{el}$ | (Ωm) | Electrical resistivity |
| $\sigma$ | (unit) | Measurement uncertainty at unit of measurand (Gaussian distribution) |
| $\varphi$ | (rad) | Phase angle |

## Subscripts

| Subscripts | Definition |
|---|---|
| 0 | smooth tube |
| a | enhanced tube |
| cw | Cooling water |
| $calibration$ | After calibration |
| i | property at inner radius tube test section |
| in | property at flow inlet |
| ins | Insulation between test tube and induction heater |
| m | Mean convective heat transfer coefficient or Nusselt number |
| meas | Measurement equipment uncertainty (Type B) |
| o | property at outer radius tube test section |
| out | property at flow outlet |
| RADAR | Radar level sensor |
| RMS | Root mean square |
| read | Measurement reading uncertainty (Type A) |
| s | Solar Salt (60 wt-% $NaNO_3$, 40 wt-% $KNO_3$) |
| t | Test tube |
| UFM | Ultrasonic flow meters |
| weld | Laser weld |
| x | axial position along heating section where property is measured |
| ∞ | Ambient conditions |

## Superscripts

| Subscripts | Definition |
|---|---|
| cal | Calorimetric method |
| el | Electrical method |

# 1 Introduction

Over the last 70 years, extensive operational experience has been accumulated with molten salts as heat transfer fluid and storage medium in commercial heat-treating and industrial process plants [2]. Common industrial applications include advanced nuclear reactors, chemical processing, energy storage and concentrated solar power generation (CSP) [3]. Most recent project developments in CSP systems suggest that central receiver systems with nitrate salts as a heat transfer fluid have become an industry standard. Solar thermal power plants can play an important role in the future international energy supply because of their ability to integrate cost-effective thermal storage and thereby dispatch electricity on demand decoupled from the fluctuating solar resource [4]. CSP systems consist of large reflectors, which concentrate sunlight on a heat exchanger, the receiver. Inside the receiver, the solar salt flows through so-called absorber tubes and is heated by the solar radiation. These plants most commonly use a binary mixture of 60 wt-% sodium nitrate ($NaNO_3$) and 40 wt-% potassium nitrate ($KNO_3$), commonly called “Solar Salt”. This molten salt is solid at ambient temperature, non-toxic and non-flammable and has its melting point at roughly 238 °C. Solar Salt exposes a low thermal conductivity, which minimizes heat losses in thermal storage applications. However, the same property leads to low forced convective heat transfer coefficients in heat exchangers, which reduces the allowable heat fluxes and therefore increases heat exchanger area and investment costs.

To mitigate the low conductivity, high flow velocities are employed in nitrate salt tubular heat exchangers, which causes high pressure drops and pumping costs. Central receivers with molten salt as heat transfer fluid operate at relatively high Reynolds numbers; ranging from 10’000 to more than 200000 [5]. Another approach to increase the heat transfer, besides increasing the bulk fluid velocity in the absorber tubes, is to enhance the convective heat transfer by the usage of passive augmentation methods [6]. Passive methods to enhance the forced convective heat transfer in a tube have been employed in various industrial fields such as desalination or power plant condensers and have been widely investigated in the literature [7]. The main idea behind the different augmentation methods is the disturbance of the existing boundary layer, which – for the right set of geometric parameters – can lead to an advantageous increase in heat transfer compared to the increase in pressure drop.

The forced convective heat transfer in circular tubes has been extensively studied for common fluids such as water, air or oil and general correlations exist for the Reynolds number and Prandtl number region relevant for solar heat exchangers. However, the available experimental data on the forced convective heat transfer of molten salt in circular tubes for Reynolds numbers above 50000 is rather limited (see chapter 3 ). Only two studies have experimentally investigated this Reynolds number region. Both studies measured lower values than expected by general correlations. The results of one of these studies would imply an underestimation of temperature levels in heat exchanger tubes and molten salt between 20 K and up to more than 100 K, leading to degradation, corrosion and ultimately premature failure of heat exchangers.

For enhanced tubes, general correlations are also available for the relevant Reynolds number and Prandtl number range. However, the available experimental data for molten salts is limited to Reynolds numbers up to 30000. This is also considerably lower than the required Reynolds number. Compared to the experimental data available for molten salt, the general correlations overpredict the measured Nusselt number ratio by up to 90% and the friction factor ratio by up to a factor of two.

Current state of the art molten salt systems based on nitrate salts are limited to an upper salt bulk temperature of 565 °C and maximum film temperature of 600 °C [8]. This upper temperature limit is set to minimize decomposition reactions of the salt, that affect both the thermal properties of the salt and limit corrosion towards container materials [9]. However, a higher upper cycle temperature promises to decrease the levelized cost of electricity (LCOE), mainly driven by smaller storage and steam generator size, as well as a higher turbine efficiency [10]. There is concern that higher bulk and film temperature may lead to localized decomposition of the nitrate salt in the film region with formation of gaseous products. The gases might form a local vapor layer with low thermal conductivity and could negatively impact the convective heat transfer of Solar Salt in heat exchanger tubes. A decrease of convective heat transfer would then cause an increase in film temperatures and would probably entail further acceleration of the decomposition process. The geometry of enhanced tubes does not only cause a local increase of fluid velocity but can also induce wakes and low-speed recirculation zones involving a local decrease in fluid velocity [8]. This could cause local overheating, entail local salt degradation and consequently negatively impact the overall convective heat transfer. Another important effect for both tube types is the formation of an oxide-based corrosion layer on the metal surface in the heating zone driven by the high film temperatures. This oxide layer would entail an increase in outer wall temperatures of the heated section if the same heat rate is transferred to the fluid. So far no to little experimental research data exists that specifically addresses the high temperature, high Reynolds number forced convective heat transfer of Solar Salt in smooth and spirally grooved tubes.

Therefore, this study addresses the forced convective heat transfer of Solar Salt at Reynolds numbers up to 200000 in circular smooth and an enhanced tube as well as the impact of film temperatures above the chemical stability limit of Solar Salt of 600 °C stated in the literature.

# 2 Fundamentals

This chapter introduces all energy transport mechanisms as well as key figures, which are relevant in this work.

## 2.1 Conduction

Conduction is a mechanism of energy transport. In a solid, conduction is attributed to the atomic activity in the form of lattice vibrations or lattice waves induced by atomic motion. According to the second law of thermodynamics, heat always flows in the direction towards lower temperatures. The thermal power transferred by thermal conduction is described by Fourier's law. Equation (2.1) shows the general form of Fourier's law in cylindrical coordinates for an isotropic material and Figure 2-1 shows the definition of the cylindrical coordinates.

$$\dot{q} = -\lambda \nabla T = -\lambda \left( \boldsymbol{i} \frac{\partial T}{\partial r} + \boldsymbol{j} \frac{1}{r} \frac{\partial T}{\partial \theta} + \boldsymbol{k} \frac{\partial T}{\partial x} \right) \tag{2.1}$$

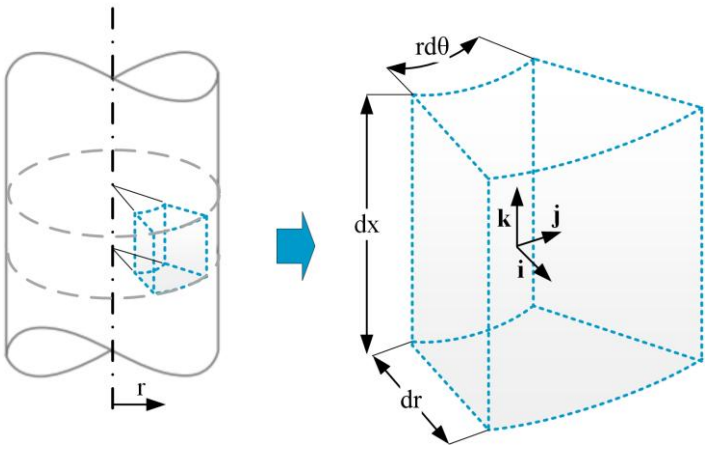


Figure 2-1: Definition of cylindrical coordinates

## 2.2 Convection

The convection heat transfer mechanisms can be categorized into two main mechanisms: the first mechanism is caused by energy transfer due to random molecular motion – the so-called diffusion. The second mechanism is the energy transferred by the macroscopic – the bulk – motion of the fluid, where large number of molecules are moving collectively (advection). The total heat transfer is composed of a superposition of energy transport by both the random motion of molecules and by the bulk motion of the fluid. The combination of both transport mechanisms is called convection. This work focusses on the convective heat transfer, which occurs between a fluid in motion and a boundary surface, when both are at different temperatures.

Convective heat transfer can be classified according to the nature of the flow: the first class being natural or free convection, where the flow along the boundary surface is induced by buoyancy forces, caused by density differences due to temperature gradients within the fluid. The second

class, which is of interest in this work, is called forced convection, where the flow is caused by external means. In this case advection and diffusion of heat dominate over buoyancy forces.

In 1883, Reynolds [11] showed that two main forms of flow exist: laminar and turbulent flow. In the case of laminar flow, the individual flow threads run side by side in an orderly fashion. In turbulent flow, the individual flow threads are intertwined in a time-dependent, irregular manner, and the individual fluid elements perform a three-dimensional, stochastic oscillating motion about their mean flow path (see Figure 2-2). This mixing process increases the frictional resistance and the heat exchange of turbulent flows. The transition from laminar to turbulent flow is commonly described by the dimensionless Reynolds number. Reynolds was the first to state that laminar flow becomes turbulent at a certain critical value of the Reynolds number. Equation (2.2) shows the Reynolds number definition for tube flow.

$$Re \equiv \frac{\bar{u} \cdot d_i}{\nu} \tag{2.2}$$

In this equation $\bar{u}$ is the mean velocity of the flow over the cross-sectional area of the tube. It is widely accepted that for $Re > 10'000$, fully developed turbulent flow conditions are present [12]. Another important dimensionless parameter is the Prandtl number as defined below:

$$Pr \equiv \frac{\nu}{a} = \frac{\nu \cdot \rho \cdot c_\mathrm{p}}{\lambda} \tag{2.3}$$

The Prandtl number is defined as the ratio of kinematic viscosity and thermal diffusivity. The Prandtl number of gases is roughly 1. This means, that both momentum and heat dissipate at the same rate. Solar Salt exposes a Prandtl number >1, hence heat diffuses slowly in this medium. Finally, the Péclet number is used to describe the ratio of advective to diffusive heat transfer rates:

$$Pe \equiv Re \cdot Pr \tag{2.4}$$

For Pe>>1, advective heat transfer is predominant over diffusive heat transfer.

Laminar flow can be described analytically, which allows the description of boundary layers, heat transfer and friction factors through analytical correlations [13]. An exclusively analytical treatment of the heat and mass transfer of a turbulent pipe flow failed so far because neither the turbulent shear stresses, nor the turbulent heat flux density nor the turbulent diffusion flux density can be determined in a purely theoretical way. Therefore, friction factors and heat transfer properties of turbulent pipe flow must be analyzed based on experiments or numerically [13]. In this work, flow conditions at $Re > 10'000$ are studied. Hence, all further considerations relate to turbulent flow conditions.

Because of the viscosity of the fluid, no relative movement occurs between the fluid and the wall at the contact location of fluid and wall. Consequently, a boundary layer forms in the direct proximity of the wall in which the velocity is reduced from free stream velocity to the surface velocity – the so-called velocity boundary layer. Likewise, a thermal boundary layer will form if the surface and free stream temperature differs. The velocity boundary layer is characterized by the presence of velocity gradients and shear stresses. The thermal boundary layer is characterized by temperature gradients and heat transfer [14].

Three different regions can be distinguished within the turbulent boundary layer as a function of distance from the wall surface (see Figure 2-2). In the viscous sublayer, transport is dominated by diffusion and the velocity profile is nearly linear. In the adjoining buffer layer diffusion and turbulent mixing are comparable [14]. In the turbulent zone the transport is dominated by turbulent mixing. In the viscous sublayer, friction is mainly caused by viscous forces, while in the turbulent region friction is dominated by "apparent friction" caused by turbulent fluctuation motion [15]. Compared to the flow situation at a flat plate described so far, the flow problem through a pipe is not a flow with typical boundary layer character. Nevertheless, as with the flat plate, the pipe flow has a two-layer structure with the turbulent region in the core flow and the viscous sublayer near the wall.

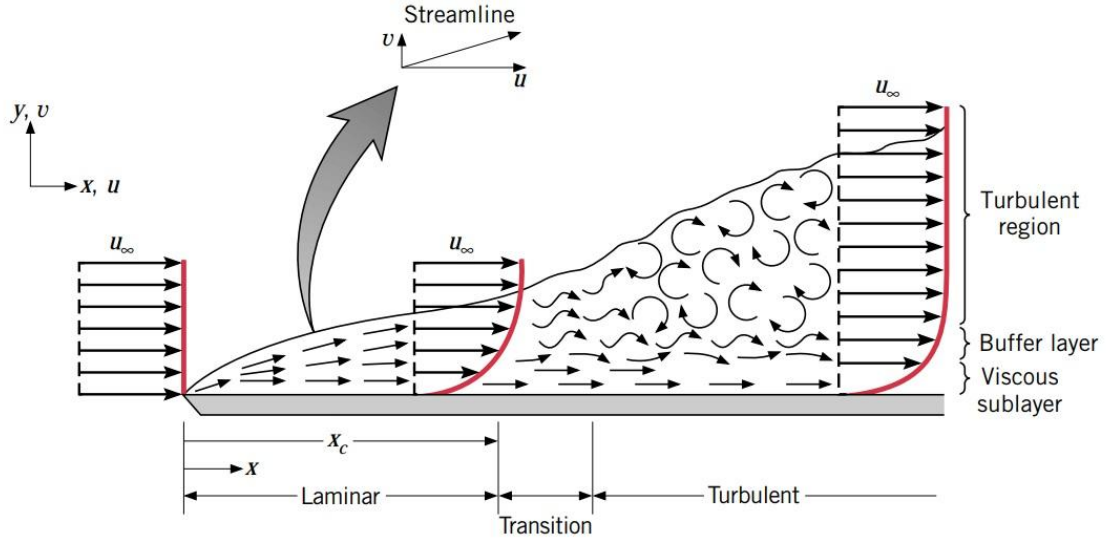


Figure 2-2: Velocity boundary layer development on a flat plate [14]

Furthermore, in the case of pipe flow, a distinction must be made between entrance length flow conditions and fully developed flow conditions. On the bottom half, Figure 2-3 shows the development of the velocity boundary layer in a tube, assuming a constant inlet velocity at tube entrance ($x=0$) for turbulent flow. When fluid elements contact the boundary surface, they assume zero velocity. The velocity boundary layer thickness gradually increases from the inlet to the outlet. However, due to the limited diameter of the pipe, the velocity boundary layer cannot grow infinitely, and a hydrodynamic developed flow occurs downstream of a position $L_{e,h}$, where the velocity profile no longer changes. The hydrodynamic entrance length for turbulent flow is approximately independent of Reynolds number. For turbulent flow the hydrodynamic entrance length $L_{e,h}$ is generally defined by equation (2.5) [12].

$$10 < \frac{L_{\mathrm{e,h}}}{d_{\mathrm{i}}} < 60 \qquad (2.5)$$

On the top half, Figure 2-3 shows exemplary radial temperature profiles for inlet conditions, the thermal inlet region and the thermally fully developed flow. Like the velocity boundary layer, the thermal boundary layer also grows in the streamwise direction. Therefore, the temperature gradients at $r=r_{\mathrm{i}}$ decrease in the streamwise direction, hence reduce the heat transfer coefficient

with increasing $x$. In the case of laminar flow, the thermal entrance length is defined as a function of the hydrodynamic entrance length: $L_{\mathrm{e,th,lam}} = L_{\mathrm{e,h}} \cdot Pr$. From this, it is evident, that for highly viscous fluids with $Pr$>100 (e.g., oils), the velocity profile is fully developed while the thermal boundary layer is still under formation. For turbulent flow however, the thermal entrance length is nearly independent of $Pr$ [14]. As a first approximation it can therefore be assumed that the thermal entrance length for turbulent flow equals to equation (2.6) [14].

$$L_{\mathrm{e,th}} \equiv 10 \cdot d_{\mathrm{i}} \tag{2.6}$$

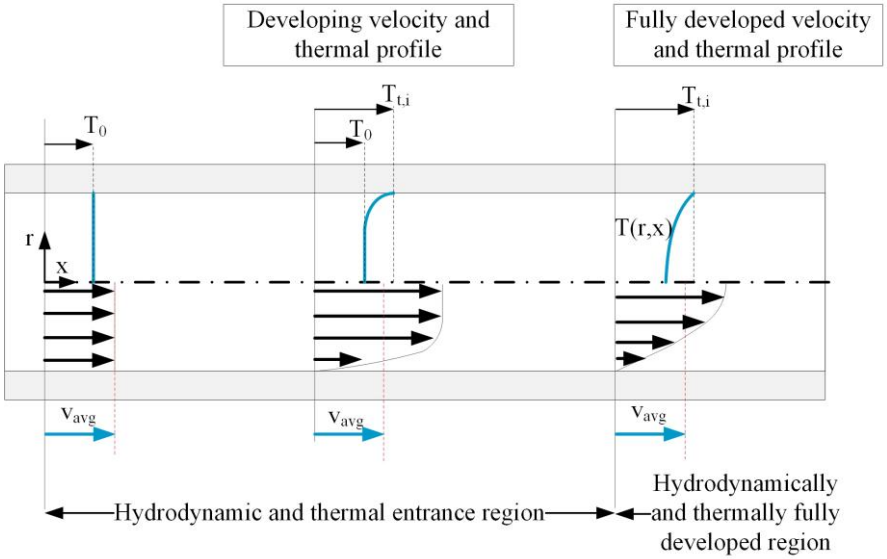


Figure 2-3: Velocity (bottom) and thermal (top) boundary layer development in a tube (laminar flow)

Regardless of the particular nature of the convection heat transfer mechanisms, the so-called Newton's law of cooling can be used to describe the local convective heat flux $\dot{q}_x$ (e.g., equation (2.7)) or the mean heat flux over the heating section $\dot{q}$ (equation (2.8)) at the boundary surface between tube and fluid [12].

$$\dot{q}_{\mathrm{x}} = h_{\mathrm{x}}\left(T_{\mathrm{t,i}} - T_{\mathrm{s,x}}\right) \tag{2.7}$$

$$\dot{q} = h_{\mathrm{m}} \Delta\vartheta_{\mathrm{ln}} \tag{2.8}$$

$$\Delta\vartheta_{\mathrm{ln}} = \frac{\left(T_{\mathrm{t,i}} - T_{\mathrm{s,in}}\right) - \left(T_{\mathrm{t,i}} - T_{\mathrm{s,out}}\right)}{\ln\left(\frac{T_{\mathrm{t,i}} - T_{\mathrm{s,in}}}{T_{\mathrm{t,i}} - T_{\mathrm{s,out}}}\right)}$$

$$h_{\mathrm{m}} = \frac{1}{l_{\mathrm{heat}}} \int_0^{l_{\mathrm{heat}}} h_{\mathrm{x}} \mathrm{d}x$$

Where $h_{\mathrm{x}}$ is the local heat transfer coefficient, $h_{\mathrm{m}}$ is the mean heat transfer coefficient (both expressed in W/(m²K)) and $\Delta\vartheta_{\mathrm{ln}}$ is the logarithmic temperature difference [12].

In 1915, Wilhelm Nußelt introduced the concept of the dimensionless heat transfer. The Nusselt number, named after him, plays a central role in this concept. For pipe flow, the dimensionless

local Nusselt number $Nu_x$ is defined by equation (2.9), the mean Nusselt number $Nu_m$ is defined by equation (2.10):

$$Nu_{\mathrm{x}} \equiv \frac{h_{\mathrm{x}} \cdot d_{\mathrm{i}}}{\lambda} \tag{2.9}$$

$$Nu_{\mathrm{m}} \equiv \frac{h_{\mathrm{m}} \cdot d_{\mathrm{i}}}{\lambda} \tag{2.10}$$

In both equations $\lambda$ is the heat conductivity of the fluid. Several authors have proposed correlations to compute the Nusselt number of turbulent fully developed flow in circular tubes as a function of Prandtl and Reynolds number. The most well-known are the Gnielinski equation, the Dittus-Boelter equation and the Sieder and Tate correlation (see Table 2-1: Convection correlations for turbulent flow in a smooth circular tube). Although both the Dittus-Boelter and the Sieder-Tate equation are mostly satisfactory and easily applied, they can result in large errors. Such errors can be reduced using more recent, but more complex correlations ( [16], [17]). The Gnielinski correlation is valid over a large Reynolds number range and includes a dependency of heating length, as well as applied flux density. Properties should be evaluated at mean fluid temperature. (except for the inner wall Prandtl number)

| **Author** | **Correlation** | **Validity range** |
|---|---|---|
| Gnielinksi: [18], [19] | $Nu_{\mathrm{m}} = \frac{\xi/8 \cdot Re \cdot Pr}{1 + 12.7 \cdot \sqrt{\xi/8}(\mathrm{Pr}^{2/3} - 1)} \left[1 + \left(\frac{2r_{\mathrm{i}}}{l_{\mathrm{heat}}}\right)^{2/3}\right] \left[\frac{Pr}{Pr_{\mathrm{t,i}}}\right]^{0.11}$ With: $\xi = (1.8 \cdot \log_{10} Re - 1.5)^{-2}$ | $0.1 \leq Pr \leq 1000$ $10^4 \leq Re \leq 10^6$ $d_{\mathrm{i}}/l \leq 1$ |
| Dittus-Boelter: [20], [14] | $Nu_{\mathrm{m}} = 0.023 \cdot Re^{4/5} \cdot Pr^{n}$ With: *n=0.4* for heating a fluid | $0.7 \leq Pr \leq 160$ $Re \geq 10'000$ $l/d_{\mathrm{i}} \geq 10$ |
| Sieder-Tate: [21], [14] | $Nu_{\mathrm{m}} = 0.027 \cdot Re^{\frac{4}{5}} \cdot Pr^{\frac{1}{3}} \left(\frac{\mu}{\mu_{\mathrm{t,i}}}\right)^{0.14}$ | $0.7 \leq Pr \leq 16'700$ $Re \geq 10'000$ $l/d_{\mathrm{i}} \geq 10$ |

Table 2-1: Convection correlations for turbulent flow in a smooth circular tube

Figure 2-4 shows the results obtained when applying the correlations listed in Table 2-1 for fully developed flow at $10'000 \leq Re \leq 300'000$, $Pr = 11$ and $Pr = 4$, as well as $\Delta T_{\mathrm{t,i-s,m}} = T_{\mathrm{t,i}} - T_{\mathrm{s,m}} = 1\ \mathrm{K}; 50\ \mathrm{K}; 150\ \mathrm{K}$[1]. The Gnielinski correlation predicts the highest Nusselt numbers. The biggest deviations occur for a combination of high Reynolds number and high temperature difference between film temperature and mean bulk temperature with up to +37% compared to the Dittus-Boelter equation. The Sieder-Tate correlation predicts values up to 13% higher than the values predicted by the Dittus-Boelter equation for high temperature gradients between fluid

[1] Operational conditions for Solar Salt in a Solar Receiver (see chapter 3.1)

and film temperature. This result shows that care must be taken when choosing a Nusselt number correlation, as the different correlations yield a rather large range of predictions.

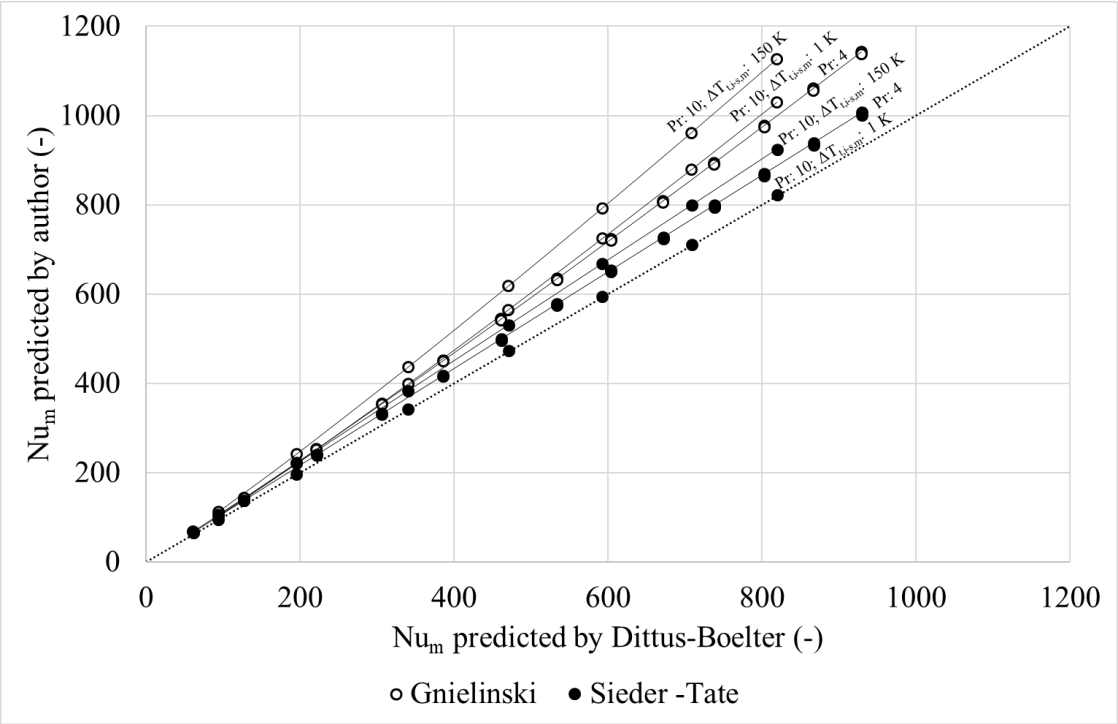


Figure 2-4: Comparison of prediction of mean Nusselt number by the Gnielinski and Sieder-Tate correlation with the Dittus-Boelter equation for different assumptions of Re, Pr and film temperatures [22]

## 2.3 Friction Factor

Beside the Nusselt number, the pressure difference required to sustain a certain flow through a heat exchanger tube needs to be known. In tubular flow, most commonly the Moody (or Darcy) dimensionless friction factor $\zeta$ is used for this purpose [23]:

$$\zeta \equiv \frac{-\left(\frac{dp}{dx}\right) \cdot d_\mathrm{i}}{\rho \cdot \bar{u}^2/2} \tag{2.11}$$

For fully developed laminar flow of an incompressible fluid, the friction factor can be analytically deduced. For fully developed turbulent flow, the available data ultimately relies on experimental results. Figure 2-5 shows the friction factors over a wide Reynolds number range for different surface conditions of the tube in a so-called Moody diagram. It can be observed that the friction factor is the lowest for a smooth surface and increases for higher surface roughness of the tube. In the current work, Reynolds numbers ranging roughly between 10000 and 300000 are of interest. It can be observed, that for a smooth tube the dependency of the friction factor on Reynolds number is more pronounced, than for a new or used drawn steel pipe with a relative roughness of 0.001 or 0.01 respectively.

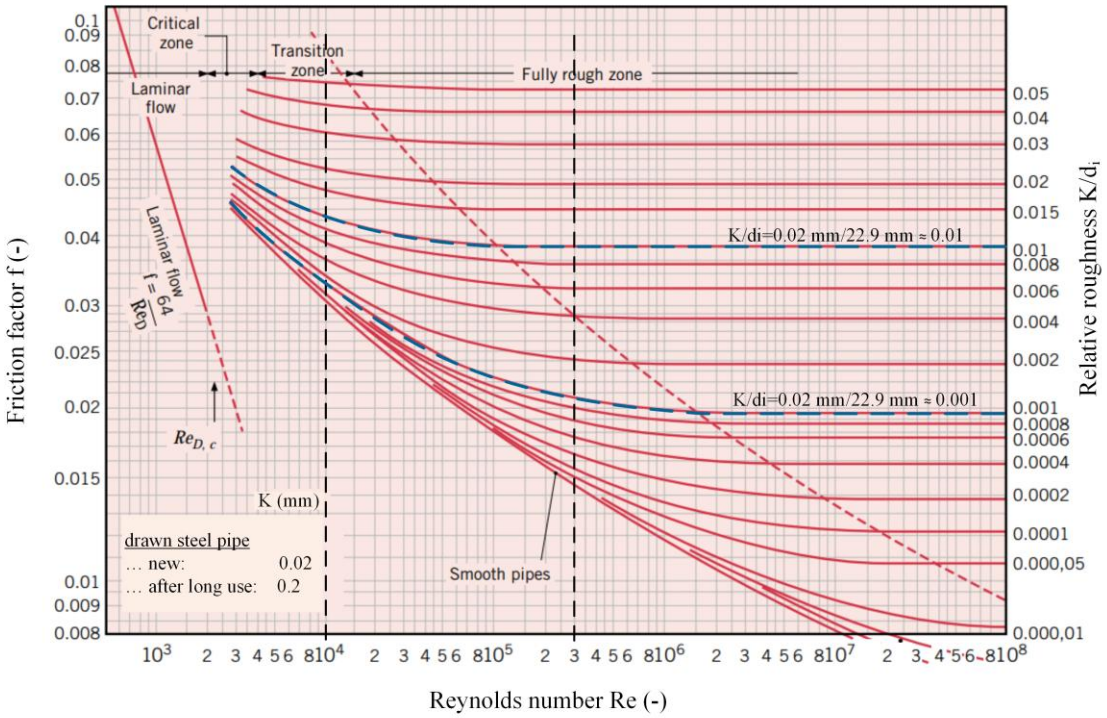


Figure 2-5: Friction factor for fully developed flow in a circular tube [23]

## 2.4 Induction Heating

Induction heating is the process of heating electrically conductive materials by electromagnetic induction. Applying an alternating voltage to an induction coil will result in an alternating current (AC) in the coil circuit. This alternating coil current entails a time-variable magnetic field at the same frequency as the coil current, which again induces eddy currents in an electrically conductive workpiece – e.g., the test tube – placed inside the coil. Primarily, the induced eddy currents produce heat in the workpiece by the Joule effect. In ferromagnetic materials, magnetic hysteresis additionally generates heat – which is caused by friction between magnetic dipoles, when ferromagnetic metals are magnetized first in one direction and then in another.

The eddy currents are oriented in the opposite direction of the coil current and have the same frequency as the coil current. The magnitude of the eddy current is proportional to the strength of the magnetic field, the area of the loop, the rate of change of flux and inversely proportional to the resistivity of the material (see Figure 2-7). A given eddy current leads to a voltage drop $U$, which is given by Ohm's Law: $U = RI$. The corresponding heating rate is given by $P = I^2R$.

The equations for the study of electromagnetic processes are the so-called Maxwell equations. Ampère's circuital law relates the integrated magnetic field of a closed electrical path to the electric current passing through the electrical path. The Faraday equation relates the electric field intensity $\boldsymbol{E}$ in a closed curve and the time-varying magnetic flux density $\boldsymbol{B}$. Gauss law for magnetism states that the magnetic field B has divergence equal to zero, meaning the magnetic field has no sources or sinks. Detailed information on the equations and their meaning can be found in the relevant technical literature ( [24], [25], [26]).

Ampère's circuital law: $$\nabla \times \boldsymbol{H} = \boldsymbol{J_f} + \frac{\partial \boldsymbol{D}}{\partial t} \quad (2.12)$$

Maxwell-Faraday equation: $$\nabla \times \boldsymbol{E} = -\frac{\partial \boldsymbol{B}}{\partial t} \quad (2.13)$$

Gauss's law: $$\nabla \cdot \boldsymbol{D} = \rho^{charge} \quad (2.14)$$

Gauss's law for magnetism: $$\nabla \cdot \boldsymbol{B} = 0 \quad (2.15)$$

An analytical solution that satisfies the equations system built by the Maxwell equations (equations (2.12), (2.13), (2.14) and (2.15)) exists only for simple geometries, for material with linear and isotropic properties and sinusoidal variation fields. In the case of cylindrical workpieces heated by solenoidal inductors the analytical solutions of the electromagnetic problem lead to quite complex formulas, which are generally evaluated using dimensionless diagrams. More complex geometries are generally analyzed using numerical approaches.

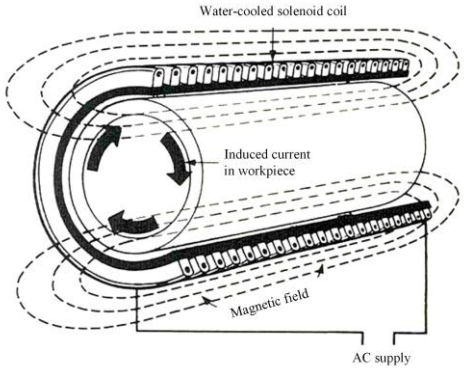


Figure 2-6: Schematic illustration of the magnetic field and current induced by a solenoid coil carrying an AC current in a cylindrical workpiece [24]

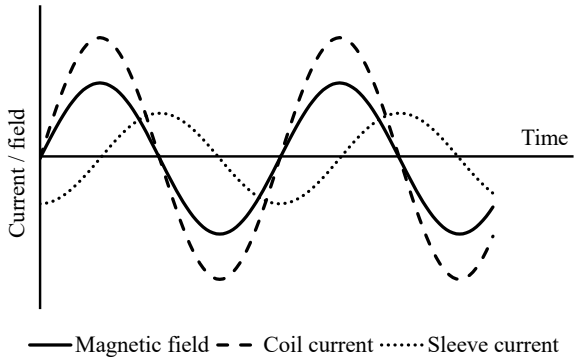


Figure 2-7: Qualitative variation of the current, the strength of the magnetic field and the eddy current induced in a conductive workpiece (sleeve) induced by a solenoid coil carrying an AC current.

It is assumed that an infinitely long solid cylindrical bar of non-magnetic material and isotropic properties is placed inside an infinitely long solenoid coil, through which flows an AC current at very high frequency. The so-called skin-effect produces an uneven distribution of the current density in the cross section of a workpiece: the current density in the workpiece decreases from the surface towards the center. The magnetic field from the solenoid creates an eddy current in the workpiece. This eddy-current runs in the opposite direction of the current in the solenoid (see Figure 2-6). Consequently, the magnetic field which originates from the eddy current counter-acts the process that has created it [27].

For a conducting semi-infinite body, which can be approximated as a cylinder of infinite radius, the skin effect can be derived analytically from Maxwell's equations (2.12) - (2.15). Based on this formulation, the electromagnetic penetration depth δ can be defined to characterize the exponential attenuation of induced currents within the conductor, as commonly described in the literature [25, 24].

For the semi-infinite body it can be shown that the current density $J$ reduces from the surface towards the center following the exponential law [24], see equation (2.16). Since the volumetric power density correlates with the current density according to equation (2.18), an analogous correlation can be deduced for the volumetric power density (2.17). In both cases, $\delta$ is the so-called penetration depth in meters (2.19). It can be defined as the distance from the surface of the conductor at which the current density is reduced to 1/e times lower than the current density at the surface [26]. Figure 2-8 illustrates the distribution of the current density and power density for the semi-infinite body as a function of relative distance from the surface.

$$J = J_{\mathrm{t,o}} e^{-\frac{y}{\delta}} \qquad (2.16)$$

$$w = w_{\mathrm{t,o}} e^{-\frac{2y}{\delta}} \qquad (2.17)$$

$$w_{r_o} = \rho_{\mathrm{el}} J_{r_o}^2 \qquad (2.18)$$

$$\delta = \sqrt{\frac{2\rho}{2\pi f \mu_0 \mu_{\mathrm{r}}}} \qquad (2.19)$$

According to equation (2.19), the penetration depth depends on the electrical resistivity, the relative magnetic permeability, and the applied frequency. Increasing excitation frequencies or increasing magnetic permeabilities result in decreasing penetration depths and therefore in more pronounced skin effects. It can be easily demonstrated that in the surface layer of thickness equal to the penetration depth 86.5% of the total active power is dissipated like in a semi-infinite conducting body. At lower frequencies, however, the distribution differs from the exponential distribution, depending on the frequency, the material characteristics, and the geometry of the body.

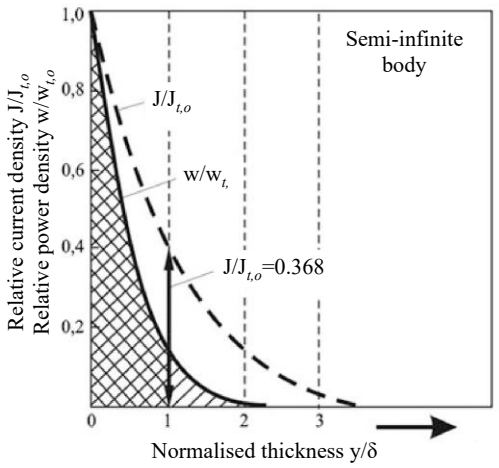


Figure 2-8: Distribution of relative current density $J/J_{\mathrm{t,o}}$ and relative power density $w/w_{t,o}$ as a function of distance from the workpiece surface for a semi-infinite body [26]

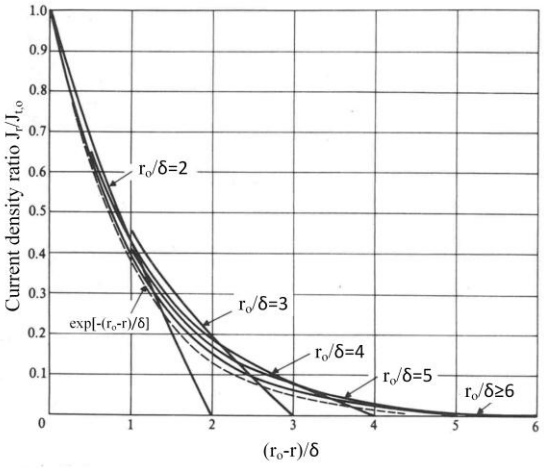


Figure 2-9: Current density distribution $J_r/J_{\mathrm{t,o}}$ in a solid cylinder as a function of normalised radius for different relative outer radius $r_o$. The dashed line shows the distribution expected for a semi-infinite body [24]

In the case of an infinitely long non-magnetic cylindrical rod placed in an infinitely long solenoid, the analytical solution of the Maxwell equations leads to complex formulas, which can be

evaluated using dimensionless diagrams. Figure 2-9 shows the radial distribution of relative induced current density as a function of $r_o/\delta$ and $(r_o - r)/\delta$. The dotted lines indicate the expected diagram for the previously discussed semi-infinite body.

It can be observed, that for small cylinder radius compared to the penetration depth $\delta$ at low relative radius of the workpiece, the decline in current density ratio is less pronounced as for a semi-infinite body. The exponential distribution is reached in practice only for values of $r_o/\delta \geq 6$.

For thin-walled tubes of non-magnetic material the current density over the thickness of the tube can be assumed to be uniform across the cylinder, because the field causing the current flux is the applied magnetic field and to a lesser extent the reaction field of the current in the workpiece. This assumption is reasonably accurate for $d_i/t_t \geq 10$ and $t_t/\delta \leq 0.2$ [24].

All considerations so far referred to non-magnetic materials; in ferromagnetic workpieces, the current density distribution is influenced not only by the temperature dependent resistivity, but also by the local value of magnetic permeability, which depends on temperature and local magnetic field intensity. Below the Curie point, the power distribution in ferromagnetic materials is highly non-uniform and undergoes a dramatic change above that temperature [26].

# 3 State of the Art

This section first summarizes the boundary conditions prevalent in state-of-the-art central solar receiver absorber tubes. These boundary conditions form the basis for the specifications of the heat transfer measurement setup. In the following section a thorough literature review of empirically deduced forced convective heat transfer for molten salt in cylindrical tubes is given. This is followed by a literature review of nitrate salt forced convective heat transfer in spirally grooved tubes. The next section gives a brief overview of the main decomposition reactions of nitrate salts and the resulting mechanisms which could interfere with the convective heat transfer. The last section gives a detailed literature review about the thermophysical properties of Solar Salt.

## 3.1 Conditions in Central Solar Receiver Absorber Tubes

Concentrating solar power (CSP) is a renewable energy technology, which converts slar radiation into thermal energy by the means of optical concentration. Depending on the system configuration, the generated thermal energy can be stored in low cost and highly efficient thermal storage systems. Thereby, CSP is able to reliably provide dispatchable renewable energy at low costs and can therefore be considered one of the backbones of future renewable energy systems [4].

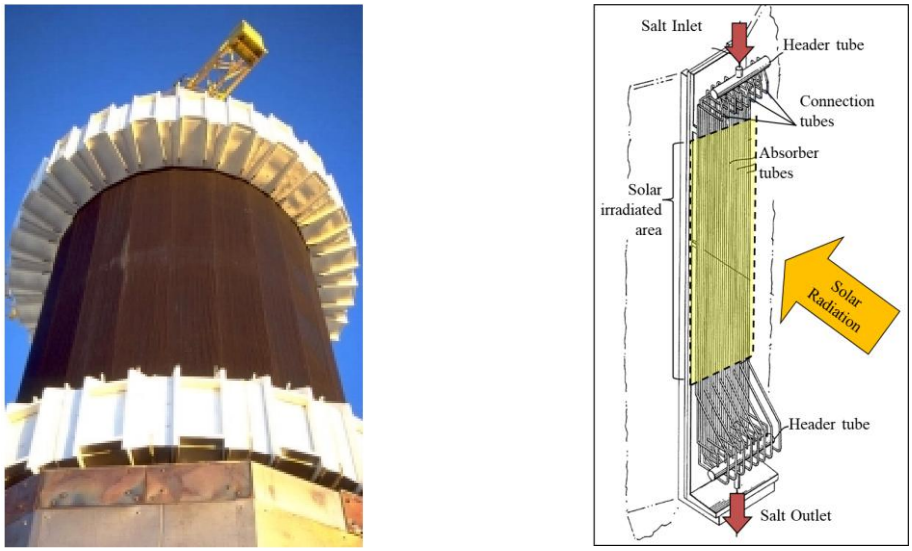


Figure 3-1: Left: Solar Two molten salt Receiver, Daggett, California [28]; Right: Schematic structure of receiver panel [2]

In a first step, the geometric and thermal specifications prevalent in molten salt receivers are collected. For this purpose, the publicly available data of several different molten salt receivers is analyzed: Solar Two [28], MSEE [29], Thémis [30], HPMS-I external receivers [10], CSP Reference plant [31], Gemasolar [32], Crescent Dunes [33], NOOR III [34] and Atacama 1 [35]

(see details in Appendix A). Most of these receivers use Solar Salt (60 wt-% $NaNO_3$; 40 wt-% $KNO_3$) as the heat transfer fluid. For this reason, this work focuses on the convective heat transfer of Solar Salt. Absorber panels are manufactured in individual modules to facilitate handling during fabrication, transportation, construction, and maintenance. Figure 3-1 shows the most common design concept of the receiver panels: It consists of several vertically arranged parallel cylindrical tubes, the so-called absorber tubes, that are connected to one header at the top and bottom, respectively. Figure 3-1 on the right also highlights the solar irradiated area of the solar receiver. In the investigated receivers, the full temperature gradient from 290 °C to 565 °C is not realized in one panel, but the salt flow travels around the receiver in a serpentine fashion.

The absorber panels are typically supported at the top and are allowed unrestricted downwards thermal expansion. The salt inlet temperature of today's receivers ranges between 280 and 300 °C, the salt outlet temperature between 550 and 565 °C. Because of the desired high transferred thermal flux densities, the required tube wall thickness should be minimized to minimize thermal stresses across the wall thickness of the tubes. This leads to employed tube dimensions ranging from as low as an inner tube diameter $d_i$=18 mm and tube wall thickness $t$= 1.2 mm [28] up to $d_i$≈50 mm [31]. The irradiated absorber lengths range between 10 and 30 m and one panel can consist of more than 100 parallel tubes [10].

The absorber panels are designed to withstand high flux densities up to roughly 1 MW/m² [5]. The allowable flux densities depend on two main factors: 1) the peak allowable flux density as a result of the thermo-mechanical fatigue and creep analysis; and 2) the tolerable maximum film temperatures to limit corrosion and salt degradation in the absorber tubes [36]. The allowable flux density is a result of each specific receiver design, salt temperature and cooling rates by the salt. This is because only half of the absorber tube is directly irradiated, while the other half is protected by the backwall insulation. In addition, the applied flux is non-uniform over the irradiated height of the absorber tube: to optimize the optical performance of the surrounding heliostat field, heliostats tend to aim more towards the center of the receiver, generally causing lower applied flux at the beginning and end of the irradiated height .

shows the results of an exemplary simulation of the allowable flux density as a function of salt temperature at full salt mass flow rate as well as the simulated achievable mean flux densities for a respective 140 $MW_{th}$ and 700 $MW_{th}$ external receiver for design point mass flow [38], [10].

The allowable thermal flux density ( ♦ ) is roughly constant at a value around 900 to 1000 kW/m² at a bulk salt temperature ranging from 290 to 450 °C and then decreases sharply down to 300 kW/m² at an outlet temperature of 565 °C. The drop of the allowable flux density above 450 °C is caused by the choice of a maximum allowable film temperature of commonly 600 °C [36]. The 600 °C limit was chosen in the design of the Solar Two test receiver (1995) to limit the corrosion rates of the absorber tubes in contact with the high temperature salt [36]. It has been demonstrated at laboratory scale that higher cycle temperatures can be achieved, while maintaining moderate salt degradation rates, by increasing the oxygen partial pressure [39].

In this work, film temperatures of at least 600 °C and higher shall be investigated. For mass flow rates lower than the design point mass flow the allowable flux density would decrease [36]. Beside

the dependency of the allowable flux density on salt temperature and salt flow bulk velocity, the applied flux density on the absorber tubes varies with the incidence angle of the radiation over the circumference of the absorber tube.

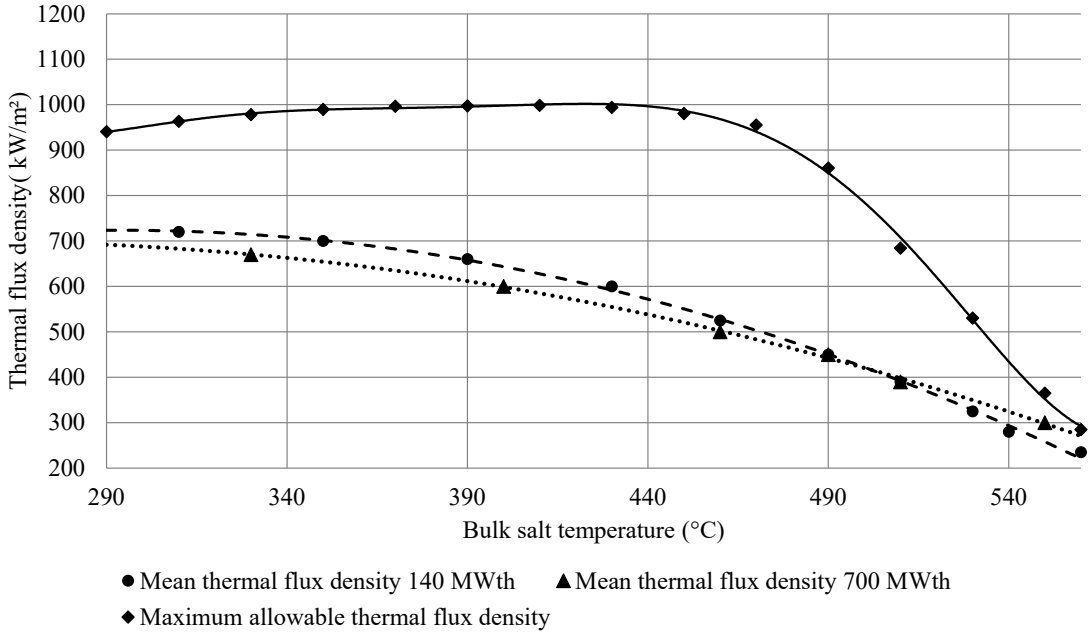


Figure 3-2: Exemplary mean and peak flux density of a 140 and 700 $MW_{th}$ external receiver (operation with full solar load) [10]

This is because only half of the absorber tube is directly irradiated, while the other half is protected by the backwall insulation. In addition, the applied flux is non-uniform over the irradiated height of the absorber tube: to optimize the optical performance of the surrounding heliostat field, heliostats tend to aim more towards the center of the receiver, generally causing lower applied flux at the beginning and end of the irradiated height [37].

All investigated solar receivers expose an irradiated length to tube diameter ratio of more than 100. Hence, hydrodynamically fully developed flow conditions should be assumed in the absorber tubes. Even though one could argue that the thermal boundary layer cannot be regarded as fully developed in a varying flux boundary condition, it is also assumed that thermally fully developed conditions are present.

Above temperatures of roughly 400 °C, Solar Salt is chemically active (see chapter 3.4). The highest salt bulk and film temperatures occur in the last panel. Commercial receivers usually use an average salt velocity in the tube of roughly 3 m/s. With an irradiated absorber height of maximum 30 m, this would lead to a total residence time of the salt in one panel of 10 seconds.

Table 3-1 summarizes the conditions prevalent in the investigated central solar receiver absorber tubes.

| Parameter | State-of-the-art Solar Tower plant |
|---|---|
| Heat transfer fluid: | Solar Salt (60 wt-% $NaNO_3$; 40 wt-% $KNO_3$) |
| Bulk salt temperature: | 290 °C - 565 °C |
| Salt film temperature: | 600 °C |
| Reynolds number: | 290 °C: 10000 – 100000<br>565 °C: 10000 – 270000 |
| Orientation of flow: | Vertical |
| Irradiated absorber length: | 15 - 30 m |
| Absorber tube dimensions: | DN20 – DN60 |
| Thermal heat flux to fluid: | 100 – 1000 kW/m² |
| Absorbed flux profile: | Axially and circumferentially varying |
| Flow profile: | Hydrodynamic and thermally fully developed flow |
| Estimation of average residence time of Solar Salt in the irradiated section of the last panel: | ~ 10 s |

Table 3-1: State of the art conditions in Central Solar Receiver Absorber Tubes

## 3.2 Forced Convective Heat Transfer in Circular Smooth Tubes

In the past, several studies have experimentally deduced the forced convective heat transfer of molten salts in smooth-circular tubes. Most setups consist of a single tube that is electrically heated. Some setups also use a double-tube setup, in which the outer tube carries a heating or cooling fluid and the investigated fluid flows in the inner circular tube. The following paragraph gives an overview of the work performed on molten salts published in the literature. The content of this section builds on the previously published article by Frantz et al. [22].

Hoffman [40] investigated the heat transfer of NaOH in circular tubes for the Reynolds number range of Re=6000-12000 and found that the experimental data lie approximately 9% below the values predicted by the Dittus-Boelter equation. Grele and Gedeon [41] investigated the same molten salt from *Re*=5300 to 30000 both during a cooling and a heating experiment. They found that the results of the heating experiment were about 20% higher than the data predicted by the Dittus-Boelter correlation, while the data from the cooling tests was in good agreement with correlations.

Hoffman et al. [42] investigated the forced convective heat transfer in circular tubes of the molten salt FLiNaK (46.5% LiF, 11.5 % NaF, 42% KF) for Reynolds numbers between 2300 and 9500. They observed that the measured heat transfer was up to a factor of two lower than the values

expected by the Dittus-Boelter equation. Grele et al. [43] analyzed the same salt for Reynolds numbers between 2000 and 20000 and heat fluxes up to 1261 kW/m². They observed average heat transfer coefficients that were roughly a third of the values calculated from the Dittus-Boelter correlation. Vriesema [44] evaluated the forced convective heat transfer of FLiNaK for Reynolds numbers between 14000 and 93000. He also found that the Dittus-Boelter correlation overestimates the heat transfer by ~17%. Both Grele et al. [43] and Hoffman et al. [42] observed the formation of a high thermal resistance corrosive layer during their tests. Hoffmann et al. [42] identified the composition, thickness and thermal conductivity of the layer and were able to show that good agreement is found between predictions and measurements, when the thermal resistance of the corrosion layer is considered. Ambrosek et al. [45] re-evaluated the work performed by Grele et al. [43], Hoffman et al. [42] and Vriesema et al. [44] in 2009. They found that a deviating thermal conductivity of the heat transfer fluid was the source of the lower measured heat transfer [45]. Ignat'ev et al. [46] investigated the heat transfer for low turbulent region Reynolds numbers of FLiNaK and found good agreement (< ±10%) between the Sieder-Tate correlation and their measurements.

Cooke et al. [47] investigated the convective heat transfer of the fluoride eutectic LiF-$BeF_2$-$ThF_4$-$UF_4$ and measured roughly -13% lower values than those predicted by the Dittus-Boelter correlation. As the authors could not ascribe this deviation to a low conductance surface film, they argued that although the results are within the uncertainty band of the Dittus-Bolter equation, the results could be linked to a delay in the transition to turbulent flow. Silverman et al. [48] measured the heat transfer of a fluoride salt similar to the one investigated by Cooke (LiF-$BeF_2$-$ThF_2$-$UF_4$) and of $NaBF_4$-NaF. For both salts, they found satisfactory agreement with the empirical Sieder-Tate correlation for $Re$>15000.

Bin et al. [49] measured the heat transfer of $LiNO_3$ for $Re$=17000 up to 45000 and found satisfactory agreement of ±15% between their measurement results and the Gnielinski correlation. Using the same experimental setup, Yu-Ting et al. [50] measured the heat transfer of the same molten salt for Re ranging between 4100-9850. They found a deviation lower than ±15.3% of the values predicted by the Gnielinski correlation.

Hoffman et al. [51] furthermore investigated the convective heat transfer of the nitrate salt mixture HITEC ($NaNO_2$-$NaNO_3$-$KNO_3$) over a Reynolds number range of 4850 up to 24710. They found that the forced convective heat transfer of HITEC in a circular tube can be described by the Dittus-Boelter equation. Furthermore, they compared their data to the measurements obtained previously by Kirst and Nagle with HITEC ($Re$: 2000-30000) [52]. They found good agreement of their data with the Kirst and Nagle [52] data in the transition flow regime. However, for $Re$>10000, considerable deviations from the Dittus-Boelter equation are found (> +20%), that could not be assigned to a cause. More recently, Wu et al. [53] published their results on the convective heat transfer of HITEC in circular tubes. They found that the Dittus-Boelter equation predicts the Nusselt number with maximum deviation of +25%. Chen et al. [54] analyzed the Nusselt-number of HITEC salt in a salt-to-oil concentric tube heat exchanger, where the molten salt flows through the inner tube and is cooled by the oil for Reynolds numbers ranging between 10000 to 50000. They found good agreement with the Gnielinski correlation. In 2020, Kuchibhotla et al. [3]

published a literature review on the experimental data of forced convective heat transfer of molten salts which includes some of the authors listed above. He et al. [55] studied HITEC in a large-scale shell-in-tube heat exchanger. In this experiment, four measurement points are published for the tube-side heat transfer for Reynolds numbers ranging between 10000 up to 19000 and a fitted curve is deduced. The measured points were within ±20% of the fitted curve.

Xingyang et al. [56] analyzed the local and mean Nusselt number for a nonuniform heated circular tube with HITEC. They achieved this nonuniform heating by applying a copper coating over half the circumference of the tube. By varying the coating thickness, flux density ratios of 2 and 5.7 between upper and lower half of the tube are achieved. They observed that the variation of heat flux ratio had only little effect on the mean Nusselt number. The adapted correlation shows a maximum deviation of 10.4% from the experimental data and yields between 5% to 9% lower values than the original Sieder-Tate correlation. This is all fairly close to the overall uncertainty of the Nu number of 7.7% stated by Xiangyang et al [56]. Also, it must be noted, that a decrease in Prandtl number did not decrease the Nusselt number for all their experiments, which is non-typical and is not further addressed by the authors. The measurement data of Xingyang et al. [56] hence suggest, that nonuniform heating of the tube does not lead to unexpected variations in heat transfer compared to uniform heating.

Jiangfeng et al. [57] observed a remarkable decrease of the heat transfer performance during their experiments with HITEC for inner wall temperatures above ~500 °C: they measured the heat transfer up to film temperatures of 600 °C. Compared to their previous values at lower film temperatures, they recorded 15% to 40% lower measured values compared to expectations. Indeed, the maximum recommended operation temperature of HITEC salt is 538 °C. Above this temperature, the salt is no longer chemically stable and decomposes. Jiangfeng et al. [57] concluded that local decomposition of the salt was probably causing the decrease in heat transfer. However, this hypothesis was not verified by an analysis of the salt.

Das et al. [58] analyzed the heat transfer of Solar Salt in an innovative experimental setup: A cartridge heater is inserted into a tube. The Solar Salt then flows through the annular section between cartridge heater and tube. The tests were carried out for Reynolds numbers up to 200000 and for various heat fluxes up to more than 1000 kW/m². They found that the measurements at Reynolds numbers comparable to previous literature data were in good agreement. However, for higher Reynolds numbers they found that the measured data were up to more than 3.5 times lower than the values predicted by the Gnielinski correlation. Also, they observed a significant trend with heat flux: for the maximum heat flux, the measured Nusselt number was up to 1.5 times lower than the prediction [58].

In summary, some authors have mentioned effects, that can impact the convective heat transfer in a manner that deviates from standard correlations, such as non-wetting of metallic surfaces, the formation of a low-conductance film or the chemical degradation of the molten salt. However, the first two effects have not been observed by most authors during the experiments with nitrate salts. Hence, it can be argued that most of the authors conclude that molten salts behave like normal fluids and that the heat transfer can be predicted with standard correlations such as the

Gnielinski correlation, which has been deduced for $10^4 \leq Re \leq 10^6$, $0.1 \leq Pr \leq 1000$ and $d_i/l_{heat} \leq 1$ [18] (see chapter 2.2).

Solar Salt has a low thermal conductivity ranging between ~0,4 and 0,5 W/m/K, which is favorable for storage design. However, this property presents a challenge to heat exchanger and receiver design: the low conductivity results in low heat transfer coefficients from the tube wall to the fluid, thus limiting the allowable heat flux. However, high heat fluxes up to > 1 MW/m² are desirable to minimize heat exchanger size and thus heat exchanger costs. Therefore, high fluid velocities are commonly employed in nitrate salt tubular heat exchangers. Central receivers using molten salt as a heat transfer fluid operate at relatively high Reynolds numbers; ranging from 10000 to more than 200000 (see chapter 3.1). However, the available experimental data on the forced convective heat transfer of molten salt in circular tubes for Reynolds numbers above 50000 is sparse (see Figure 3-3). The only studies that have experimentally investigated this Reynolds number region are the ones performed by Das et al. [58] and Vriesema [44], who both measured significantly lower values than expected. Especially the results of Das et al. would imply drastic underestimation of temperature levels in absorber tubes and molten salt, leading to degradation, corrosion, and ultimately premature failure of receivers. In addition, the findings of Jianfeng et al. show that local salt degradation due to film temperatures above the chemical stability of the molten salt can lead to a lowering of the heat transfer.

For this reason, this thesis investigates the forced convective heat transfer of Solar Salt at Reynolds numbers up to 200000 as well as the impact of film temperatures above the chemical stability limit of Solar Salt of 600°C stated in the literature.

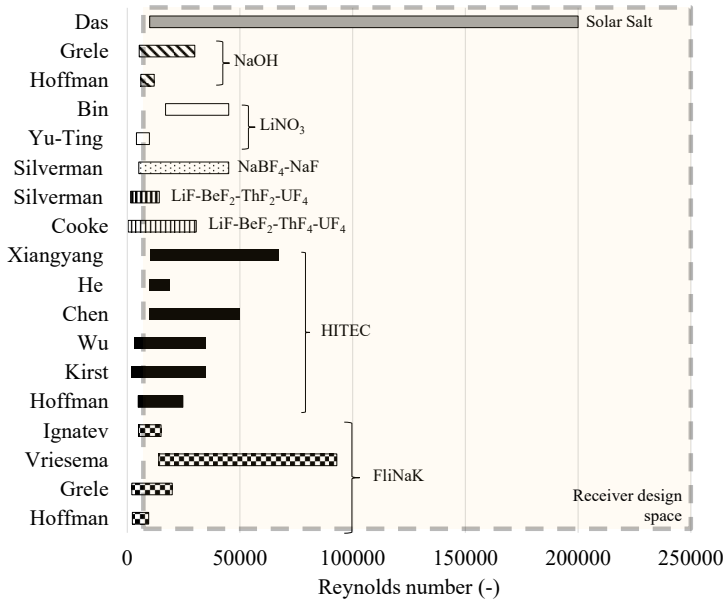


Figure 3-3: Reynolds number range of experimental data for the forced convective heat transfer of molten salts in circular tubes by author and salt type. The dashed box represents the receiver design space [22]

## 3.3 Forced Convective Heat Transfer in Enhanced Tubes

The content of this section builds on the previously published article by Frantz et al. [59]. For today's engineering practice, sixteen different enhancement techniques have been identified [60]. These techniques can be broadly classified in passive and active methods. Passive methods to enhance the forced convective heat transfer in a tube have been employed in various industrial fields such as desalination or power plant condensers and have been widely investigated in the literature [7]. Two main passive approaches can be distinguished: 1) Methods implying the deformation of the tube (rough surfaces or extended surfaces trough transverse or helical ribs or fins); 2) insertion of structures into the tube that disturb the fluid flow (displaced enhancement devices or swirl flow devices, such as twisted tapes or wire coils) [61]. The main idea behind these approaches is the disturbance of the existing boundary layer, increase of heat transfer area, increased turbulence of the flow or a combination of all three, which leads to an increased heat-transfer performance. The most successful technique, mainly because of its effectiveness and simplicity in application, has been augmentation through surface modification [61]. Here the surface roughness of the tube is increased by forming repeated grooves in the tube. These grooves create a disturbance of the laminar sublayer in the near-wall turbulent flow and as a consequence increase the forced convective heat transfer. The most common groove pattern for large scale production is a helical groove pattern because it allows a continuous fabrication process through rolling or indenting [62]. Figure 3-4 shows the definition of the main geometric parameters groove height e, groove pitch p, helix angle of groove $\alpha$ and contact angle of the roughness profile $\beta$. Generally, both the Nusselt number and the friction factor increase for decreasing groove pitch $p$, increasing groove height $e$ and higher helix angles $\alpha$. Of these three factors, the groove height $e$

has the strongest impact [62]. The groove height affects the separation of the boundary layer by vortex and jet generation. The groove pitch restraints the boundary layer development and thus leads to thinner boundary layers. However, it was observed that for small pitches sluggish and stagnant vortex can occur, which lowers the heat transfer [63]. Other factors, such as groove shape or groove width are found to play a minor role in the heat transfer increase [64].

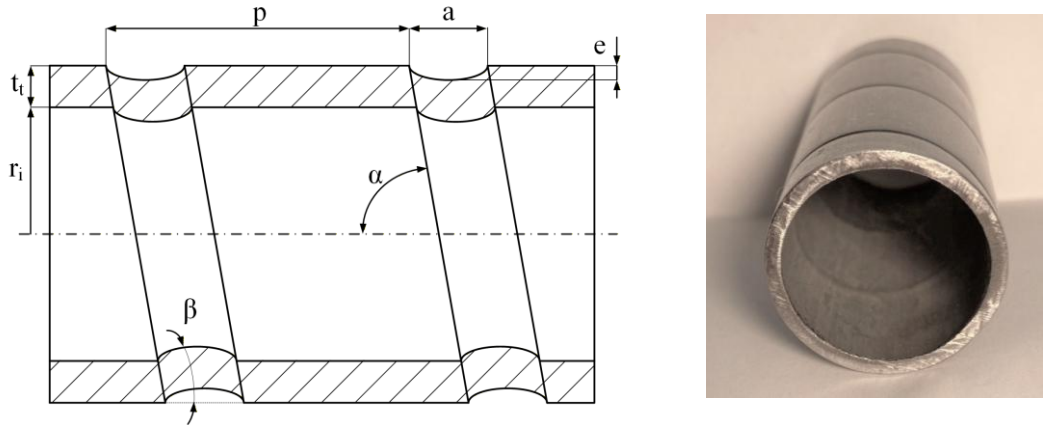


Figure 3-4: Left: Geometry definition of spirally grooved tube; Right: Specimen of the test tube used in this work [59]

Numerous investigations have been published in the past about the heat transfer and friction factor of fluids in enhanced tubes [65]. As the present experimental results are generated for single-phase forced convective flow in a rough surface or corrugated tube [7], the presented literature is limited to the work performed on this type of enhancement. Furthermore, the published work on wire coil inserts is included because several authors consider that wire coil inserts disturb turbulent flow in an analogous fashion to grooved tubes ( [66], [62]). In a first step an overview over past and current research involving all fluids is given. In a second step the available research on the enhanced heat transfer using molten salts is presented and analyzed in more detail.

In 1971, Webb et al. [67] published correlations based on experimental data for transverse grooves, while Gee and Webb [68] presented correlations for helical ribs in 1980. In 1982, Li et al. [69] developed correlations for helical ribs which also include the impact of groove pitch length and groove angle. In 1996, Ravigururajan and Bergles [62] developed general correlations for the friction factor and heat-transfer coefficient for single-phase turbulent flow in internally augmented tubes. They verified their correlations for a wide range of tube parameters with $e/d_i$=0.01 to 0.2; $p/d_i$=0.1 to 7.0 and $\alpha$/90=0.3 to 1.0 using experimental data from seventeen authors (>1650 datapoints for pressure drop, 1800 data points for heat transfer). The collected experimental data were collected for Re numbers ranging between 5000 up to 250000 and Pr ranging between 0.66 up to 37.6. Most of the studies of the database used water or air as the working fluid. Their deduced correlation predicts 96% of the friction factor database and 99% of the Nusselt number database to within ±50%. 77% of the friction factor and 69% of the Nusselt number database are predicted within ±20% [62]. The following two equations show the resulting correlations for the expected ratios of friction factor $\zeta_a/\zeta_0$ and Nusselt number $Nu_a/Nu_0$ [7]:

$$\frac{\zeta_a}{\zeta_0} = \left\{\left[29.1 \cdot Re^{0.67-0.06\cdot p/d-0.49\cdot\alpha/90} \cdot \left(\frac{e}{2r_i}\right)^{1.37-0.157\cdot p/d} \cdot \left(\frac{p}{2r_i}\right)^{-1.66e^{-6}\cdot Re-0.33\cdot\alpha/90} \cdot \left(\frac{\alpha}{90}\right)^{4.59+4.11e^{-6}\cdot Re-0.15\cdot\frac{p}{d}} \cdot (1+(2.94\cdot\sin\beta)/n)\right]^{15/16}\right\}^{16/15} \quad (3.1)$$

$$\frac{Nu_a}{Nu_0} = \left\{1+\left[2.64 \cdot Re^{0.036}\left(\frac{e}{2r_i}\right)^{0.212} \cdot \left(\frac{p}{2r_i}\right)^{-0.21} \cdot \left(\frac{\alpha}{90}\right)^{0.29} \cdot \mathrm{Pr}^{-0.024}\right]^7\right\}^{1/7} \quad (3.2)$$

Where $\beta$ is the contact angle in degrees of the roughness profile relative to the flow direction and is taken as 90° (semi-circular profiles [62]) and $n$ denotes the number of spiral rib starts.

In 2005, Garcia et al. [70] presented experimentally deduced correlations for the convective heat transfer and friction factor for flow enhancement using wire coil inserts in laminar-transition-turbulent regimes for Prandtl numbers ranging between 2.8 and 150 and Reynolds numbers ranging from 80 to 90000. They were able to show that wire coil inserts maximize their impact in transitional flow regimes [70]. In 2015, Ji et al. [71] published a review on the available literature on single-phase heat transfer enhancement techniques of liquid laminar and turbulent pipe flow. They summarized the work of a total of 13 authors, which have published experimental data on the thermo-hydraulic performance of corrugated tubes for Reynolds numbers ranging between 100 and 100000 between the years of 1977 and 2015. The review also contained the work of two authors who evaluated wire coil inserts. The experimental data were obtained with setups using water or oil. The evaluation of the thermo-hydraulic performance was performed following the approach proposed by Fan et al [72]. Ji et al. [71] summarized that an enhanced heat transfer of corrugated tubes can regularly be obtained with an identical pressure drop. The wire coil inserts in this study showed enhanced heat transfer per identical pumping power or identical pressure drop. In 2017, Ji et al. [73] performed a detailed review on several types of enhancement techniques for laminar and turbulent air flow. The reviewed data for wire coil inserts included six studies for Reynolds numbers ranging between Re=100 and 45000. Ji et al. summarized that heat transfer augmentation ratios through inserts for gases are in the range of 2-4 and friction factor increment ratios are higher than the heat transfer [73]. Furthermore, Ji et al. [73] summarized the work of 11 authors who studied the thermo-hydraulic performance of different corrugated tubes over a Reynolds number ranging between 2000 and 100000. Ji et al. [73] found that an enhanced heat transfer of corrugated tubes can regularly be obtained with the identical pressure drop and that the heat transfer ratios for gases are very similar to liquids, while pressure drop penalties for gases are considerably higher. The next paragraphs give an overview over the available experimental and simulation data on molten salt in corrugated tubes.

In 2013, Jiangfeng et al. [57] published their results of the convective heat transfer of the ternary nitrate salt HITEC ($NaNO_3$–$NaNO_2$–$KNO_3$, 7–40–53 wt.%) for salt temperatures ranging between 250 and 500 °C and for Reynolds numbers between 10000 and 30000. They compared their results of a smooth tube to three different transversely grooved tubes (α/90°=1) with groove heights of $e/d_i$=0.038; 0.046 and 0.092 and a relative groove pitch $p/d_i$=0.738. They fitted a correlation to their measurement data, which indicates that the Nusselt number can be increased

1.8 times for $e/d_i$=0.092. No measurements of the pressure difference are published. The same year, Jiangfeng et al. [74] published results of the convective heat transfer of the same molten salt for Reynolds numbers between 5000 and 15000 for spirally grooved tubes. Their measurement campaign was performed on four different tubes with a pitch angle of 78°, relative groove pitch of $p/d_i$=0.738 and the following relative groove heights: $e/d_i$=0.024, 0.031, 0.038 and 0.048. They found that the measured Nusselt number increases up to 1.4-1.7 times compared to a smooth tube for the highest relative groove height. An updated correlation for their measurement data was published by Jiangfeng in 2015 [75]. No pressure difference is published. Also, the same year, Chen et al. [76] published their results on enhanced tubes with HITEC salt for the Reynolds number range 10000-30000. They analyzed three transversally grooved tubes ($\alpha$/90°=1) with a relative groove pitch ranging between $p/d_i$=0.31-1 and relative groove heights ranging between 0.55 and 0.75. They found that no relevant increase of the Nusselt number is found for a relative groove pitch $p/d_i$=1. For the two tubes with lower relative tube pitch, they fitted two correlations over their measurement data; they found an increase of 1.2 to 1.3 times of the Nusselt number relative to a smooth tube. They also deduced a general correlation, but this correlation does not account for the impact of groove pitch on the Nusselt number, so it will not be further considered. They also compared the measured pressure difference of the different tubes and fitted correlations for each tube. It can be found that the friction factor is increased by a factor of 1.07 to 1.19. Xiangyang et al. [77] developed a CFD model for transversely grooved tubes and validated the model using experimental data obtained with the nitrate salt HITEC. The final simulation studied the heat transfer of different transversely grooved tubes ($\alpha$/90°=1) for three relative groove heights under non-uniform radiation and deduced a correlation for the Nusselt number. Furthermore, they varied the groove width and confirmed that the impact of groove width $a$ on the Nusselt number was lower than the impact of the groove height $e$.

Figure 3-5 shows the ratios of Nusselt number (left) and friction factor (right) deduced by the above-mentioned authors compared to the general correlations from Ravigururajan. The respective ratios are deduced using the author correlations (see Table 3-2) compared to the Sieder-Tate-correlation [21]. In this analysis the impact of the ratio of dynamic viscosity $(\mu/\mu_w)^{0.14}|_a/(\mu/\mu_w)^{0.14}|_s$ is neglected, as its impact is lower than a few percent. It can be observed that the general correlation of Ravigururajan overpredicts the measured Nusselt number ratio by 15% up to 90%. Better agreement of the general correlation of Ravigururajan to the specific correlations is found for the data of the relative friction factor of the simulation of Xiangyang et al. The friction factor ratio of the experimental data of Chen et al, however is overpredicted by a factor 1.7 up to 2.3.

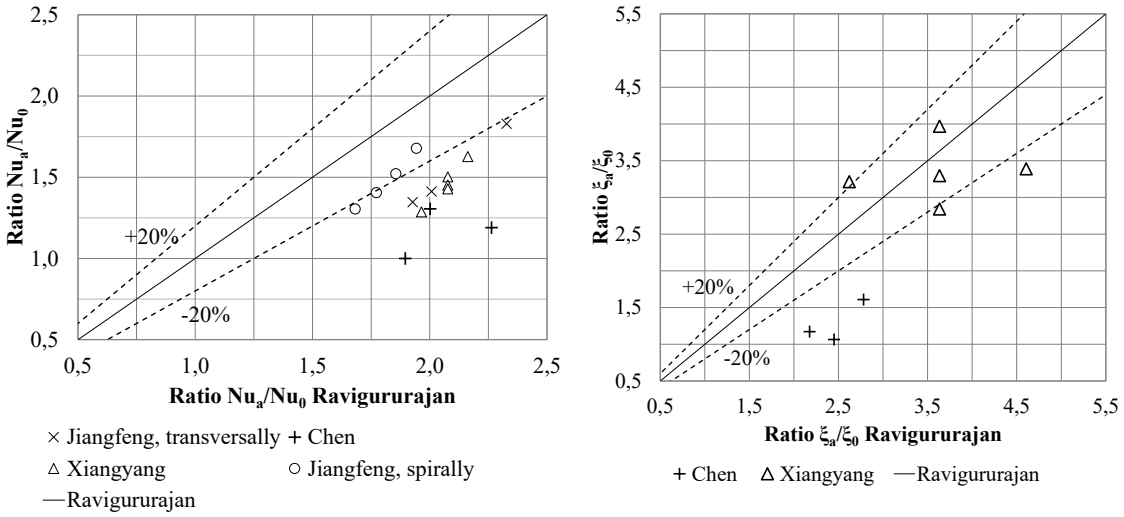


Figure 3-5: Left: Nusselt number ratio $Nu_a/Nu_0$ of different authors [57], [75], [76], [77] compared to the respective ratios predicted by the general correlation of Ravigururajan [7] (equation (3.2)). Right: friction factor ratio ζa/ζ0 of different authors [76] and [77] compared to the respective ratios predicted by the general correlation of Ravigururajan [7] (equation (3.1)) (adapted from [59])

| Source | Correlation author | α/90° | $e/d_i$ | $p/d_i$ |
|---|---|---|---|---|
| Jiangfeng, [57] | $\frac{Nu_a}{Nu_0} = \frac{0.0301Re^{0.796} \cdot Pr^{1/3}\left(1+\frac{2e}{d}\right)^{3.18}}{0.027Re^{0.8} \cdot Pr^{1/3}}$ | 1 | 0.038 | 0.738 |
| | | 1 | 0.046 | 0.738 |
| | | 1 | 0.092 | 0.738 |
| Jiangfeng, [75] | $\frac{Nu_a}{Nu_0} = \frac{0.02762Re^{0.798} \cdot Pr^{1/3}\left(1+\frac{2e}{d}\right)^{5.68}}{0.027Re^{0.8} \cdot Pr^{1/3}}$ | 0.867 | 0.048 | 0.738 |
| | | 0.867 | 0.038 | 0.738 |
| | | 0.867 | 0.031 | 0.738 |
| | | 0.867 | 0.024 | 0.738 |
| Chen, [76] | $\frac{Nu_a}{Nu_0} = 1; \frac{\zeta_a}{\zeta_0} = \frac{0.14Re^{-0.029 \cdot Pr^{1/3}}}{0.13Re^{-0.028 \cdot Pr^{1/3}}}$ | 1 | 0.047 | 1.000 |
| | $\frac{Nu_a}{Nu_0} = \frac{0.03524Re^{0.8 \cdot Pr^{1/3}}}{0.027Re^{0.8 \cdot Pr^{1/3}}}; \frac{\zeta_a}{\zeta_0} = \frac{0.28Re^{-0.087}}{0.13Re^{-0.028}}$ | 1 | 0.034 | 0.563 |
| | $\frac{Nu_a}{Nu_0} = \frac{0.03213Re^{0.8 \cdot Pr^{1/3}}}{0.027Re^{0.8 \cdot Pr^{1/3}}}; \frac{\zeta_a}{\zeta_0} = \frac{0.54Re^{-0.12}}{0.13Re^{-0.028}}$ | 1 | 0.034 | 0.313 |
| Xiangyang, [77] | Simulation results | 1 | 0.046 | 0.819 |
| | | 1 | 0.059 | 0.819 |
| | | 1 | 0.072 | 0.819 |

Table 3-2: Correlations and geometric specifications from literature

Based on the available experimental data the following conclusions can be made: general correlations are available for the relevant Reynolds and Prandtl number ranges. However, the

available experimental data for molten salts is limited to Reynolds numbers up to 30000. This is considerably lower than the Reynolds number used for example in concentrating solar power (CSP) applications, which are commonly operated at Reynolds numbers ranging between 10000 and more than 200000 [58]. Also, respective to heat transfer enhancements with structured tubes, compared to the experimental data, the general correlation of Ravigururajan overpredicts the measured Nusselt number ratio of other authors by up to 90% and the friction factor ratio by up to more than a factor of two.

## 3.4 Solar Salt Decomposition

The nitrate salt most used in CSP applications is the binary mixture of sodium nitrate ($NaNO_3$) and potassium nitrate ($KNO_3$) (see chapter 3.3). Both components are usually obtained from natural resources found in the form of salar brines or are produced synthetically [78], [79]. They are solid at ambient temperature, non-toxic and non-flammable. They are common components of fertilizers and explosives and show therefore a good availability in large quantities at low cost. The eutectic mixture of $NaNO_3$ and $KNO_3$ is found over a broad band ranging between 46 and 54 wt-% $NaNO_3$. Even though the eutectic mixture exposes a lower melting point (~222 °C), the common mixture – known as Solar Salt – generally consists of 60 wt-% $NaNO_3$ and 40% wt-% $KNO_3$. This composition has a slightly higher melting point (~238 °C), but the higher content of the lower cost component $NaNO_3$ leads to a significant reduction in cost of the mixture [80], [4].

Current state-of-the-art molten salt systems based on nitrate salts are limited to an upper salt temperature of 565°C [8]. This upper temperature limit is defined to minimize decomposition reactions of the salt that affect both the thermal properties of the salt and limit corrosion towards container materials [9]. However, a higher upper cycle temperature promises to decrease the levelized cost of electricity (LCOE), mainly driven by smaller storage and steam generator size, as well as a higher turbine efficiency [10]. The decomposition mechanisms of nitrate salts at high temperatures are complex, but can be broken down to a few main reactions, which will be shortly described in this section.

Above 400 °C the first reaction is the equilibrium reaction between nitrate and nitrite ions with gaseous oxygen (3.3) [81]. This reaction is observed at every scale from lab to large-scale tank and is reversible [9].

$$NO_3^- \rightleftharpoons NO_2^- + \frac{1}{2}O_2 \tag{3.3}$$

There is consensus in the literature, that a nitrate-nitrite equilibrium is established at 560 °C in air at ambient pressure at about 95 mol% $NO_3^-$ and 5 mol% $NO_2^-$ [82]. An increase in salt temperature shifts this equilibrium more towards the nitrite side, leading to mostly gaseous oxygen formation. If the salt is exposed to a step change in temperature, the time required to establish a new equilibrium nitrite concentration is on the order of several hours, based on the quantity of salt

[83], [9]. Several authors furthermore showed that an increase in oxygen partial pressure shifts the reaction equilibrium to the nitrate side [84], [9].

Above 550 °C, further decomposition of the nitrite ion is known to occur [81]. Several reaction mechanisms of this decomposition have been published. All of them propose the formation of oxide ions together with different gaseous species, such as nitric oxide, nitrogen dioxide (e.g., NO, $NO_2$), oxygen or nitrogen. One of the proposed reactions is the formation of an oxide ion that is dissolved in the melt and different nitrous gases from the nitrite ion according to reaction (3.4) [9].

$$2NO_2^- \rightleftharpoons O^{2-} + \mathrm{NO}(g) + \mathrm{NO_2}(g) \tag{3.4}$$

The oxide ions are dissolved in the molten salt, while the nitrous gases leave the salt. The reverse reaction proceeds only at a limited rate [83]. As discussed previously, the decomposition of the salt is temperature dependent. In the heated section of tubular flow, it is assumed that the decomposition process accelerates when the salt moves from the bulk region to the higher temperature film region and that the decomposition process then slows when the salt moves from the film region back to the bulk region [83]. The results of Sötz et al. [82] suggest that the formation of oxides via equation (3.4) is faster than with the pathway described by equation (3.3).

One concern is that localized decomposition of the nitrate salt in the film region with formation of gaseous products would form a local gas layer with low thermal conductivity and that this layer would negatively impact the convective heat transfer of Solar Salt in heat exchanger tubes. A decrease of convective heat transfer would then again lead to an increase in film temperatures and would probably entail further acceleration of the decomposition process.

Another important effect is the formation of an oxide-based corrosion layer on the metal surface in the heating zone driven by the high film temperatures. Indeed, numerous studies have been published in the past investigating the corrosion rates of different stainless steels and nickel base alloys in Solar Salt (see Figure 3-6). The corrosion mechanisms that occur are numerous and complex and are discussed in more depth in the relevant literature [85], [86].

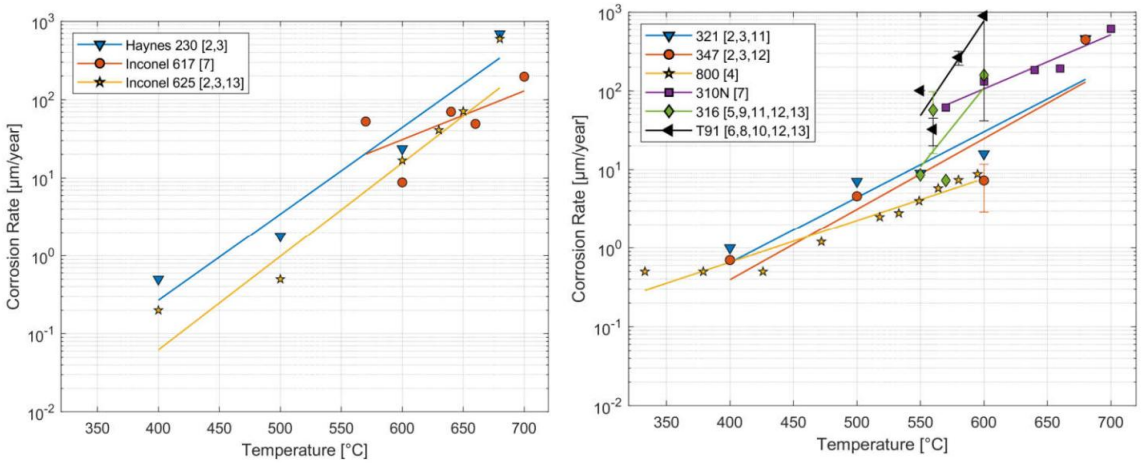


Figure 3-6: Corrosion rates of several Ni-base alloys (left) and austenitic steels (right) in Solar Salt as a fucntion of temperature [86]

Metallic corrosion and passivation of the steel surface generally proceeds via the oxidation of the metallic Fe, Cr or Ni with available nitrate ions. This process is believed to accelerate with the presence of oxide ions and possibly nitrite ions from reaction (3.4). Above roughly 500 °C the passivation is aggravated because of the thermal decomposition of nitrates. In addition, the thermal conductivity of the oxide layer is highly influenced by the porous structure of the oxide scale, as well as its composition. The formation of an oxide scale having a low thermal conductivity in the heating zone would decrease the overall heat transfer coefficient of the tube. This again would entail an increase in outer wall temperatures of the heated section if the same heat rate passes into the fluid. This effect was observed by some authors while performing heat transfer measurements with fluoride salts (see chapter 3.2).

Several authors have stated measured thermal conductivities of iron oxide scales ranging from 1 to 4 W/(m·K), [87], [88]. This is significantly lower than the expected thermal conductivity of the test tube (steel type 1.4748, $\lambda_t$ =15… 25 W/(m·K), see chapter B.2). Furthermore, the uncertainty of the thermal conductivity of the used stainless steel is later on assumed to be ±4% (see appendix B.2). The overall heat transfer coefficient of a stainless-steel tube with an oxide layer can be calculated using equation (3.5), where $t_{oxide}$ is the thickness of the oxide scale. It can easily be calculated that for a tube of the dimensions later on used in the experiment (see chapter 4.2), a corrosive scale thickness of 1 µm or 26 µm leads to an increase of the overall thermal resistance of +4% if a thermal conductivity of 1 W/m/K, respectively 4 W/m/K is assumed for the thermal conductivity of the corrosive layer. In experimental design and testing conditions it should therefore be made sure that the expected thickness of the oxide scale is minimized.

$$U_{oxidized} = \frac{1}{\frac{r_i \ln\left(\frac{r_i + t_{oxide}}{r_i}\right)}{\lambda_{oxide}} + \frac{(r_i + t_{oxide}) \ln\left(\frac{r_o}{r_i + t_{oxide}}\right)}{\lambda_t}} \tag{3.5}$$

## 3.5 Material Properties

The thermophysical properties of Solar Salt, water and tube material have a considerable impact on heat transfer and thus on the evaluation of the Nusselt number. The thermophysical properties of water and the tube material are relatively well known and can be found in appendix B.1. The next section presents the results of a thorough literature review on the thermophysical properties of Solar Salt and outlines the selection process and deduction of correlations. The section is derived from the article that was published in advance of this dissertation [22].

Solar Salt (60 wt% $NaNO_3$, 40 wt% $KNO_3$) is chemically active above temperatures of roughly 450 °C, undergoing a variety of reactions depending on the temperature and the composition of the cover gas (see chapter 3.4). This contributes to somewhat scattering information about the thermophysical properties of Solar Salt in the literature. However, precise knowledge of the thermophysical properties – such as specific heat capacity, density, dynamic viscosity, and thermal conductivity – is crucial for the design of processes using Solar Salt either as a storage or heat transfer medium and are also relevant assumptions to deduce the heat transfer properties. For all following calculations a composition tolerance of ±1 wt-% is assumed.

Table 3-3 summarizes the basic properties of Solar Salt used in the following sections.

| **Property** | **Value** |
|---|---|
| Molar mass $NaNO_3$ | 84.99 g/mol |
| Molar mass $KNO_3$ | 101.10 g/mol |
| Molar mass Solar Salt | 90.78 g/mol |
| Mole fraction $NaNO_3$ in Solar Salt | 64.08 % |
| Mole fraction $KNO_3$ in Solar Salt | 35.92 % |

Table 3-3: Basic properties Solar Salt

Specific heat capacity

Several literature values have been reported in the past for the specific heat capacity of Solar Salt. In general, the authors use a differential scanning calorimetry (DSC) or a modulated DSC (MDSC) to obtain their results [89]. Experimentally, different dependencies of $c_p(T)$ have been found in the liquid state, ranging from increasing, to constant, to decreasing with salt temperature [90]. Three main factors influence the quality of the heat capacity measurements [91]:

- Side reactions, such as endothermic evaporation, salt-gas phase interactions (oxygen, release, $NO_x$ release), salt decomposition (formation of nitrites) or interaction with crucible materials
- Due of the low surface tension of Solar Salt, the salt tends to wet any available surface as long as its temperature exceeds the melting point of the salt. This leads to so-called “salt creeping” and can lead to loss of salt mass during the DSC measurements
- Uncertainty of the used measurement equipment (DSC ~ ±10%, MDSC ~ ±5% [92])

The specific heat capacity of the single salts, e.g., $NaNO_3$ and $KNO_3$, and of the mixtures in the liquid state is typically constant [93] whereas an increasing $c_p(T)$ behavior is more typical of weakly interacting liquids. However, nitrates belong to the class of strongly interacting liquids [90]. A decreasing heat capacity with temperature is not viable from a thermodynamic point of view [93].

In 2018, D'Aguanno et al. investigated the thermostatic properties of Solar Salt by combining classical molecular dynamics (MD) simulations and DSC experiments and found that the heat capacity is principally independent of temperature [90]. This finding is empirically supported by the measurement data acquired by Rogers and Janz [94] by DSC in 1982 for various compositions of $NaNO_3$-$KNO_3$ from 250 up to 430 °C (see Figure 3-7).

This also holds true for the values published by Bradshaw et al. in 1987 for $c_p(T)$ of Solar Salt from 250 to 400 °C [80]. Both publications show no systematic temperature dependence of $c_p(T)$ outside the stated measurement uncertainty. Muñoz-Sánchez et al. [89] conducted a round-robin test involving 8 partners in 2017 with the aim to deduce $c_p(T)$ of one common Solar Salt sample using a standardized sample preparation procedure. The authors state a measurement reading uncertainty of ranging between 30 and 100 J/kg/K over all measurements. When taking account of the respective measurement uncertainty, the given results do not contradict a constant $c_p(T)$ assumption. In 2021, Jung et al. [95] published their results on a Calvet-type DSC in which they confirmed a constant heat capacity between 249 °C and 483 °C.

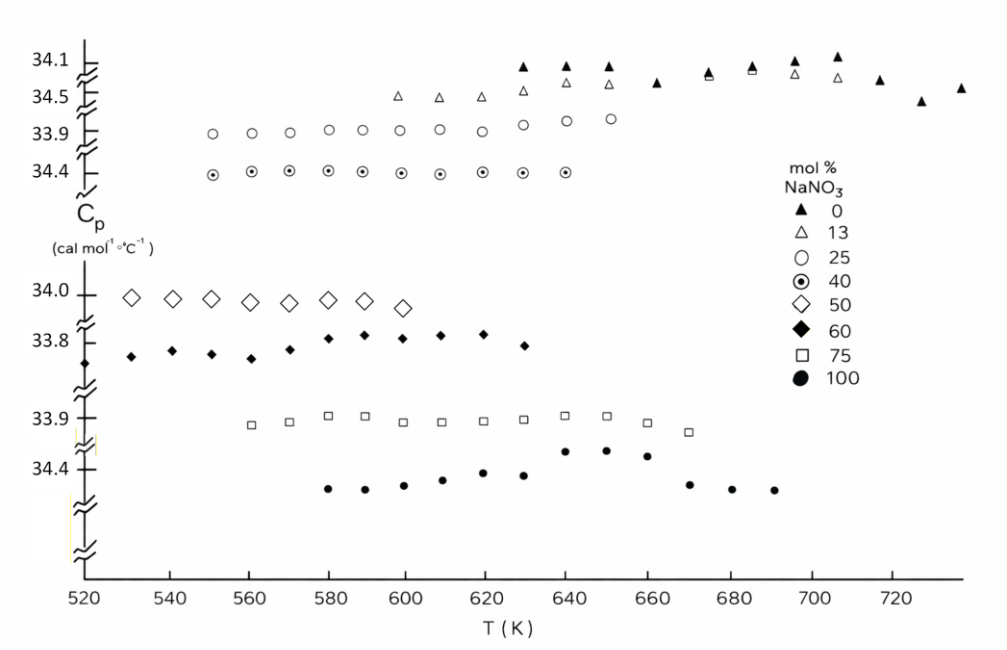


Figure 3-7: Specific heat capacity as a function of temperature for different compositions of $NaNO_3$-$KNO_3$ [94]

Table 3-4 summarizes the reported mean specific heat capacities of the the authors cited above.

| Author | Reported mean specific heat capacity |
|---|---|
| Rogers & Jans, 1982, [94] | 1584 ±83 J/kg/K |
| D'Aguanno 2017 (empirical), [90] | 1518 ±152 J/kg/K |
| Bradshaw, 1987, [80] | 1541 ±154 J/kg/K |
| Munoz-Sánchez 2017, Partner 1 ASTM E1269, [89] | 1610 ±70 J/kg/K |
| Munoz-Sánchez 2017, Partner 3 ASTM E1269, [89] | 1477 ±68 J/kg/K |
| Munoz-Sánchez 2017, Partner 5 ASTM E1269, [89] | 1553 ±50 J/kg/K |
| Munoz-Sánchez 2017, Partner 6 ASTM E1269, [89] | 1533 ±38 J/kg/K |
| Munoz-Sánchez 2017, Partner 1 MSDC Dynamic, [89] | 1494 ±45 J/kg/K |
| Munoz-Sánchez 2017, Partner 1 MSDC Isotherm, [89] | 1497 ±34 J/kg/K |
| Munoz-Sánchez 2017, Partner 1 MSDC Isoth.short, [89] | 1540 ±30 J/kg/K |
| Munoz-Sánchez 2017, Partner 2 MSDC Dynamic, [89] | 1450 ±15 J/kg/K |
| Munoz-Sánchez 2017, Partner 8 MSDC Isotherm, [89] | 1497 ±34 J/kg/K |
| Jung 2021, [95] | 1545 ±31 J/kg/K |

Table 3-4: Reported mean specific heat capacities by several authors

Based on this review of the literature, a temperature-independent specific heat capacity is assumed in this work. Under this assumption, the mean average of the given measurements of Jung et al., Bradshaw et al., D'Aguanno et al., Rogers & Janz and of each partner measurement set of Muñoz-Sánchez et al. is calculated:

$$\bar{c}_{p,S} = 1529\,\mathrm{J/kg/K} \tag{3.6}$$

Figure 3-8 summarizes all published data of Solar Salt as a function of temperature.

Bonk et al. [91] find that the variation in composition of $KNO_3$ and $NaNO_3$ has a negligible effect of less than 0.1% on the specific heat capacity. Another source of uncertainty is the presence of nitrite ions in Solar Salt at operation temperatures larger than 400 °C. After prolonged times at high temperature, an approximate value of $X_{NO_2} = 5\ \mathrm{mol\%}$ can be expected [96] according to equation (3.3). Using the assumption of a constant molar heat capacity, the impact of formation of $KNO_2$ and $NaNO_2$ can be estimated. An increase of up to 2% of the specific heat capacity can be found when assuming a composition of 64 mol-% $NaNO_3$, 31 mol-% $KNO_3$ and 5 mol-% $KNO_2$.

In a final step, the combined measurement uncertainty of the mean specific heat capacity $\sigma_{\bar{c}_{p,S}}$ is calculated as $\sigma_{\bar{c}_{p,S}} = \sqrt{\sigma^2_{\bar{c}_{p,S,u.a.}} + \sigma^2_{\bar{c}_{p,S,scat.}} + \sigma^2_{\bar{c}_{p,S,comp}}} = 51\,\mathrm{J/kg/K}$. Where $\sigma^2_{\bar{c}_{p,S,u.a.}}$ is the experimental standard deviation of the mean specific heat capacity (~21 J/kg/K), assuming the

measurement uncertainty stated by the authors. For authors that do not state a measurement uncertainty, a conservative default value of ±10% is assumed. $\sigma^2_{\bar{c}_{p,S,scat.}}$ is the experimental standard deviation resulting from the variations of the calculated mean between all authors (~43 J/kg/K) and $\sigma^2_{\bar{c}_{p,S,comp}}$ is the expected uncertainty caused by the uncertainty of the composition of the salt (~17 J/kg/K).

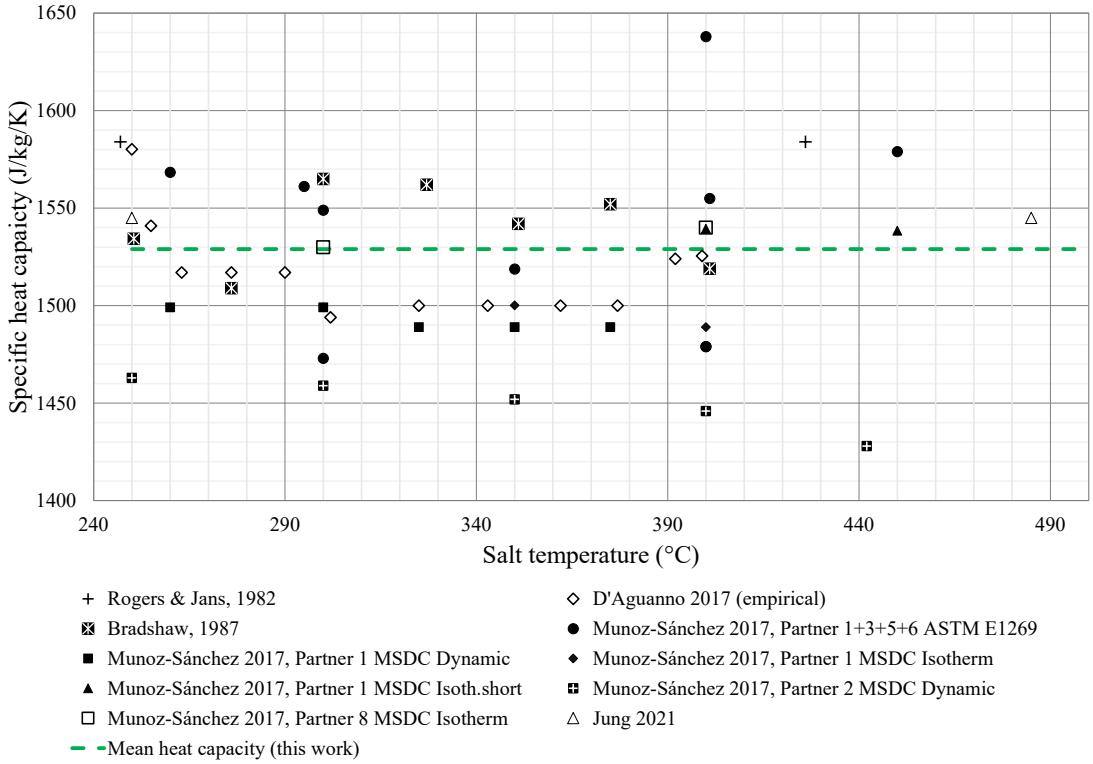


Figure 3-8: Specific heat capacity Solar Salt – Left: Values from the literature as a function of temperature; Right: Mean specific heat capacity over the full temperature range by author. For values marked with (*) no uncertainty of measurement is stated and ±10% is assumed (adapted from [22])

The only measurement data available for the full liquid range up to 540 °C have been published by Jung et al. [95]. Compared to the constant value of $c_p(T)$, $c_p$ = 1545 J/kg/K, measured in a temperature range of T = 240 to 483 °C, they measured an increase of up to 45 J/kg/K at 540°C. They attribute this 3 % increase to nitrite formation. The necessary time for nitrite formation is in the order of several hours to several days. In this work however, the dwell time of the solar salt in the heating section of the tube is much lower, hence it is assumed that the enthalpy of formation of nitrite does not play a role in the present heat transfer experiment. Therefore, it is assumed in this work that the specific heat capacity remains constant up to 550 °C.

Density

Janz et al. recommended density values for Solar Salt for temperatures up to 450 °C for various compositions of $NaNO_3$ and $KNO_3$ in 1972 [97]. The values for single salts were revised by Janz et al. in 1988, leading to slightly lower density values [1]. The results published by Nissen et al.

[98] for the density of a 50 mol-% to 50 mol-% $NaNO_3$-$KNO_3$ mixture from 300 °C to 600 °C are widely used for Solar Salt. Bauer et al. conducted a critical review of the available density correlations for Solar Salt and suggested an improved correlation, which accounts both for the updated single salt density values by Janz [97] and also for nitrite formation at high temperature operation. Their work demonstrates that the density of Solar Salt can be calculated using a quasilinear volumetric additivity rule (VAR) [99]. The correlation proposed by Bauer et al. [99] using the VAR method (see equation (3.7)) will be used for the calculation of the salt density.

$$\rho_s(T)[\mathrm{kg/m^3}] = 2118 - 0.7185 \cdot (T/°\mathrm{C}) \tag{3.7}$$

Figure 3-9 summarizes the densities proposed by the different authors as well as the finally used correlation in this work.

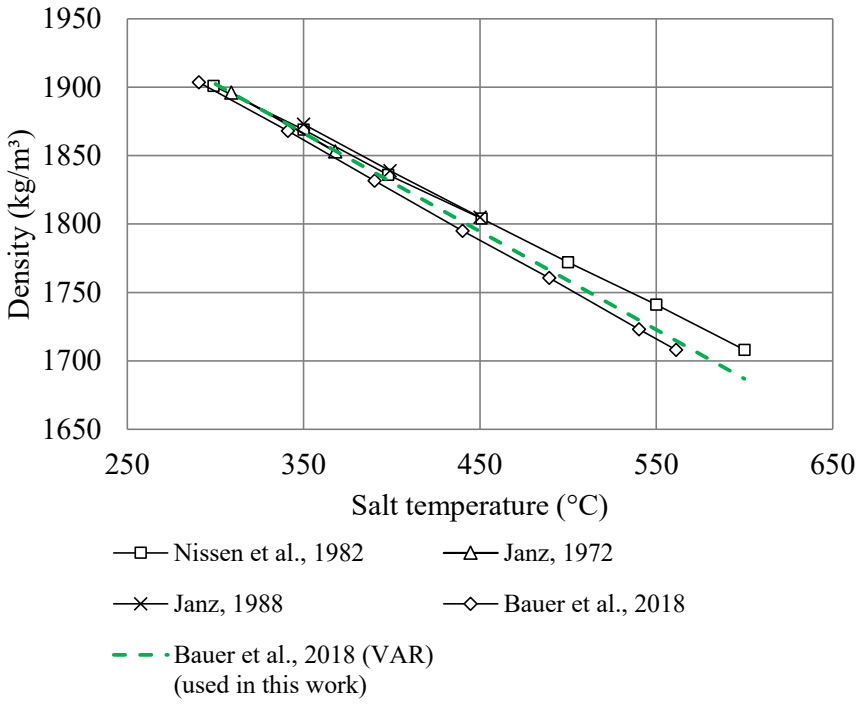


Figure 3-9: Density of Solar Salt as a function of temperature for various authors [22]

The variation in composition of $KNO_3$ and $NaNO_3$ has a negligible effect of less than 0.1% on the density of Solar Salt as it was found by Bonk et al. [91]. Bauer et al. showed that for a nitrite content of 5 mol-%, the density values are reduced by roughly 0.3%. The uncertainty of salt absolute temperature measurement leads to an uncertainty of ~0.2% for $\sigma_T$=5 K. As a result, the final relative uncertainty of the salt density is $\delta\rho_s = 0.4$ %.

Thermal conductivity

While several authors have published data on the pure salts $NaNO_3$ and $KNO_3$, the available data on the thermal conductivity of the Solar Salt mixture is poor [100]. Bauer et al. [91] summarized in a review that the thermal conductivity of the $KNO_3$-$NaNO_3$ system depends on the composition and that all authors, except one [101], found an approximately linear dependency on the

composition [102], [103], [104]. In 2015, Zhao et al. [105] deduced a theoretical model for predicting the thermal conductivity of binary molten salts based on the properties of the single salts. Comparison with existing literature data showed that the theoretical correlations predict the thermal conductivity of $NaNO_3$-$KNO_3$ mixtures within standard errors of 4.15% [100]. The following formulas show the formula proposed by Zhao et al.: where $\lambda_{XNO_3}$ is the thermal conductivity, $\rho_{XNO_3}$the density and $w_{XNO_3}$ are the mass fraction of the single salt respectively.

$$\lambda_s = \lambda_{NaNO_3} \cdot \left[ \left(1 - \left(\frac{b}{a}\right)^2\right) + \frac{\left(\frac{b}{a}\right)^2}{1 + \left(\frac{\lambda_{NaNO_3}}{\lambda_{KNO_3}} - 1\right)\frac{b}{2a}} \right]; \qquad \frac{b}{a} = \left( \frac{2\frac{\rho_{NaNO_3} \cdot w_{KNO_3}}{\rho_{KNO_3} \cdot w_{NaNO_3}}}{1 + \frac{\rho_{NaNO_3} \cdot w_{KNO_3}}{\rho_{KNO_3} \cdot w_{NaNO_3}}} \right)^{1/3}$$

For the calculation of the density of the single salts, the values published by Janz et al in 1988 are used [1]. The single salt thermal conductivity is calculated using the correlation published by Zao et al. [100]. The resulting curve of $\lambda_s$ decreases linearly as a function of temperature and can be described by equation (3.8):

$$\lambda_s(T) = -2.2849 \cdot 10^{-4} \cdot T(°C) + 0.54692 \tag{3.8}$$

Empirical data on the single salt properties only exist for temperatures ranging between 250 °C and 500 °C [91]. The thermal conductivity for temperatures exceeding this interval is extrapolated. Bonk et al. analyzed the impact of composition errors on the thermal conductivity. They found that the expected deviation is below ±0.2% [91].

Dynamic viscosity

Solar Salt can be considered a Newtonian fluid and typically shows low viscosity, similar to values of water at room temperature [91]. A correlation for the dynamic viscosity proposed by Nissen et al. [98] in 1982, based on measurements performed on an equimolar $NaNO_3$-$KNO_3$ composition is widely used for CSP applications [106]. Janz et al. [1] published several correlations for various compositions of $NaNO_3$-$KNO_3$ as a function of temperature in 1988. These correlations show a non-trivial course relative to composition, which is also a function of temperature. In 2019, Tasidou et al. [107] conducted a literature review of the available measurement data for the single salts $NaNO_3$ and $KNO_3$ and proposed updated equations for the single salts with an enlarged temperature validity interval accounting for measurement data up to 450 °C for $NaNO_3$ and 700 °C for $KNO_3$. The researchers found that deviations of newer viscosity data deviated less than 1% of the reference equations proposed by Janz [107]. For this evaluation the expressions for $KNO_3$-$NaNO_3$ compositions published by Janz will be used to minimize errors due to assumptions about mixing effects [1]. The correlation for Solar Salt is obtained through linear interpolation of 50 mol-% $NaNO_3$ – 50 mol-% $KNO_3$ and 75 mol-% $NaNO_3$ – 25 mol-% $KNO_3$. The resulting values are fitted using the least square method to yield the formula described by equation (3.9) for the dynamic viscosity of Solar Salt. The maximum deviation between fit and original values is less than 0.1%.

$$\eta_s(T/\mathrm{K}) = 0.08703 \cdot \exp\left(\frac{16990.8686}{R \cdot T(\mathrm{K})}\right) \tag{3.9}$$

Figure 3-10 shows the used correlation, the values commonly used by Nissen et al. [98] and the values deduced from the correlations given by Murgulescu et al. [108]. Considerable deviation between the Nissen correlation and the correlation deduced based on the Janz values can be found especially at temperatures lower than 300°C and higher than 500°C, which can not entirely be explained by the deviating composition of salt. Further research is necessary to investigate dynamic viscosity data above 450 °C.

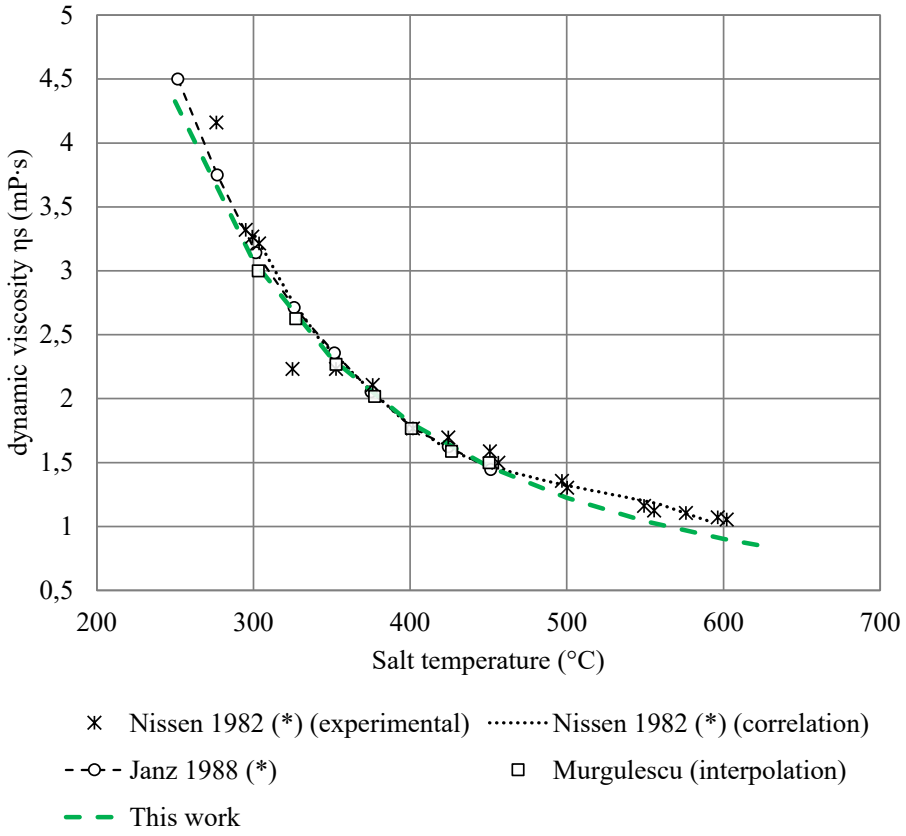


Figure 3-10: Dynamic viscosity of nitrate salt as a function of salt temperature: data marked with (*) are for equimolar $NaNO_3$-$KNO_3$; other data are for Solar Salt [22]

Specific electrical resistivity

For the characterization of the behavior of the salt in the magnetic field, the specific electrical resistivity is of interest. Janz published correlations for the specific electrical conductance of different mixing ratios of $NaNO_3$ and $KNO_3$ [97]. The specific electrical resistivity for the present mixture of 60% $NaNO_3$ and 40% $KNO_3$ is calculated by forming the reciprocal value of the electrical conductance and by linear interpolation of the correlations for 72% $NaNO_3$ and 46% $NaNO_3$ (see Figure 3-11). The deduced correlation for the specific electrical resistivity for Solar Salt is given by formula (3.10):

$$\rho_{el}(T/°C) = -1.66221e-15 \cdot T^5 + 4.31898e-12 \cdot T^4 - 4.5824e-9 \cdot T^3 + 2.52147e-6 \cdot T^2 - 7.42531e-4 \cdot T + 1.02204e-1 \quad (3.10)$$

It must be emphasized that the data published by Janz is only valid for the two mixing ratios of 72% $NaNO_3$ and 46% $NaNO_3$.a temperature range of 287°C to 397 °C, all values shown outside of this range are hence extrapolations.

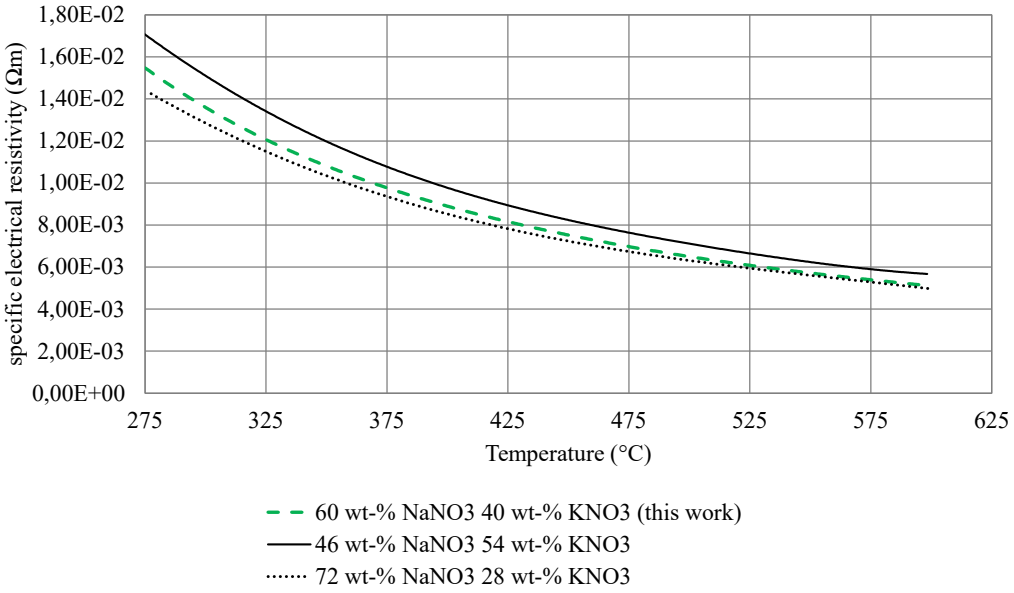


Figure 3-11: Specific electrical resistivity for two different compositions of $NaNO_3$ and $KNO_3$ according to [97] and Solar Salt as a function of temperature

# 4 Experimental Setup and Evaluation

An exclusively analytical treatment of the heat and mass transfer of a turbulent pipe flow failed so far because neither the turbulent shear stresses, nor the turbulent heat flux density nor the turbulent diffusion flux density can be determined in a purely theoretical way. For this reason, the heat transfer of turbulent pipe flow must be analyzed based on experiments [13]. This chapter first gives an insight into the selection process of the heating concept. Then the final experimental setup is described and the mathematical basis for the deduction of the Nusselt number deduced by the measurements and the reference Nusselt number as well as the friction factor is given. In a final section, the test procedure and measurement plan are described.

## 4.1 Selection of Heating Concept

Several different heating concepts for the test section are considered: a) Joule heating, b) impedance heating, c) heating cartridge, d) induction heater and e) using a secondary medium. The following performance criteras were selected in order to evaluate the different concepts:

- Re numbers between 10000 – 200000 achievable (yes/no)
- Flux densities between 100 – 1000 kW/m² achievable (yes/no)
- Applicability with enhanced tubes (yes/no)
- Theoretically achievable measurement uncertainty and main uncertainty impact parameter
- Feasibility

Most of the experimental setups found in literature use a **Joule heating concept** for the heating section (see chapter 3.2): a small electric potential difference is applied over the length of the desired heating section, which leads to an electrical current and heating of the tube. The initial concept of the heating section of the tube was conceived using a DC constant current source. In addition to the possibility to measure the heat input into the salt through mass flow and temperature gradient measurement measurement (calorimetric method), this approach offers the possibility to measure the power input to the salt through potential difference and electric current measurement (electrical method). This type of measurement generally leads to good measurement uncertainty, especially at high Reynolds numbers, where mass flows are high, and thus temperature gradients in the salt inlet and outlet are decreased. To achieve the flux densities ranging between 100 and 1000 kW/m² as present in solar absorber tubes, an applied potential difference ranging between 4 and 12 V would have been necessary (leading to roughly 2500 A of current passing through the tube). One concern with this approach is that an electrolysis current is generated at the tube to salt boundary by the potential difference, accelerating the decomposition reactions of the salt and the formation of an oxide scale and possibly impacting the convective heat transfer (see chapter 3.4).

The first question is whether ion conduction takes place if a potential difference is applied over the length of a tube through which an electrolyte flows. In a classical electrolysis setup, a potential difference is applied to two electrodes (cathode and anode) which are separated by an electrolyte. In the case of the pipe, however, the tube represents a single electrode over which the potential difference decreases continuously from one end to the other. In the case of the pipe it can be argued that no electrolysis reactions would take place because the local potential difference is not high enough. To confirm the single electrode concept in principle, a simple experiment was carried out using a wire to represent the tube and a saline solution to represent the salt: A single NiCr (NiCr6015) wire is placed in a saline solution (Water + NaCl) to which a DC potential difference is applied and both the potential difference and the current through the wire is measured (for more details see appendix C.1).

Figure 4-1 shows an exemplary picture of the single electrode water test at the outermost side of the wire respectively. As in the classical electrode setup[II], it is observed that hydrogen is formed on the cathode side and probably some oxidized nickel species on the anode side. It could also be seen that the reaction intensity is the strongest at the respective outermost side of the wire and decreases continuously towards the center of the wire. The presence of hydrogen was demonstrated by an oxyhydrogen test, which produced the expected characteristic sound.

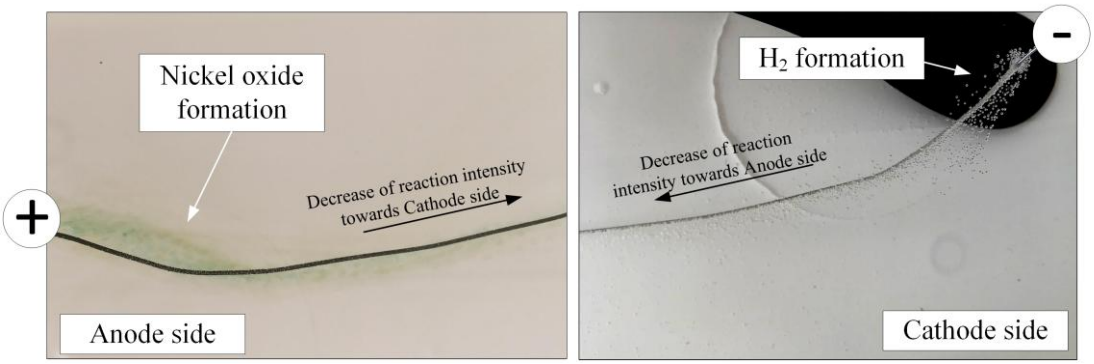


Figure 4-1: Hydrogen and nickel oxide formation in single electrode water test

Figure 4-2 shows the measurement results of the single electrode water test. The graph on the left shows that the measured current increases linearly with the applied current – following Ohm's law. Also, it can be seen that the measured current increases with higher salt content in the saline solution. The graph on the right shows the measured current minus the measured current for the pure water setup as a function of salt content in the solution. The measured additional current increases linearly with the salt content in the water. These two graphs show in addition to the qualitative findings discussed beforehand, that ion conduction is taking place in the single electrode setup. It can be concluded that electrolysis reactions can occur in principle in a heat transfer setup with molten salt using a DC current.

[II] A two-electrode setup was also tested using the same wire, but as the results of this setup are well-known, it will not be discussed in detail in this work

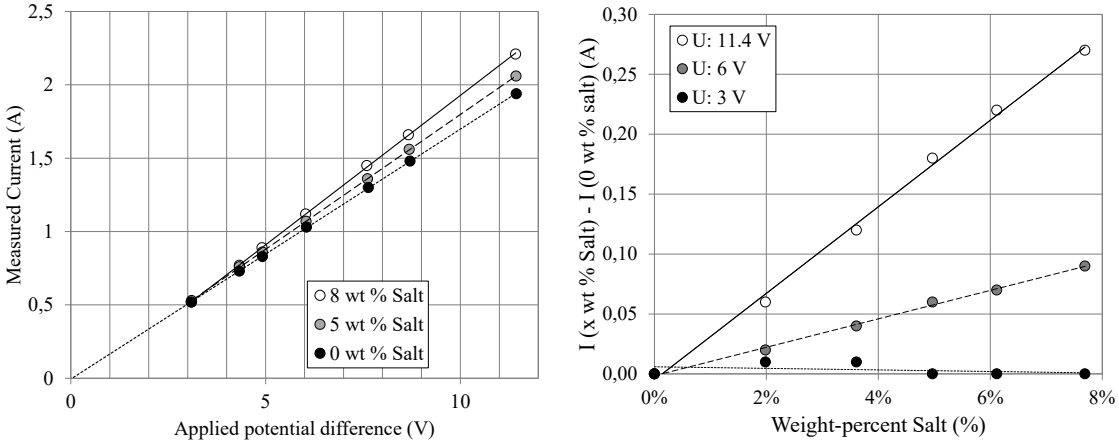


Figure 4-2: Measurement results of single electrode water test. Left: Total measured current as a function of applied potential difference for three different saline solutions. Right: Measured additional current as a function of salt concentration for different applied voltages

For electrolysis reactions to occur, a minimum voltage is required between anode and cathode, the so-called decomposition potential. This behavior is associated with the passage of charges through the phase boundary. For most electrolysis reactions the decomposition potential lies within 1 to 4 V [109]. The decomposition potential of a system with Solar Salt must be determined experimentally. For this purpose, a cyclic voltammetry experiment is selected. Cyclic voltammetry is an analytical method that is commonly used to examine various electrode processes. In cyclic voltammetry, first a linearly increasing and then a decreasing potential is applied to a pair of electrodes immersed in an electrolyte. This process is repeated several times, while the current and applied potential differences are measured as a function of time [109].

Figure 4-3 shows the results of a cyclic voltammetry experiment carried out with Solar Salt at 290 °C and 560 °C respectively and two Alloy625 electrodes (more details on the experimental setup can be found in appendix C.2). The 290 °C case shows that a current can be measured first at an applied potential difference of 2 V. Here, a first redox reaction seems to take place, which is however inhibited. At roughly 3.6 V potential difference the current increases in a linear fashion. At 560 °C, the decomposition potential is found at roughly 1.1 V. It can be noticed, that above the decomposition potential the current shows an approximately linear dependency on the applied potential difference. This linear behavior is generally a sign, that the total resistance of the system is dominated by the electrical resistivity of the fluid and that the redox reactions are not a limiting factor in the system at the applied potential differences. Also, it can be noticed, that the slope of the current increases at higher temperatures. This is probably caused by the lower electrical resistivity of the salt at higher temperatures (see chapter 3.5)

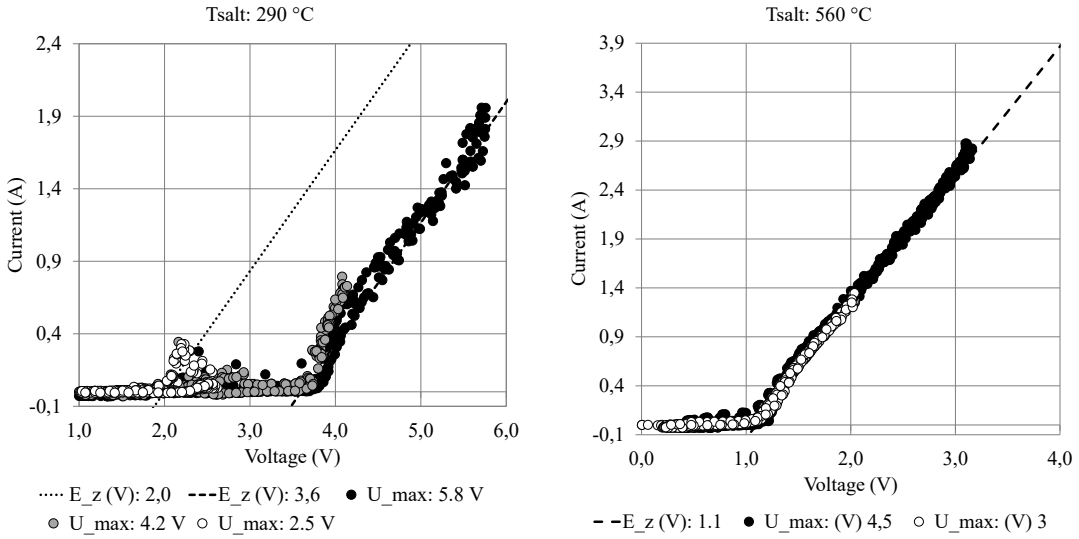


Figure 4-3: Results of cyclic voltammetry experiment with Alloy625 electrodes and Solar Salt

Figure 4-4 shows on the left a representative picture of the Alloy625 electrodes before and after roughly 20 minutes of cyclic voltammetry tests. The formation of a black oxide layer on the anode is observed. In one of the experiments, this layer flaked off completely after air-cooling of the electrodes to ambient temperature. Figure 4-4 on the right shows the Solar Salt after an experiment at 290 °C and 560 °C before complete freezing.


Figure 4-4: Left: Alloy625 electrodes before and after cyclic voltammetry test; Right: Solar Salt after cyclic voltammetry test before completely freezing

In both cases black particles – probably some oxidized metallic species – can be observed in the salt. From these measurements it can be deduced that the application of potential differences above roughly 3.6 V for 290 °C or 1.1 V for 560 °C would provoke redox reactions with formation of a corrosive layer on the electrodes. Also salt decomposition with gaseous oxygen or $NO_x$ formation is possible. As already discussed in chapter 3.4, these effects are suspected to be the source of a decreased heat transfer and should not be additionally provoked in the heat transfer test setup.

However, lowering the applied potential difference below these values proves technically challenging as on one hand the necessary currents to reach 1 MW/m² of heat flux are of the order of magnitude of ~7 kA and at the same time the heating section length has to be reduced (<0.25 m) while wall thickness and diameter of the test tube (50 mm) have to be increased strongly to

reduce the resistance of the tube (>20 mm tube thickness). This again would lead to intolerable high outer wall tube temperatures, strong dependency of measurement uncertainty on tube thermal conductivity and complex electrical contacting.

When an alternating voltage is applied to the electrodes of an electrochemical cell, the so-called electrochemical double layer is formed at the solid-liquid phase boundary by the migration of oppositely charged ions. If an alternating voltage is applied, the double layers at the electrodes are recharged in the rhythm of the alternating voltage. This corresponds to the charging and discharging of capacitors. Consequently, an alternating current can flow without the need for charge to pass through the electrode/electrolyte solution phase boundaries [109]. Ion conduction can be completely inhibited by the application of high frequency.

In a setup with an **induction heater**, a high frequency alternating current (AC) is generated in a solenoid coil, which surrounds the tube with the heat transfer fluid [83]. This alternating coil current causes eddy currents in the test tube and heats the workpiece by the Joule effect. With this method flux densities of 1 MW/m² can be easily achieved [26]. Also, as with the Direct Joule heating concept, the heating power transferred to the tube can be measured by electrical power measurement, which leads to low measurement uncertainty. In addition, the method is applicable to enhanced tubes, analogeous to direct joule heating concepts. Finally, induction heating equipment is commercially available and equipment costs are reasonable.

Another approach for the heating section of heat transfer measurement setups is the usage of a **secondary fluid**. In this approach the test tube is heated using a secondary fluid, which is heated to a certain temperature, required to achieve a certain heat flux through the test tube wall. Chen et al. employed this approach in his measurements with the ternary nitrate salt HITEC up to temperatures of 300 °C [54]. Yu-ting et al. used a setup using a cooling oil for the heat transfer measurement of $LiNO_3$ up to molten salt temperatures of ~400 °C [50]. In order to achieve the desired heat fluxes up to 900 kW/m² and Solar Salt temperatures bulk temperatures around 550 °C, tube outer wall temperatures > 650 °C are necessary in the present setup. Such high temperatures make designs with a secondary fluid and a concentric tube at the required temperatures challenging. Reason for this, is the limited available secondary liquid fluids, that are chemically stable at these temperatures (e.g. sodium, lead-bismuth). The necessary security equipment and necessary measures to prevent corrosion ( [110], [111]) make the setup apparatus complex. Another important downside of this appraoch, is that the heat input into the salt has to be measured using the calorimetric method. This leads to the necessity of long heating sections in order to assure high temperature gradients in the Solar Salt also at high Reynolds numbers.

Das et al. [58] used a **cartridge heater** placed at the inside of a tube in order to measure the forced convective heat transfer. This setup allows the required high flux densities and power input measurement through electric power input measurement. However, with this setup, ultimately the heat transfer in annular flow is measured and has to be transferred to the heat transfer in tube flow using secondary effect corrections [58].

Table 4-1 shows an overview of the advantages and disadvantages of the different heating concepts. Based on this overview, the concept using an induction heater is selected as the most

promising concept as all required boundary conditions can be achieved, (flux density, applicability with enhanced tubes, required Reynolds numbers, tubular flow), relatively good measurement uncertainty can be reached, and the equipment complexity is justifiable.

| **Criteria** | **Concept** | | | | |
|---|---|---|---|---|---|
| | Joule Heating (DC) | Impedance heating | Heating cartridges | Induction heating | Secondary medium |
| Re numbers:<br>10‘000 – 200‘000 | ✓ | ✓ | ✓ | ✓ | ✓ |
| Flux densities:<br>100 – 1000 kW/m² | 1 MW/m² | 1 MW/m² | 1 MW/m² | 1 MW/m² | 1 MW/m² |
| Applicable with enhanced tubes: | ✓ | ✓ | × | ✓ | ✓ |
| Theoretically achievable measurement uncertainty: | ± 2 ... ± 15 % | ± 2 ... ± 15 % | ± 2 ... ± 15 % | ± 2 ... ± 20 % | ± 4... ± 80 % |
| Main factor on measurement uncertainty: | Low uncertainty of outer wall temperature and power measurement (impact of heat conductivity of tube neglected) | Low uncertainty of outer wall temperature and power measurement | Low uncertainty of outer wall temperature and power measurement | Low uncertainty of outer wall temperature and power measurement (additional: uncertainty of cooling water losses) | Low uncertainty of outer wall temperature<br>Measurement of thermal power input can only be performed with calorimetric method |
| Feasibility: | Electrochemical reactions leading to oxide layer and possibly local decomposition of salt with gas formation. High outer wall tube temperatures | High frequencies necessary to inhibit electrochemical reactions. | Annular flow conditions are measured. | High frequency inhibits electrochemical reactions. No major problem | High equipment expenditures. (high pressure steam or sodium) |

Table 4-1: Overview of selection criteria of heating concepts

## 4.2 Experimental Setup

As discussed in the previous section, a cylindrical induction heater setup is chosen as a heating concept.

Figure 4-5 shows the schematic representation of the main test section. The main fluid enters the main test section on the left, where it first flows through a DN50 (ID: 52.48 mm, t: 3.91 mm) tube across a static mixer. After a reducer the medium flows through the hydrodynamic entrance section. As the velocity boundary layer is fully developed in solar receivers (see chapter 3.1) the hydrodynamic entrance length is chosen with a ratio of length to inner diameter of $L_{e,h}/d_i = 55$. Hence it can be assumed that the velocity boundary layer is fully developed before entering the heating section (see chapter 2.2.). After the hydrodynamic entrance length follows the heating section, which is heated by a solenoid induction heating coil ($L_{e,th}/d_i = 20$). After the heating section, the flow passes through a diverter to a DN50 tube comprising another static mixer. The main flow bulk temperature measurement is done by 3 type N thermocouples at the inlet and 3 type N thermocouples at the outlet of the test setup. These sensors are in direct contact with the main fluid flow. Both sets of thermocouples are preceded by a static mixer to achieve a uniform bulk temperature measurement. The thermocouples are immersed over a length of ~ 37 mm, which equals roughly 12 times the thermocouple diameter. In the heating section, 32 type N thermocouples are welded to the outer tube wall by a micro laser beam weld to maximize the thermal contact between thermocouple and tube. For these thermocouples, firstly, a small diameter (0.5 mm) was chosen, and the sensors were oriented so that they were at a right angle to the induced current direction. Furthermore, they were galvanically separated from the rest of the sensors. With this approach, the impact of the electromagnetic field can be inhibited. The placement of the thermocouples can be found in appendix F.1. The whole test section is insulated using 300 mm of refractory ceramic fiber mats.

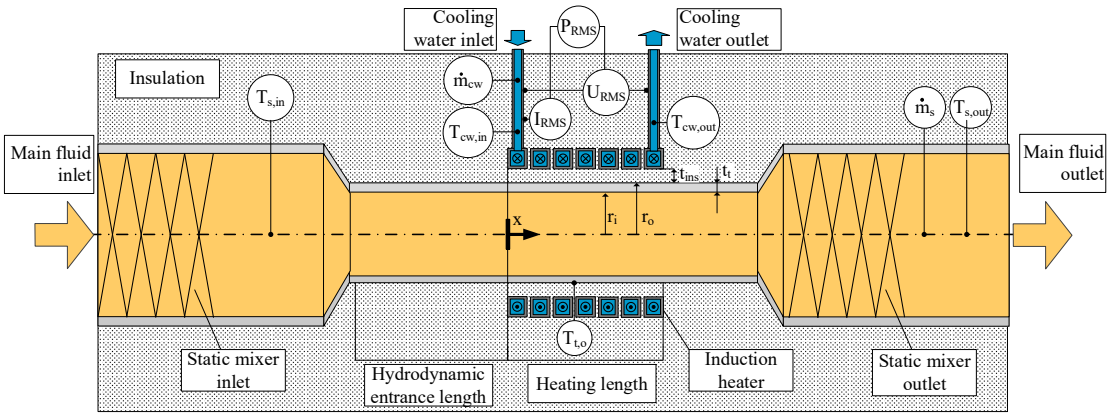


Figure 4-5: Schematic representation of the main test section

The austenitic stainless steel of the type 1.4878 is selected as tube material for the test section. Several studies on the corrosion rates in Solar Salt exist for this material for different immersion times, temperatures, and salt impurities, as summarized in Figure 4-6. For a test duration of 600 hours and a corrosion rate of roughly 40 µm/year one can expect a corrosion layer < 3 µm. This

was deemed acceptable. In addition, the austenite stainless steel is a paramagnetic material. This leads to a lower efficiency of the induction heating process. On the other hand, more importantly no non-linear effects of the magnetic properties have to be expected (see chapter 2.4). The selection of the spirally grooved tube geometry and measurement of the as-built geometric properties can be found in appendix 0.

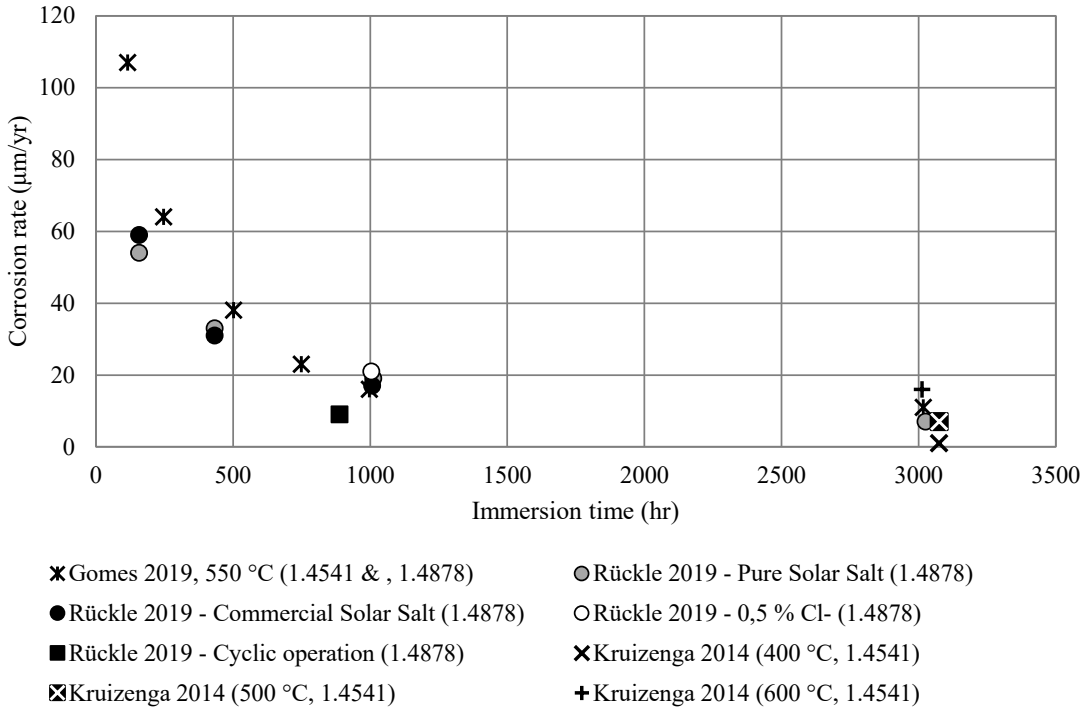


Figure 4-6: Overview of corrosion rates of steel types 1.4878 and 1.4541 in Solar Salt as a function of immersion time of different authors [112], [113], [114]

The solenoid induction heater must be water-cooled to prevent overheating at high flux densities. A frequency of 8600 Hz was chosen for the induction heater, yielding theoretical penetration depth in a semi-infinite body of 4.6-5.6 mm (see also chapter 2.4). The inlet and outlet cooling water temperature is measured each by 3 type K FEP[III] -insulated thermocouples. The cooling water mass flow is measured by a Heinrichs TMU-010 Coriolis sensor. The active current of the induction heater is measured using a Chauvin-Arnoux MA-200 Rogowski coil, the active voltage by an R&S RT-ZI10 passive probe. Both signals are monitored and processed using an R&S RTH1002 oscilloscope. The whole test section is insulated using silica fiber wool. Table 4-2 summarizes the specifications and uncertainties related to geometric properties of the tube. Further pictures and technical drawings of the test setup can be found in appendix D.

All used thermocouples are calibrated with their respective evaluation unit (thermal line + SPS) using an Ametek ATC650B dry block calibrator. For calibration, the readings of a PT1000 temperature reference sensor (model STS-100 A 901) is used. The calibrator and PT1000 sensor

[III] FEP: Fluorinated ethylene propylene

are calibrated and adjusted prior to thermocouple calibration by an accredited institution (ISO17025, DANAK). The calibrator has a combined uncertainty tested by the manufacturer as ±0.11 K (k=2), this translates to a Gaussian uncertainty of $\sigma_{calibrator} = \pm 0.055$ K. To minimize uncertainties, pairs of thermocouples which measure a temperature difference are calibrated simultaneously.

| **Parameter** | **Smooth tube test setup** | **Spirally grooved tube test setup** |
|---|---|---|
| Outer diameter tube $d_o$ | 26.9 ±0.3 mm | |
| Tube wall thickness $t_t$ | 2.0 ±0.1 mm | |
| Groove height e | / | 0.4 mm ±0.05 mm |
| Pitch length p | / | 20.9 mm ±0.1 mm |
| Pitch angle α | / | 73.8° |
| Hydrodynamic entrance length | 1250 mm | |
| Heating length $l_{heat}$ | 470 mm ±18 mm | |
| Thickness of insulation between induction heater and tube test section $t_{ins}$ | 15 mm ±5 mm | |
| Outer insulation thickness | ~300 mm | |
| Number of turns of solenoidal heating coil | 40 | |
| Inner radius of solenoidal heating coil $r_{ind}$ | 30 mm | |

Table 4-2: Geometric specification main test section

The molten salt test setup utilizes the test infrastructure of the DLR TESIS:com plant (Cologne) (see Figure 4-7 and Figure 4-8: molten salt test setup with generator, induction heater and heat rejection) [115]. The testing infrastructure consists of two molten salt tanks, each able to hold 20 t of Solar Salt. The salt can be heated or cooled to the desired temperature before passing through a test bench. Each molten salt tank is equipped with an E+H Micropilot FMR54 radar level sensor, which has been calibrated using a Coriolis sensor and water. The tank deformation at higher temperature has been accounted for using a detailed FEM simulation of the tank and the salt to precisely track the salt inventory. In addition, the solar salt mass flow is measured using three serially placed FLEXIM WI-400 ultrasonic clamp-on mass flow sensor. The salt mass flow measurement system has been validated with Solar Salt up to 400 °C using a high temperature KROHNE Optimass 6400 Coriolis sensor. A generator provides the power to the induction heater. The induction heater is also cooled by the cooling water circuit. The cooling water circuit rejects heat by a water-to-air cooler. The pressure is measured at the inlet and at the outlet of the TESIS:com test section (see Figure D-4 in appendix D). The pressure measurement at the inlet is composed of a vertically connected tube in which an air blanket acts as a thermal insulation between the molten salt and the diaphragm seal of the pressure transmitter (Endress & Hauser

PMP 75). The pressure transmitter and the diaphragm seal are thermally disconnected by an oil-filled capillary tube. The used oil is only stable up to 400 °C. The outlet pressure is measured with a Gems Sensors & Controls 3500 Series pressure sensor. Again, an air cushion is used to protect the sensor from the high salt temperatures.

Measurements with water as the main fluid are used to validate the measurement setup for the forced convective heat transfer of Solar Salt in a smooth tube. For the water setup, the smooth tube test section is integrated to a water setup. The water tests are conducted prior to the molten salt tests. The water validation test setup uses the same data acquisition system as the final molten salt system. More information on the water test setup can be found in appendix D. The main water flow in the water setup is measured by a Proline Promass 83F Coriolis Sensor by Endress+Hauser. The measurement equipment uncertainty of the Coriolis sensor of $\delta_{\dot{m}_s,meas}$=±0.15%, as stated by the manufacurer is experimentally confirmed using a platform scale IKT 150K1L by KERN & Sohn GmbH.

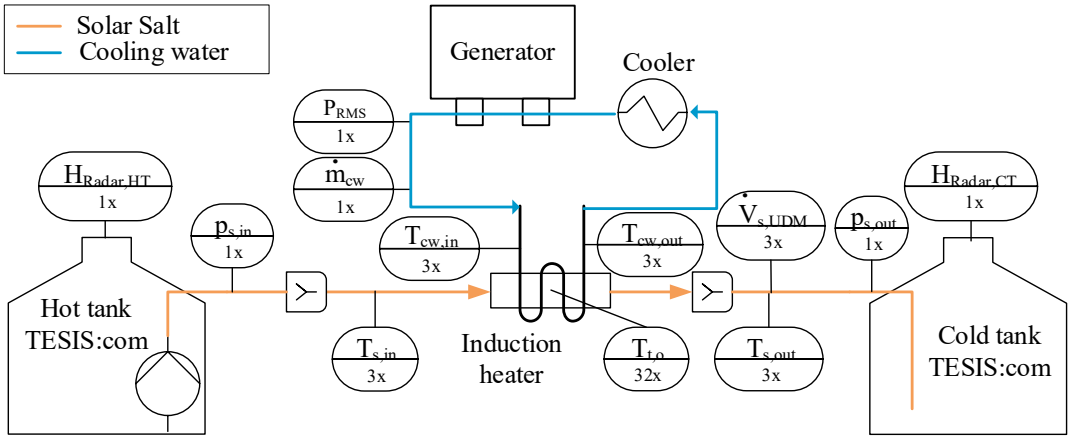


Figure 4-7: Simplified piping and instrumentation diagram of the experimental system Solar Salt loop

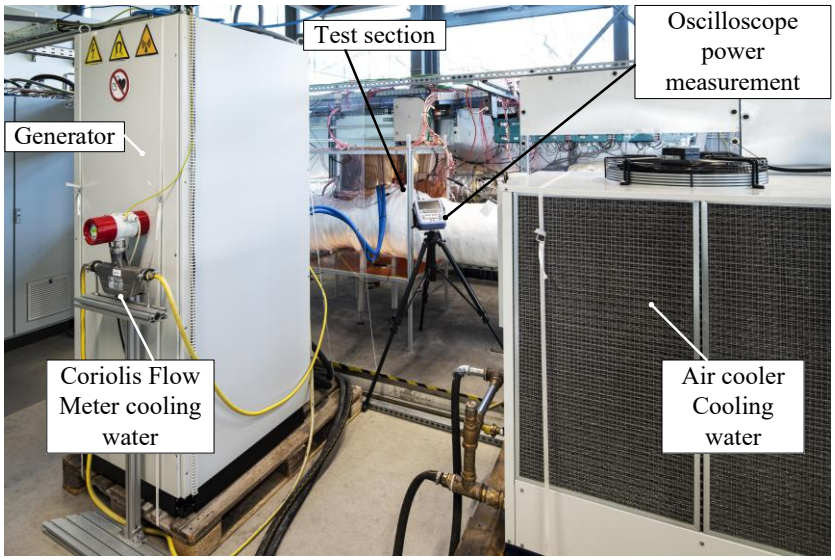


Figure 4-8: molten salt test setup with generator, induction heater and heat rejection

# 4.3 Deduction of Nusselt Number

The Nusselt number cannot be measured directly but must be derived from several measured variables. This chapter describes the derivation of the Nusselt number from the measured values. This chapter is adapted from an article that was published beforehand by the author [22]. Applying the energy balance to the differential control volume shown in Figure 4-9 leads to the following general form of the heat equation [14]. Where $\lambda_t$ is the thermal conductivity of the tube, $\rho_t$ is the density of the tube and $c_{p,t}$ is the specific heat capacity of the tube. $w$ is the volumetric heating density in W/m³. The definition of the coordinates $r, \theta$ and $x$ can be found in Figure 2-1 and Figure 4-9.

$$\frac{1}{r}\frac{\partial}{\partial r}\left(\lambda_t r \frac{\partial T_t}{\partial r}\right) + \frac{1}{r^2}\frac{\partial}{\partial \theta}\left(\lambda_t \frac{\partial T_t}{\partial \theta}\right) + \frac{\partial}{\partial x}\left(\lambda_t \frac{\partial T_t}{\partial x}\right) + w = \rho_t c_{p,t} \frac{\partial T_t}{\partial t} \tag{4.1}$$

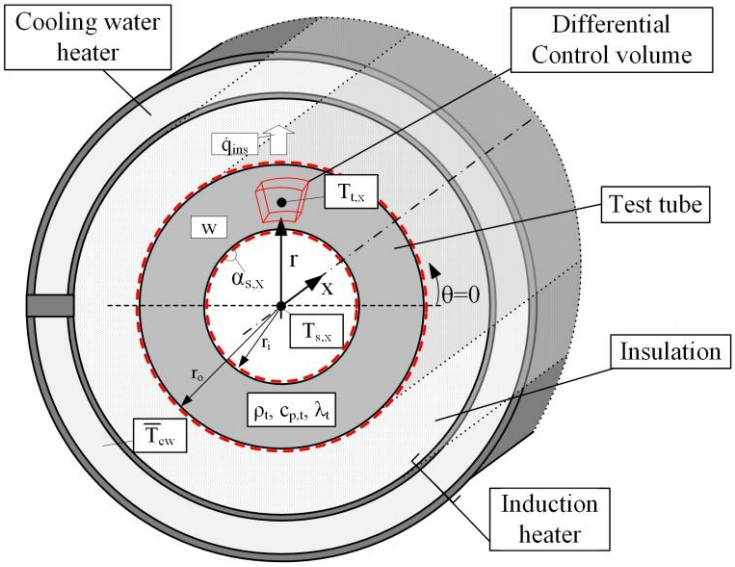


Figure 4-9: Position and boundary condition of differential control volume $\mathrm{d}r \cdot r\mathrm{d}\theta \cdot \mathrm{d}x$

Stationary conditions can be assumed as the test procedure is designed to ensure steady state conditions. For more details see appendix G.2 and chapter 4.6. Regarding the induction heating, a thin-walled cylinder relative to its diameter $d_o/t \geq 10$ and the penetration depth $t_t/\delta \leq 0.2$ of the magnetic field is assumed. Hence, a constant volumetric heating density $w$ is assumed over the radial direction of the tube. This also applies axially as the cylindrical induction heater's diameter is approximately one order of magnitude smaller than its length which leads to a homogeneous magnetic field. Furthermore, heat conduction in circumferential direction in the tube can be omitted because of the symmetric heating of the system. Heat conduction in the axial direction in the tube wall at the boundary was found to be several orders of magnitudes lower than the power transferred in radial direction, therefore it will be neglected. Furthermore, heat

conduction in flow direction can be neglected, because the Péclet number is >>1 over the full range of experiments. Finally, a radially constant thermal conductivity $\lambda_t$ is assumed. Consequently, the general equation (4.1) can be simplified to the following heat balance:

$$\frac{1}{r}\frac{d}{dr}\left(r\frac{dT_{t,x}}{dr}\right)+\frac{w}{\lambda_t}=0 \tag{4.2}$$

After variable separation and solving the integrations, the general solution for the temperature distribution in the test tube becomes:

$$T_{t,x}(r)=-\frac{w\cdot r^2}{4\lambda_t}+C_1\ln(r)+C_2$$

To obtain the two constants of integration $C_1$ and $C_2$ the two boundary conditions are applied: Heat losses through the insulation of the tube to the induction heater (equation (4.3)) and convective heat transfer to the molten salt at the inner side of the tube (equation (4.4)).

$$-\lambda_t\cdot\frac{d}{dr}T_{t,x}(r)\Big|_{r=r_o}=\dot{q}_{ins} \tag{4.3}$$

$$-\lambda_t\cdot\frac{d}{dr}T_{t,x}(r)\Big|_{r=r_i}=-h_{s,x}\cdot\left(T_{t,x}(r=r_i)-T_{s,x}\right) \tag{4.4}$$

The heat losses to the induction heater through the tube insulation $\dot{q}_{ins}$ are measured using the temperature difference between the tube outer wall $T_{t,o,x}$ and the mean cooling water temperature $\bar{T}_{cw}$ of the induction heater.

$$\dot{q}_{ins}=\frac{\lambda_{isol}}{r_o\cdot\ln\left(\frac{r_{ind}}{r_o}\right)}\cdot\left(T_{t,o,x}-\bar{T}_{cw}\right) \tag{4.5}$$

Applying the boundary conditions and solving for $T_{t,x}(r)$ leads to the following expression:

$$T(r)=-\frac{w\cdot r^2}{4\lambda_t}+\left(\frac{-\dot{q}_{ins}\cdot r_o}{\lambda_t}+\frac{w\cdot r_o^2}{2\lambda_t}\right)\ln(r)+\frac{1}{h_{s,x}}\left[-\frac{w\cdot r_i}{2}-\frac{\dot{q}_{ins}\cdot r_o}{r_i}+\frac{w\cdot r_o^2}{2\cdot r_i}\right]+\frac{w\cdot r_i^2}{4\lambda_t}$$
$$-\left(\frac{-\dot{q}_{ins}\cdot r_o}{\lambda_t}+\frac{w\cdot r_o^2}{2\lambda_t}\right)\ln(r_i)+T_{s,x}$$

The temperature of the tube will be measured at the location $r=r_o$ in order not to disturb the inner fluid flow. Hence the temperature at $T_t(r=r_o)$ is inserted and the equation is solved for $\alpha_{s,x}$.

$$h_{s,x}=\frac{2\lambda_t\left[w\left(r_o^2-r_i^2\right)-2r_o\dot{q}_{ins}\right]}{r_i\left[4\lambda_t\left(T_{t,o,x}-T_{s,x}\right)+2r_o ln\left(\frac{r_o}{r_i}\right)\left(2\dot{q}_{ins}-wr_o\right)+w\left(r_o^2-r_i^2\right)\right]} \tag{4.6}$$

With the general definition for the local Nusselt number [19]:

$$Nu_{s,x}=\frac{h_{s,x}\cdot 2r_i}{\lambda_s} \tag{4.7}$$

The final expression for the local Nusselt number becomes:

$$Nu_{s,x} = \frac{4\lambda_t\left[w\left(r_o^2 - r_i^2\right) - 2r_o\dot{q}_{ins}\right]}{\lambda_s \cdot \left[4\lambda_t\left(T_{t,o,x} - T_{s,x}\right) + 2r_o ln\left(\frac{r_o}{r_i}\right)(2\dot{q}_{ins} - wr_o) + w\left(r_o^2 - r_i^2\right)\right]} \tag{4.8}$$

All material properties of the salt are evaluated at mean bulk salt temperature. The mean Nusselt number is defined as follows. Δx is the length of one discrete element of the heating length and $n_x$ is the number of measurement points along the heating length.

$$Nu_{s,m} = \frac{\int_0^{l_{heat}} Nu_{s,x}\mathrm{d}x}{l_{heat}} \approx \frac{1}{l_{heat}}\left[\sum_1^{n_x} Nu_{s,x} \cdot \Delta x\right] \tag{4.9}$$

The volumetric inductive heating density of the tube is defined with $w = P_t/V_t$. Two measurement approaches are used to deduce the power transferred by the induction heater to the tube: the "calorimetric method" and the "electrical method".

### 4.3.1 Calorimetric method

The first approach measures the volumetric heating density of the tube and considers the energy balance of the main fluid flow. This approach will be referred to as the "calorimetric method". For the calorimetric method, the energy balance over the molten salt is set up for the control volume shown in Figure 4-10. Steady state conditions are assumed.

$$P_{t,el}^{cal} = \dot{m}_s \cdot \bar{c}_{p,s}(\bar{T}_s) \cdot \left(T_{s,out} - T_{s,in}\right) + \dot{Q}_{ins} + \dot{Q}_{t,\infty} \tag{4.10}$$

Here, $\dot{m}_s$ is the salt mass flow, $\bar{c}_{p,s}(\bar{T}_s)$ is the specific heat capacity of Solar Salt at mean bulk salt temperature and $\left(T_{s,out} - T_{s,in}\right)$ is the temperature gradient between bulk salt outlet and inlet temperature in the test section. $\dot{Q}_{ins}$ is the thermal power which is transferred from the test tube to the inductor coil by heat conduction through the insulation in the gap between induction heater and test tube. $\dot{Q}_{t,\infty}$ are the thermal losses from the test tube to the ambient, other than the heat losses to the inductor coil.

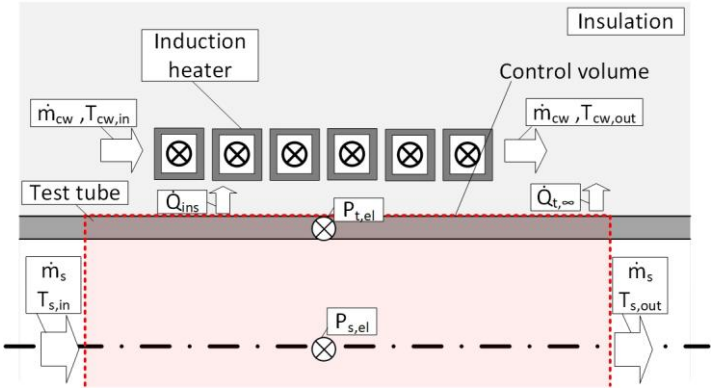


Figure 4-10: Heat flows and system boundaries of the energy balance according to the "calorimetric method" [22]

To decrease systematic measurement errors, the temperature gradient across the testing section is measured in the main fluid and the cooling water before and after the heating interval. These data are obtained during the homogenization period, which is conducted before and after each heating interval and in which the test section is flown through with the respective salt mass flow but the tube is not heated by the induction heater (see chapter 4.6). With this method the thermal losses over the test section $\dot{Q}_{t,\infty}$ to ambient can be deduced and thus transient effects and systematic errors can be minimized. For the evaluation, a temperature difference $\Delta T_{calib,s}$ is calculated that leads to the losses to ambient $\dot{Q}_{t,\infty} \equiv 0$ using the measurement data from the periods without heating ($P_{t,el} = 0$):

$$\left.\begin{aligned} &\dot{m}_s \cdot \bar{c}_{p,s}(\bar{T}_s) \cdot \left(T_{s,out} - T_{s,in} + \Delta T_{calib,s}\right) + \dot{Q}_{ins} + \overbrace{\dot{Q}_{t,\infty}}^{\equiv 0} = 0 \\ &\Leftrightarrow \Delta T_{calib,s} = -\frac{\dot{Q}_{ins}}{\dot{m}_s \cdot \bar{c}_{p,s}(\bar{T}_s)} - \left(T_{s,out} - T_{s,in}\right) \end{aligned}\right| \quad \forall\, P_{t,el} = 0 \qquad (4.11)$$

For the water tests the temperature difference between cooling water and main water before and after heating at a stationary state is lower than $\Delta T = 20$ K. Assuming the heating length $l_{heat}$, the wall thickness of the insulation and conductivity of the insulation, this leads to an exchanged power between cooling circuit and main circuit of less than 5 W. This would theoretically lead to a temperature difference of below 0.01 K in the cooling water circuit and well below 0.002 K even at the lowest water mass flows in the main water circuit. As a result, the impact of the heat flow between cooling water and main water flow can be neglected for the calibration of the water setup $\dot{Q}_{ins|P_{t,el}=0} \cong 0$.

For the salt setup, the expected transferred power between cooling water and salt ranges between 50 W (at 300 °C salt temperature) and 100 W (at 550 °C salt temperature). This corresponds to a temperature difference ranging between 0.07 K and 0.13 K in the cooling water circuit and a temperature difference ranging between 0.05 K and 0.1 K for the molten salt circuit when assuming a mass flow of 0.8 kg/s. Therefore, the heating losses to the induction heating coil are considered during the homogenization periods.

The heat losses between the test tube and the inductor coil are calculated by solving the Fourier equation for a cylindrical body. The heat losses to the induction heater $\dot{Q}_{ins}$ represent less than 1% of the power transferred to the salt and low values of the partial derivative $\partial Nu/\partial \dot{Q}_{ins}$ lead to a low impact on the overall uncertainty of the Nusselt number, for these reasons an average cooling water temperature ($\bar{T}_{cw} = 1/6 \cdot \left(\sum_{k=1\ldots3} T_{cw,in_k} + \sum_{k=1\ldots3} T_{cw,out_k}\right)$ is used to calculate $\dot{Q}_{ins}$.

$$\dot{Q}_{ins} = \frac{\lambda_{ins}}{r_o \cdot \ln\left(\frac{r_{ind}}{r_o}\right)} \cdot 2\pi r_o \cdot l_{heat} \cdot \left(T_{t,o} - \bar{T}_{cw}\right) \tag{4.12}$$

In a final step, the relation for the power transferred to the tube based on the calorimetric method is given by equation (4.13).

$$P_{t,el}^{cal} = \dot{m}_s \cdot \bar{c}_{p,s}(\bar{T}_s) \cdot \left(T_{s,out} - T_{s,in} + \Delta T_{calib,s}\right) + \dot{Q}_{ins} \tag{4.13}$$

### 4.3.2 Electrical method

The second method measures the power transferred by the induction heater to the tube by regarding the energy balance of the cooling water loop combined with the measurement of the active power. This approach will be referred to as the "electrical method". In a first step, the energy balance in the control volume shown in Figure 4-11 is formed based on the principle of energy conservation and assuming steady state conditions.

$$P_{c,el} + \dot{Q}_{ins} - \dot{m}_{CW} \cdot \bar{c}_{p,cw}(\bar{T}_{cw}) \cdot \left(T_{cw,out} - T_{cw,in}\right) - \dot{Q}_{c,\infty} = 0 \tag{4.14}$$

Here, $P_{c,el}$ is the thermal power transferred to the induction coil trough ohmic losses produced by the induction heating process. $\dot{Q}_{ins}$ is the thermal power which is transferred from the test tube to the inductor coil by heat conduction through the insulation in the gap between induction heater and test tube. $\dot{m}_{CW} \cdot \bar{c}_{p,cw}(\bar{T}_{cw}) \cdot \left(T_{cw,out} - T_{cw,in}\right)$ is the thermal power removed from the inductor coil by the cooling water and $\dot{Q}_{c,\infty}$ are the thermal losses from the induction coil to ambient through the outer insulation. Because of the water cooling, the temperature gradient between ambient and induction coil is not very high (< 40 K). Assuming a silica fibre insulation around the induction heater with a thickness of >100 mm leads to heat fluxes of < 35 W/m² or, considering the area, less than 10 W over the heating section. Consequently, the losses to ambient will be neglected further on.

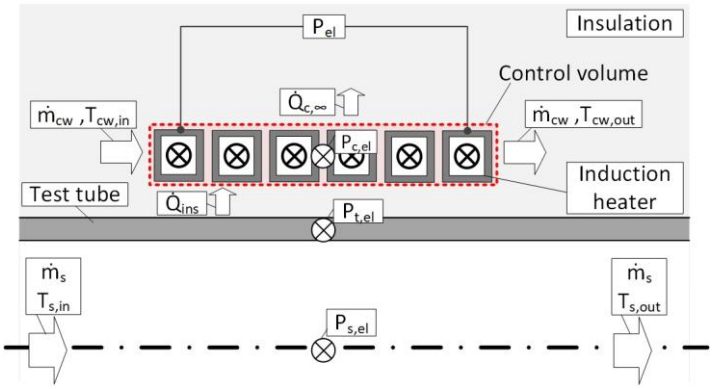


Figure 4-11: Heat flows and system boundaries of the energy balance according to the "electrical method"

Next, the measured active power across the induction heater $P_{\mathrm{el}}$ equals the sum of the active power induced by the induction heater in the test tube $P_{\mathrm{t,el}}$, the active power transferred to the induction coil over the heating section $P_{\mathrm{c,el}}$ and the active power induced by the induction heater in the main fluid $P_{\mathrm{s,el}}$ (e.g. Solar Salt or water).

$$P_{\mathrm{el}} = P_{\mathrm{t,el}} + P_{\mathrm{c,el}} + \overbrace{P_{\mathrm{s,el}}}^{\ll} \qquad \text{with: } P_{\mathrm{el}} = U_{\mathrm{RMS}} \cdot I_{\mathrm{RMS}} \cdot \cos(\varphi) \tag{4.15}$$

Solar Salt is a poor electrical conductor – although much better than water – consequently $P_{\mathrm{s,el}}=0$ is assumed in the following (for more details see appendix G). $U_{\mathrm{RMS}}$ is the root mean square potential difference between inlet and outlet of the induction coil and $I_{\mathrm{RMS}}$ is the root mean square current through the induction heater. $\varphi$ is the phase angle between the induction coil current and voltage, $\cos(\varphi)$ is the so-called power factor of the induction coil.

The heat flow $\dot{Q}_{\mathrm{ins}}$ between the test tube and the inductor coil is derived analogeously to the calorimetric method, described in detail in the section above. Inserting equation (4.15) into equation (4.14) and rearranging for $P_{\mathrm{t,el}}$ leads to the relationship for the active power transferred into the test tube:

$$P_{\mathrm{t,el}}^{\mathrm{el}} = U_{\mathrm{RMS}} \cdot I_{\mathrm{RMS}} \cdot \cos(\varphi) - \dot{m}_{\mathrm{CW}} \cdot \bar{c}_{\mathrm{p,cw}}(\bar{T}_{\mathrm{cw}}) \cdot \left(T_{\mathrm{cw,out}} - T_{\mathrm{cw,in}}\right) + \frac{\lambda_{\mathrm{ins}}}{r_{\mathrm{o}} \cdot \ln\left(\frac{r_{\mathrm{ind}}}{r_{\mathrm{o}}}\right)} \cdot 2\pi r_o \cdot l_{\mathrm{heat}} \cdot \left(T_{\mathrm{t,o}} - \bar{T}_{\mathrm{cw}}\right) \tag{4.16}$$

Unfortunately, the measurement of the phase angle with the oscilloscope suffered of low reproducibility. Therefore, the power factor of the induction heater system is deduced by equating the thermal power transferred to the tube using the electrical method and the calorimetric method, thus solving $P_{t,el}^{el} = P_{t,\mathrm{el}}^{cal}$; leading to the expression for the power factor.

$$\cos(\varphi) = \frac{\dot{m}_s \cdot \bar{c}_{p,s}(\bar{T}_s) \cdot \left(T_{s,out} - T_{s,in} + \Delta T_{calib,s}\right) + \dot{m}_{CW} \cdot \bar{c}_{p,CW}(\bar{T}_{Cw}) \cdot \left(T_{CW,out} - T_{CW,in}\right)}{U_{RMS} \cdot I_{RMS}} \tag{4.17}$$

## 4.4 Reference Nusselt Number

The Nusselt number derived from the experiments will be compared to the Nusselt number calculated from known correlations. This chapter describes the calculation of the reference Nusselt number. In this work, the Nusselt number based on measured parameters will be compared to the correlation proposed by Gnielinski [18]:

$$Nu_{x,REF} = \frac{\xi/8 \cdot Re \cdot Pr}{1 + 12.7 \cdot \sqrt{\xi/8}(\mathrm{Pr}^{2/3} - 1)} \left[1 + \frac{1}{3}\left(\frac{2r_i}{x}\right)^{2/3}\right] \left[\frac{Pr}{Pr_{t,i}}\right]^{0.11}$$
$$\xi = (1.8 \cdot \log_{10}(Re) - 1.5)^{-2}$$

All salt properties are evaluated at mean fluid temperature $\bar{T}_{s,m} = \frac{(T_{s,out}+T_{s,in})}{2}$. For the calculation of the film Prandtl number $Pr_{t,i}$, the inner wall temperature $T_{t,i}$ of the tube has to be deduced. The Prandtl number is defined as a function of the mean inner wall temperature

$$Pr_{t,i} \equiv f(\bar{T}_{t,i})$$

$$\text{with } \bar{T}_{t,i} = \frac{1}{l_{heat}} \cdot \int_0^{l_{heat}} T_{t,i,x}\mathrm{d}x$$

Furthermore, it is defined:

$$\dot{q}_s = \alpha_m \cdot \Delta T_{log} = \frac{Nu_m \cdot \lambda_s}{2r_i} \cdot \Delta T_{log}$$
$$\Delta T_{log} = \frac{\left(\bar{T}_{t,i} - T_{s,in}\right) - \left(\bar{T}_{t,i} - T_{s,out}\right)}{\ln\left(\frac{\bar{T}_{t,i} - T_{s,in}}{\bar{T}_{t,i} - T_{s,out}}\right)}$$

Here, $\dot{q}_s$ is the thermal flux density transferred to the salt and $\Delta T_{log}$ is the logarithmic temperature difference. When combining with the equation for $Nu_{x,REF}$ and rearranging for $\bar{T}_{t,i}$ this yields the correlation for $\bar{T}_{t,i}$:

$$\bar{T}_{t,i} = \frac{T_{s,out} \cdot e^{T_{s,out} \cdot \alpha_m/\dot{q}_s} - T_{s,in} \cdot e^{T_{s,in} \cdot \alpha_m/\dot{q}_s}}{e^{T_{s,out} \cdot \alpha_m/\dot{q}_s} - e^{T_{s,in} \cdot \alpha_m/\dot{q}_s}} \tag{4.18}$$

The thermal entrance length has a relevant impact on the Nusselt number based on measured parameters. However, in the measurement setup the first few millimeters of the entrance length will not be evaluated. To enable a correct comparison, the mean Nusselt number deduced from the experiments is compared to the expected mean Nusselt number over the test section:

$$Nu_{m,REF} = \int_0^{l_{heat}} \frac{1}{l_{heat}} Nu_{x,REF}\,\mathrm{d}x = \overbrace{\int_0^{x_0} \frac{1}{x_0} Nu_{x,REF}\,\mathrm{d}x}^{Nu_{m,REF,0\ldots x_0}} + \overbrace{\int_{x_0}^{l_{heat}} \frac{1}{l_{heat} - x_0} Nu_{x,REF}\,\mathrm{d}x}^{Nu_{m,REF,x_0\ldots l_{heat}}}$$

Solving the integral leads to the following reference correlation for the mean expected Nusselt

number in the test section. The measured mean Nusselt number described in the previous paragraph will be compared to the values obtained with equation (4.19).

$$Nu_{m,REF,x_0\ldots l_{heat}} = \frac{1}{l_{heat}-x_0}\left[\frac{\xi/8\cdot Re\cdot Pr}{1+12.7\sqrt{\xi/8}(\mathrm{Pr}^{2/3}-1)}\left[\frac{Pr}{Pr_{t,i}}\right]^{0.11}\left[(2r_i)^{2/3}\left(\sqrt[3]{l_{heat}}-\sqrt[3]{x_0}\right)-x_0+l_{heat}\right]\right] \tag{4.19}$$

# 4.5 Deduction of Friction Factor

The measured pressure difference is defined as follows:

$$\Delta p_{\mathrm{s,total}} = p_{\mathrm{s,o}} - p_{\mathrm{s,i}} \tag{4.20}$$

The pressure difference measurement measures not only the pressure difference between the inlet and outlet of the test tube, but the section in between includes several components (tubing, reducers, static mixers, elbows; for details see appendix G.3). The overall pressure difference can also be written as:

$$\Delta p_{\mathrm{s,total}} = \Delta p_{\mathrm{s,t}} + \Delta p_{\mathrm{per}}$$

where $\Delta p_{s,t}$ is the pressure difference in the test tube and $\Delta p_{per}$ is the sum of pressure differences of all peripheral components. The detailed deduction of $\Delta p_{per}$ can be found in appendix G.3.

The friction factor $\zeta$ of the test section is deduced by rearranging the general correlation for pressure difference of single-phase flow in a tube [19].

$$\zeta = \frac{\left(\Delta p_{s,t}\right)\cdot 4r_i}{l_t\rho_s u_s^2} = \frac{\left(\Delta p_{s,total}-\Delta p_{per}\right)\cdot 4\pi^2\cdot(r_o-t_t)^5\cdot\rho_s}{l_t\dot{m}_s^2} \tag{4.21}$$

Where $l_t$ is the total length of the test tube, including the hydrodynamic entrance length. The final goal is to deduce the ratio of friction factor between the smooth and the spirally grooved tube. The friction factor ratio is defined as the ratio between the deduced friction factor of the grooved tube $\zeta_a$ and the smooth tube $\zeta_0$. The geometric terms $4\pi^2\cdot(r_o-t_t)^5/l_t$ can be reduced as they are constant in both tubes. It must be noted that the inner diameter of the tube is not physically constant for both setups, but by convention.

$$\frac{\zeta_a}{\zeta_0} = \frac{\left(\frac{\left(\Delta p_{s,total}-\Delta p_{per}\right)\cdot\rho_s}{\dot{m}_s^2}\right)_a}{\left(\frac{\left(\Delta p_{s,total}-\Delta p_{per}\right)\cdot\rho_s}{\dot{m}_s^2}\right)_0} \tag{4.22}$$

The term $\rho_s/\dot{m}_s^2$ can be reduced in the calculations, where the friction factor of the smooth tube is calculated using deduced correlations. For calculations employing pairs of measurement results, $\rho_s/\dot{m}_s^2$ is not exactly the same and is considered as a part of the uncertainty calculation.

## 4.6 Test Procedure and Measurement Plan

In a first step, the test section is integrated into a setup which uses water as the main fluid. The measurement campaign with water is used to validate the test setup. This can be done because the forced convective heat transfer of water in a smooth tube is relatively well-known [18]. A description of the water setup can be found in chapter 4.2 and appendix D. The measurement campaign with water starts at the beginning of the day with the initial homogenization phase. A constant mass flow is set through the test setup until a constant temperature difference forms over the test track. As the water temperatures are relatively close to the ambient temperature (max. 40 °C), the homogenization period is less than the periods necessary for the salt setup. After the initial homogenization phase follows the calibration phase. Then during the heating, the desired main water mass flow for the measuring point is set. After the calibration phase follows the heating phase in which the induction heater is activated, while maintaining the same main water mass flow. After the heating period follows another calibration phase analogous to the calibration phase prior to the heating phase. The last three phases are repeated for each measurement point. A detailed description of the test procedure can be found in . An overview of the different main water mass flows and heat fluxes for the water tests can be found in appendix D.

After completion of the validation measurements with water as the main fluid the smooth tube test section is transferred to the molten salt setup. A description of the molten salt setup can be found in chapter 4.2 and appendix D. To minimize transient heat loss effects on the measurement results, the TESIS:com plant and its salt inventory as well as the test setup is heated to the desired salt temperature using an electrical trace heating system. Three main salt temperatures are selected for the test campaign: 300 °C, 400 °C and 550 °C. The salt temperature is adapted during the "Electrical heating phase", usually over the course of one or two days. Analogous to the water tests, an initial homogenization phase precedes all tests. This phase lasts at least 60 minutes (see appendix G.2 for discussion). Analogous to the water tests, the initial homogenization phase is followed by the calibration phase before heating, the heating phase and the calibration phase after heating at the respective main mass flow $\dot{m}_s$, main fluid temperature $T_s$ and heat flux $\dot{q}_s$. After completion of those three phases, the set points of either main mass flow or heat flux is changed, and the next measurement point is measured. During one test day, the inlet salt temperature is kept constant. The molten salt is pumped from one tank of the TESIS:com plant into the second tank to enable mass flow measurement using the radar level sensors. A detailed description of the test procedure can be found in . After completion of the test campaign with the smooth tube, the tests are repeated with the spirally grooved tube. A goal test matrix is shown in Table 4-3. An overview of measured ranges of main measurement quantities and derived quantities can be found in Table 4-4.

<table>
<tr><th>Goal main mass flow $\dot{m}_s$</th><th>Goal main salt temperature: $T_s = 300$ °C</th><th>Goal main salt temperature: $T_s = 400$ °C</th><th>Goal main salt temperature: $T_s = 550$ °C</th></tr>
<tr><td>≈ 0.8 kg/s</td><td rowspan="4">Goal heat flux $\dot{q}_s$:<br>300, 600, 900 kW/m²</td><td>Goal heat flux $\dot{q}_s$:<br>300, 600 kW/m²</td><td rowspan="2">Goal heat flux $\dot{q}_s$:<br>300, 600 kW/m²</td></tr>
<tr><td>≈ 2.1 kg/s</td><td rowspan="3">Goal heat flux $\dot{q}_s$:<br>300, 600, 900 kW/m²</td></tr>
<tr><td>≈ 3.4 kg/s</td></tr>
<tr><td>≈ 4.7 kg/s</td><td rowspan="2">Goal heat flux $\dot{q}_s$:<br>300, 600, 900 kW/m²</td></tr>
<tr><td>≈ 6 kg/s</td></tr>
</table>

Table 4-3: Goal test matrix molten salt test setup with smooth and spirally grooved tube

| Item | Water Setup | Solar Salt Setup |
|---|---|---|
| **Measured quantities** | | |
| Main fluid mass flow: $\dot{m}_s$ | 0.94 – 3.18 kg/s | 0.558 – 5.813 kg/s |
| Cooling water mass flow: $\dot{m}_{cw}$ | 0.157 – 0.160 kg/s | 0.172 – 0.174 kg/s |
| Main fluid inlet temperature: $T_{s,in}$ | 11 – 46 °C | 296 – 554 °C |
| Main fluid temperature gradient: $\Delta T_s$ | 1 – 7 K | 1 – 30 K |
| Outer wall temperature: $T_{t,o}$ | 80 – 150 °C | 333 – 667 °C |
| Cooling water inlet temperature: $T_{CW,in}$ | 24 – 28 °C | 24 – 28 °C |
| Cooling water temperature gradient: $\Delta T_{cw}$ | 7 – 16 K | 5 – 15 K |
| RMS voltage $U_{RMS}$ | 290 – 445 V | 252 – 461 V |
| RMS current $I_{RMS}$ | 548 – 831 A | 465 – 841 A |
| **Derived quantities** | | |
| Heat flux to main fluid: | 420 - 970 kW/m² | 330 - 930 kW/m² |
| Power transferred to main fluid: | 14.0 – 32.5 kW | 11.0 – 32.0 kW |
| Inner wall tube temperature: $T_{t,i}$ | 48 – 90 °C | 317 – 633 °C |
| Reynolds number: | 43600 – 298300 | 13720 - 284000 |
| Prandtl number: | 3.9 – 8.7 | 3.7 – 10.0 |

Table 4-4: Overview of range of main measurement quantities and derived quantities

# 4.7 Uncertainty analysis

The combined standard measurement uncertainty is computed using the method of propagation of uncertainty using the definitions of JCGM 100:2008 [116]. For this purpose, the partial derivative of each measured quantity is computed and the overall uncertainty is calculated based on the following general definition: $\sigma_{Nu_{\mathrm{m}}=f(x_1,x_2\ldots x_{\mathrm{n}})} \equiv \sqrt{\left(\frac{\partial y}{\partial x_1}\right)^2 \cdot \sigma_{x_1}^2 + \cdots + \left(\frac{\partial y}{\partial x_n}\right)^2 \cdot \sigma_{x_{\mathrm{n}}}^2}$. A coverage factor of k=1 is assumed for all values cited in this work, unless otherwise specified. The assumptions taken for the uncertainty analysis can be found in the appendix chapter F. As described in chapter 4.3, the power transferred to the main fluid can be deduced based on the measurement of the mass flow and temperature gradient in the main fluid – called the calorimetric method or by building the energy balance over the measurements of the induction heating power and the power transferred to the cooling water – called the electrical method. The equations (4.23) and (4.24) show the dependency of the uncertainty of the mean Nusselt number deduced from the calorimetric energy balance and the electrical energy balance respectively.

$$\sigma_{Nu_{\mathrm{m}}}^{\mathrm{cal}} = f(\dot{m}_{\mathrm{s}}; c_{\mathrm{p,s}}; \Delta T_{\mathrm{s}};\ T_{\mathrm{t,o}}; T_{\mathrm{s,in}}; \dot{Q}_{\mathrm{ins}}; \lambda_{\mathrm{t}}; \lambda_{\mathrm{s}}; r_{\mathrm{o}}; t_{\mathrm{t}}; l_{\mathrm{heat}}) \tag{4.23}$$

$$\sigma_{Nu_{\mathrm{m}}}^{\mathrm{el}} = f(I_{\mathrm{RMS}}; U_{\mathrm{RMS}}; \varphi; \dot{m}_{\mathrm{CW}}; c_{\mathrm{p,CW}}; \Delta T_{\mathrm{CW}}; \Delta T_{\mathrm{s}}; T_{\mathrm{t,o}}; T_{\mathrm{s,in}}; \dot{Q}_{\mathrm{ins}}; \lambda_{\mathrm{t}}; \lambda_{\mathrm{s}}; r_{\mathrm{o}}; t_{\mathrm{t}}; l_{\mathrm{heat}}) \tag{4.24}$$

The mean Nusselt number uncertainty for the calorimetric method is relatively high for high Reynolds numbers because of the low temperature gradient $\Delta T_{\mathrm{s}}$, while the impact of the uncertainty of this gradient on the mean Nusselt number deduced with the electrical method is very low (<0.1%). For this reason, the uncertainty of the Nusselt numbers deduced with the electrical method is generally lower. Therefore, mainly the results yielded with the electrical method are presented in chapter 5 . The values from the calorimetric method are used for plausibility checks. The content of the following subsection is adapted from an article published in advance of this dissertation: [22].

## 4.7.1 Results Uncertainty Analysis of the Water Setup

In the water tests, the relative mean Nusselt number uncertainty ranges between ±6% and ±31% for the calorimetric method and between ±7% and ±16% for the electrical method. A summary of the combined uncertainty for each measurand is found in Table 4-5.

The uncertainty for the calorimetric method is dominated by the uncertainty of the main flow temperature gradient $\sigma_{\Delta T_s}$, this makes up for 33% to 83% of $\sigma_{Nu_m}^{cal}$. The very high fractions are reached for the tests with the highest Reynolds numbers, because of the resulting low temperature gradients in the water. The uncertainty of the thermal conductivity of the tube $\sigma_{\lambda_t}$ represents the second largest contributor to the overall uncertainty with 8% to 20%. Other contributors to the uncertainty are the tube thickness $t_t$ (5% - 13%), the thermal conductivity of the salt $\lambda_s$ (1% - 11%), the tube outer wall temperature $T_{t,o}$ (1% - 10%), the heating length $l_{heat}$ (2% - 12%), and the tube outer radius $r_o$ (1% - 3%). All other parameters ($\dot{m}_s, c_{p,s}, T_{s,in}, \dot{Q}_{ins}$) make up for less than

1% of the Nusselt number uncertainty. Figure 4-12 shows the distribution of uncertainty contributions for an exemplary measurement point[IV].

The uncertainty for the electrical method is dominated by the power measurement $P_{t,el}^{el}$, which makes up for 31% to 48% of $\sigma_{Nu_m}^{el}$. The power measurement uncertainty is strongly dominated by the conservatively chosen uncertainty of the phase angle (see chapter F.3) which accounts for roughly 72% of $\sigma_{P_{t,el}^{el}}$. Then follow the RMS current uncertainty, which accounts for about 26%, and the RMS voltage uncertainty, which covers about 1%. All other contributors to $\sigma_{P_{t,el}^{el}}$, such as the cooling water massflow, heat capacity and temperature gradient as well as $\dot{Q}_{ins}$ amount to a contribution of less than 1%. As for the calorimetric method, the uncertainty of the thermal conductivity of the tube $\sigma_{\lambda_t}$ represents the second largest contributor to the overall uncertainty of $\sigma_{Nu_m}^{el}$ with 14% up to 31%. The tube thickness $t_t$ amounts for 9% to 20%, the thermal conductivity of the salt $\lambda_s$ for 2% to 9%, the tube outer wall temperature $T_{t,o}$ for 3% to 11%, the heating length $l_{heat}$ for 6% to 10% and the tube outer radius $r_o$ for 2% to 4%. All other parameters ($\Delta T_s$, $T_{s,in}$, $\dot{Q}_{ins}$) contribute less than 1% to the Nusselt number uncertainty $\sigma_{Nu_m}^{el}$. Figure 4-13 shows the distribution of uncertainty contributions to $\sigma_{Nu_m}^{el}$ for the same measurement point as in Figure 4-12.

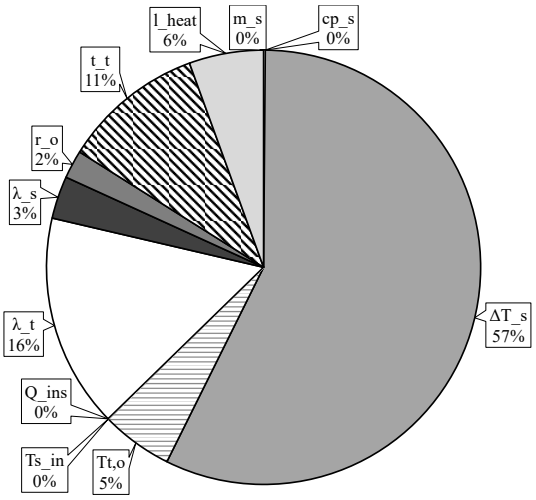


Figure 4-12: Exemplary distribution of uncertainty contributions of $\sigma_{Nu_m^{cal}}$ for water test (calorimetric method, test case WAT_m2_q700 [IV])

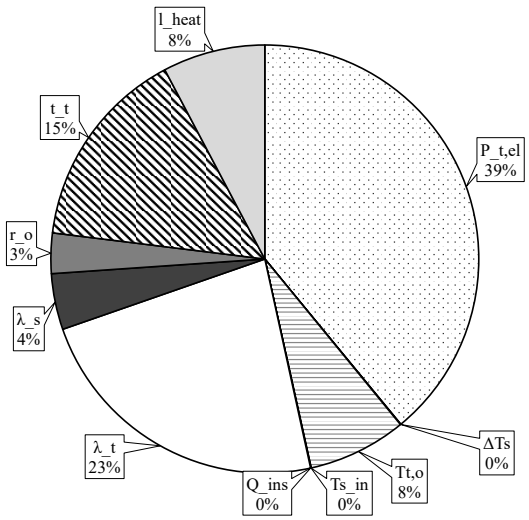


Figure 4-13: Exemplary distribution of uncertainty contributions of $\sigma_{Nu_m^{el}}$ for water test (electrical method, test case WAT_m2_q700 [IV])

From this analysis, it becomes obvious that the electrical method is better suited for measurements at high Reynolds numbers because the achieved temperature difference in the main flow $\Delta T_s$ has a negligible impact on the overall uncertainty. This is of special importance for the water setup,

[IV] Test identification: WAT_m2_q700, for more details see appendix D.3

because at Reynolds numbers comparable to the maximum Reynolds number of Solar Salt at 560 °C only a third to roughly half of the temperature gradient which can be achieved with Solar Salt is expected for the tests with water. This is because Solar Salt possesses roughly double the density, a quarter of the specific heat capacity and half the kinematic viscosity compared to water.

| Item | Range | Uncertainty |
|---|---|---|
| Main fluid mass flow: $\dot{m}_{\mathrm{s}}$ | 0.944 – 3.184 kg/s | ±0.2% |
| Cooling water mass flow: $\dot{m}_{\mathrm{cw}}$ | 0.157 – 0.160 kg/s | ±0.06% |
| Main fluid inlet temperature: $T_{\mathrm{s,i}}$ | 10 – 46 °C | ±0.1 K |
| Main fluid temperature difference $\Delta T_{\mathrm{s}}$ | 1 – 7 K | ±0.1 – 0.2 K |
| Outer wall temperature $T_{\mathrm{t,o}}$ | 80 – 150 °C | ±1 – 3 K |
| Cooling water temperature difference: $\Delta T_{\mathrm{cw}}$ | 7 – 16 K | ±0.1 K |
| RMS voltage $U_{\mathrm{RMS}}$ | 290 – 445 V | ±0.2% |
| RMS current $I_{\mathrm{RMS}}$ | 547 – 830 A | ±1% |
| Phase angle: $\varphi$ | 83.3° | ±0.12° |
| Combined measurement uncertainty $Nu_{\mathrm{m}}$ | | Calorimetric method: ±6% .. ±31%<br>Electrical method: ±7% and ±16 |

Table 4-5: Summary of combined measurement uncertainty of the water setup

### 4.7.2 Results Uncertainty Analysis of the Solar Salt Setup

In the Solar Salt tests, the relative mean Nusselt number uncertainty ranges between ±7% and ±41% for the calorimetric method and between ±6% and ±13% for the electrical method. A summary of the combined uncertainty for each measurand is found in Table 4-5.

The uncertainty for the calorimetric method $\sigma_{Nu_m}^{cal}$ is dominated by the power measurement $P_{t,el}^{cal}$ (68% to 99%). The power measurement itself is composed of the uncertainty of mass flow $\sigma_{\dot{m}_s}$, the temperature gradient $\sigma_{\Delta T_s}$ and specific heat capacity $\sigma_{\mathrm{c_{p,s}}}$. The mass flow measurement uncertainty strongly depends on the achieved height difference in the salt tank (see appendix F.2). The impact of the temperature gradient uncertainty is a function of the achieved temperature gradient in the salt $\Delta T_s$. When both are combined, the mass flow uncertainty and temperature gradient uncertainty make up for 54% to 98% of the power measurement uncertainty. The rest of the power measurement uncertainty is caused by the uncertainty of the specific heat capacity. The remaining contributors to the combined Nusselt number uncertainty $\sigma_{Nu_m}^{cal}$ are the thermal conductivity of the tube $\sigma_{\lambda_t}$ (<1% to 6%) the tube thickness $t_t$ (<1% to 4%) the thermal conductivity of the salt $\lambda_s$ (<1% to 9%), the tube outer wall temperature $T_{t,o}$ (<1% to 15%), the heating length $l_{heat}$ (<1% to 14%) and the thermal losses through the insulation $\dot{Q}_{ins}$ (<1 to 3%).

All other parameters ($r_o, T_{s,in}$) account for less than 1% of the Nusselt number uncertainty. Figure 4-14 shows the distribution of uncertainty contributions for an exemplary measurement point[V].

The uncertainty for the electrical method is as well dominated by the power measurement $P_{t,el}^{el}$, which makes up for 53% to 70% of $\sigma_{Nu_m}^{el}$. Similar to the water setup, the power measurement uncertainty is strongly dominated by the uncertainty of the phase angle (see chapter F.3) which accounts for roughly 80% to 90% of $\sigma_{P_{t,el}^{el}}$, followed by the RMS current uncertainty, which accounts for about 9% to 14% and the RMS voltage uncertainty, which covers about 1%. All other contributors to $\sigma_{P_{t,el}^{el}}$, such as the cooling water mass flow, heat capacity and temperature gradient as well as $\dot{Q}_{ins}$ amount to a contribution of less than 1%. The remaining contributors to the combined Nusselt number uncertainty $\sigma_{Nu_m}^{el}$ are the thermal conductivity of the tube $\sigma_{\lambda_t}$ (<1% to 13%) the tube thickness $t_t$ (<1% to 9%) the thermal conductivity of the salt $\lambda_s$ (<4% to 14%), the tube outer wall temperature $T_{t,o}$ (1% to 11%), the heating length $l_{heat}$ (12%) and the thermal losses through the insulation $\dot{Q}_{ins}$ (<1 to 3%). All other parameters ($\Delta T_s$, $T_{s,in}$, $\dot{Q}_{ins}$) make up for less than 1% of the Nusselt number uncertainty $\sigma_{Nu_m}^{el}$. Figure 4-15 shows the distribution of uncertainty contributions to $\sigma_{Nu_m}^{el}$ for the same measurement point as in Figure 4-14.

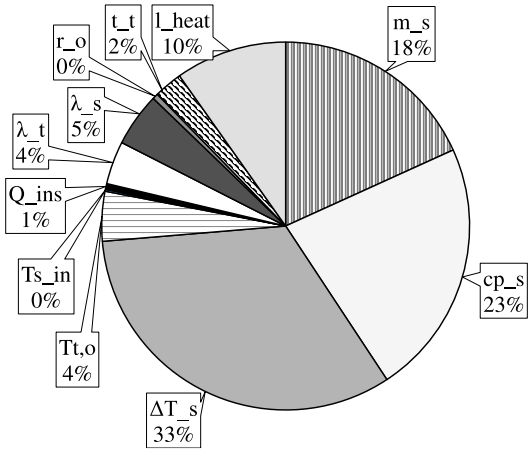


Figure 4-14: Exemplary distribution of uncertainty contributions of $\sigma_{Nu_m^{cal}}$ for salt test [V] (calorimetric method, test case SALT_SG_T300_m3_q700)

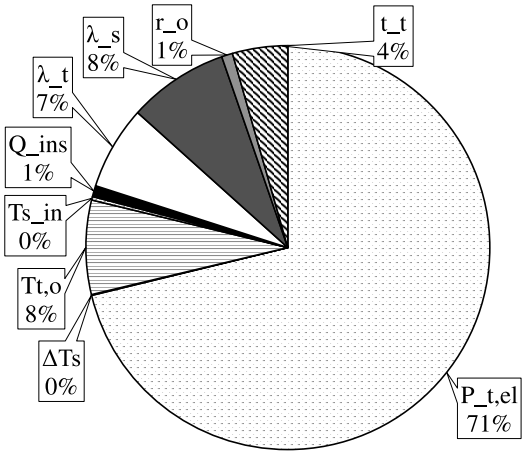


Figure 4-15: Exemplary distribution of uncertainty contributions of $\sigma_{Nu_m^{el}}$ for water test [V] (electrical method, test case SALT_SG_T300_m3_q700)

[V] Test identification: SALT_SG_T300_m3_q700, for more details see appendix chapter D.2

| **Item** | **Range** | **Uncertainty** |
|---|---|---|
| Main fluid mass flow: $\dot{m}_s$ | 0.56 – 5.81 kg/s | ± 2% – 15% |
| Cooling water mass flow: $\dot{m}_{cw}$ | 0.172 – 0.174 kg/s | ± 0.06% |
| Main fluid inlet temperature: $T_{s,i}$ | 296 – 554 °C | ± 0.2 °C |
| Main fluid temperature gradient $\Delta T_s$ | 1 – 30 K | ± 0.2 – 0.5 K |
| Outer wall temperature $T_{t,o}$ | 333 – 667 °C | ± 1 – 9 K |
| Cooling water temperature gradient: $\Delta T_{cw}$ | 5 – 15 K | ± 0.1 K |
| RMS voltage $U_{RMS}$ | 252 – 461 V | ± 0.2% |
| RMS current $I_{RMS}$ | 465 – 841 A | ± 1% |
| Phase angle: $\varphi$ | 83.6° | ± 0.2° |

Table 4-6: Summary of combined measurement uncertainty of the Solar Salt setup

# 5 Results and Discussion

In this chapter first the results of the validation campaign with the smooth tube and water are presented. In a next section, the results of the Nusselt number measurement campaigns with Solar Salt and a smooth tube are shown and discussed. In a final section, the results of both the Nusselt number and the friction factor of the spirally grooved tube measurement campaign with Solar Salt are presented and discussed.

## 5.1 Validation experiments with water

Measurements with water as the main fluid are used to validate the measurement setup for the forced convective heat transfer of Solar Salt in a smooth tube. As the heat transfer properties of water in smooth tubes is fairly well understood and water properties are well-known, water is well-suited for validation. The content of this subsection is adapted from an article published in advance of this dissertation: [22].

The water measurements are carried out for Reynolds numbers ranging between Re = 43000 and 305000, bulk Prandtl numbers between 4 and 9 and for five different flux densities[VI]: 420 kW/m², 560 kW/m², 660 kW/m², 830 kW/m² and 970 kW/m². Figure 5-1 shows the results of the mean measured Nusselt number normalized by the bulk and inner wall Prandtl number. As expected it can be seen, that the normalized Nusselt number increases with higher Reynolds numbers.

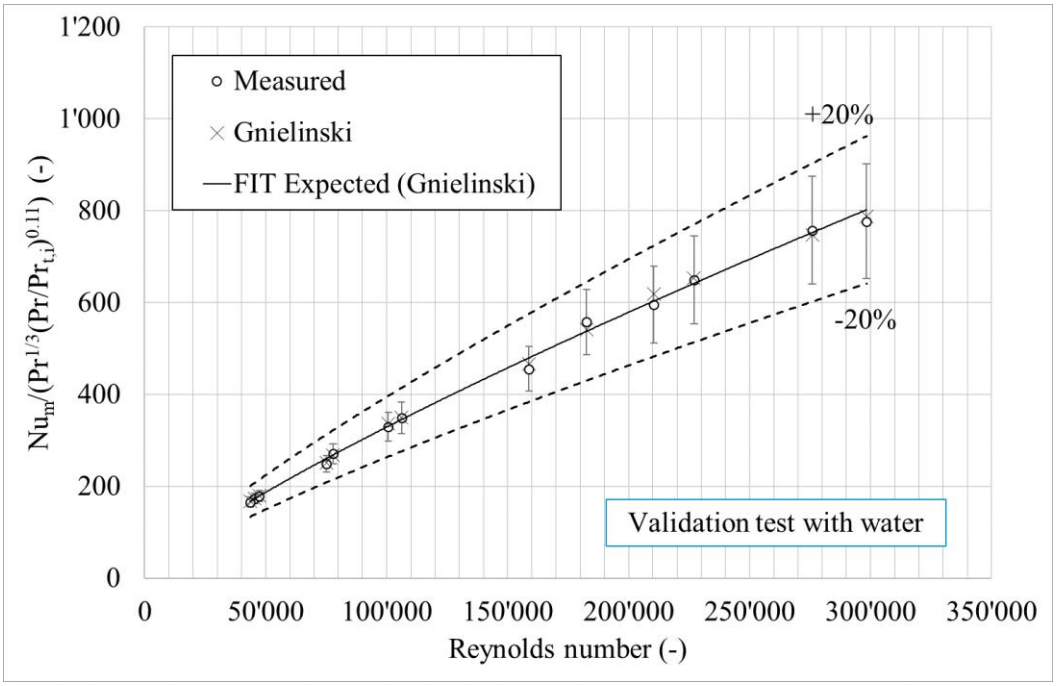


Figure 5-1: Normalized Nusselt number as a function of Reynolds number of the validation tests with water compared to the Gnielinski correlation (Re: 43000 to 305000, Pr: 4 to 9) [22]

[VI] Flux density is here defined at the inner tube surface as: $\dot{q} = (P_t - \dot{q}_{ins} \cdot 2\pi r_i \cdot l_{heat})/(2\pi \cdot r_i \cdot l_{heat})$

Figure 5-2 shows the results of the validation tests with water in comparison to the values predicted by the Gnielinski correlation. It can be observed that the measured values are in good agreement with the values predicted by the Gnielinski correlation with deviations lower than ±4%. Given the high uncertainties, especially at the high Reynolds numbers, this can be interpreted that the chosen uncertainties, especially for the phase angle $\varphi$ and the tube wall thickness $t_t$ are on the conservative side.

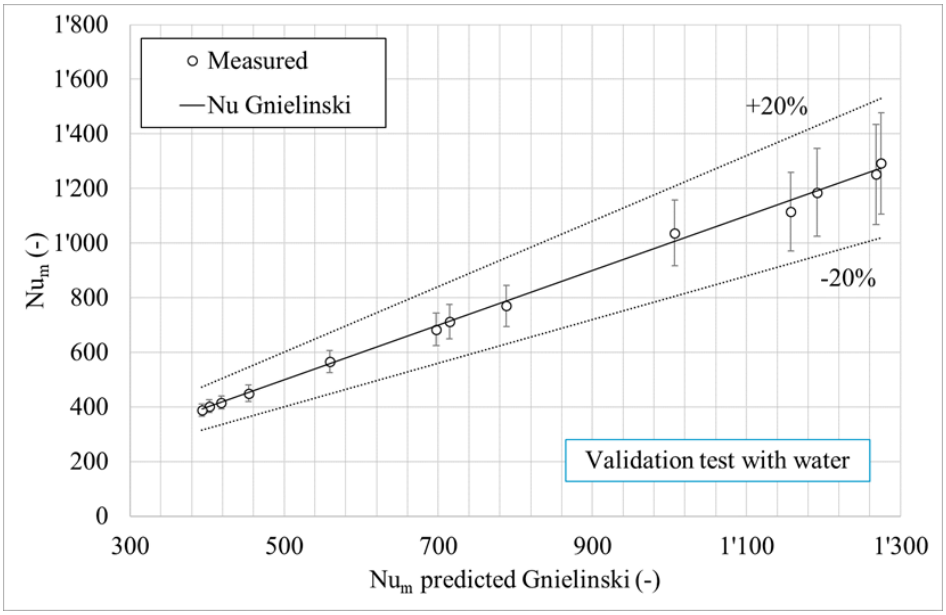


Figure 5-2: Measured Nusselt number compared to the Nusselt number predicted by the Gnielinski correlation of the validation tests with water (Re: 43000 to 305000, Pr: 4 to 9) [22]

## 5.2 Smooth circular tube with Solar Salt

The forced convective heat transfer of Solar Salt in a smooth tube is determined at three main bulk salt inlet temperatures: 300°C, 400°C and 550°C. Consequently, Prandtl numbers range from 10 to 3.8. At each temperature, up to 5 different mass flows are assessed. This approach leads to Reynolds numbers ranging between 14000 and 222000. Three different flux densities are applied for each combination of mass flow and temperature: 330 kW/m², 630 kW/m² and 930 kW/m². The content of this subsection is adapted from an article published in advance of this dissertation: [22].

Figure 5-3 shows the resulting absolute measured mean Nusselt number of Solar Salt as a function of Reynolds number for all salt temperatures. As expected, the Nusselt number increases with increasing Reynolds number and decreases with lower Prandtl numbers. The mean Nusselt numbers range from 130 up to 1300. The values predicted by the Gnielinski correlation for a mean bulk Prandtl number and mean film Prandtl number of all experiments are added for reference.

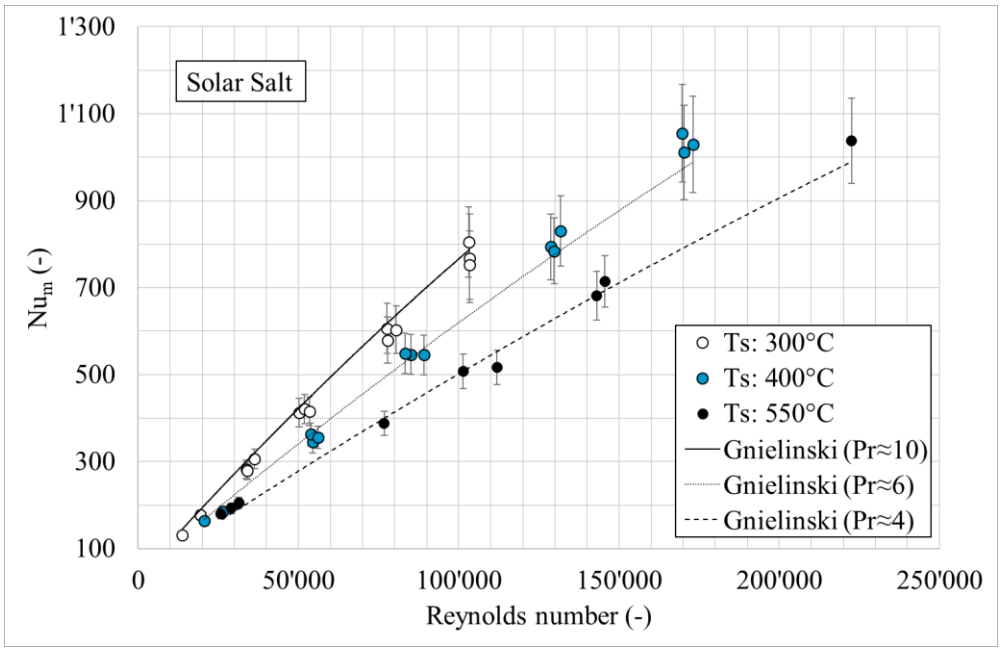


Figure 5-3: Measured mean Nusselt number of Solar Salt as a function of Reynolds number and salt temperature (Re: 14000 to 222000; Pr: 3.8 to 10) and values expected by Gnielinski for 3 different Prandtl numbers [22]

Figure 5-4 shows the comparison of the heat balance between the results obtained with the "calorimetric method" compared to the "electrical method" as a function of Re. For 65% of the experimental cases, the deviation of both approaches is less than ±2.5%, for 90% of the experiments, the deviation is less than ±5%.

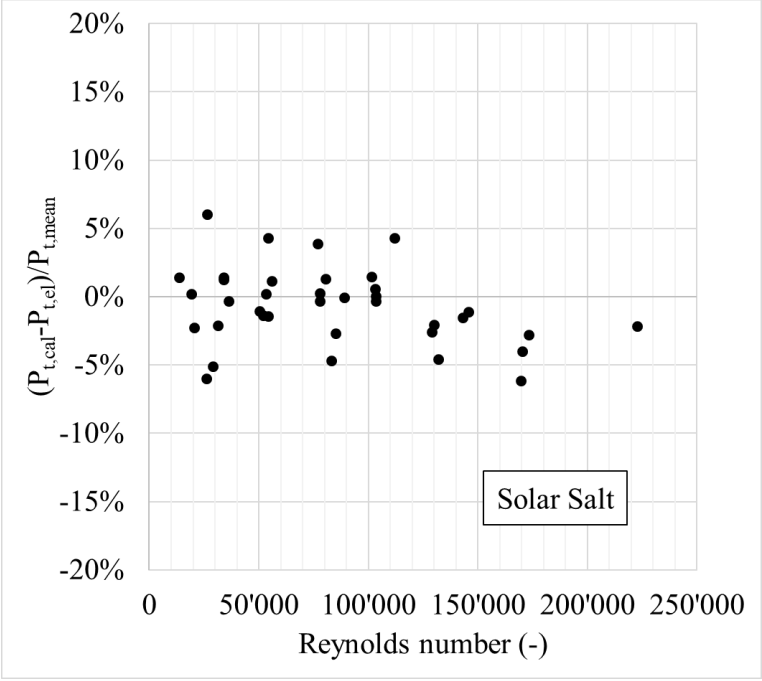


Figure 5-4: Deviation of power transferred to tube using the calorimetric and the electrical method as a function of Re (Re: 14000 to 222000; Pr: 3.8 to 10) [22]

Figure 5-5 shows the measured Nusselt number of all salt temperatures normalized by the bulk and inner wall Prandtl number. The measured deviations from the Gnielinski correlation fit within the uncertainty of the measurement and the uncertainty band of ±20% stated by the Gnielinski correlation.

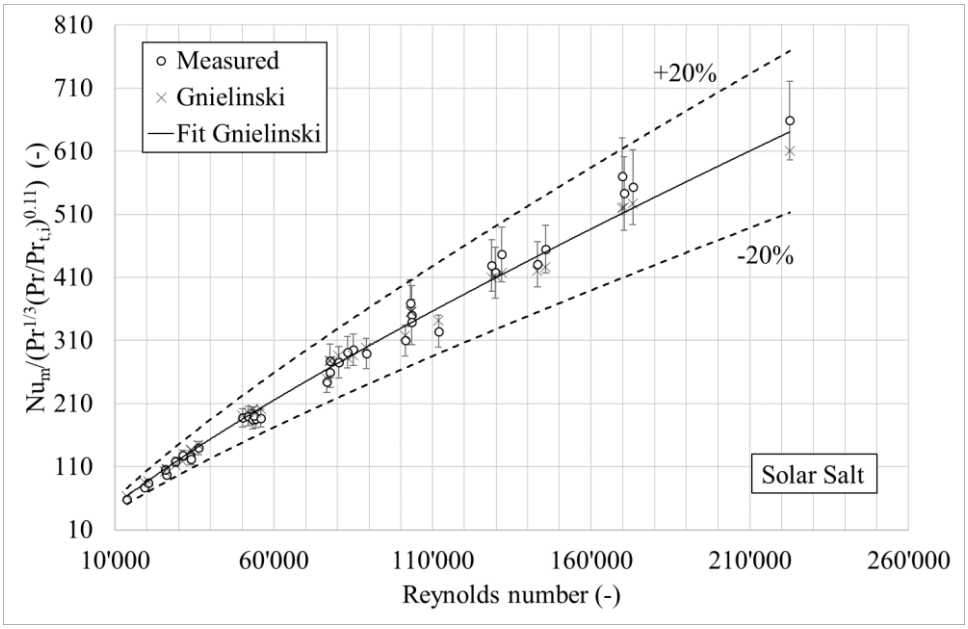


Figure 5-5: Normalized mean Nusselt number of Solar Salt as a function of Re number for all salt temperatures (Re: 14000…222000; Pr: 3.8…10)

This becomes even more obvious in Figure 5-6 in which the measured mean Nusselt number is plotted versus the expected mean Nusselt number using the Gnielinski correlation. In this plot, small variations in Prandtl number and varying heat flux can be accounted for. The observed values for the salt properties impact factor $\left(Pr/Pr_{t,i}\right)^{0.11}$ range between 1.01 and 1.08 for the conditions in the present experiment. This is generally lower than the measurement uncertainty. No impact beyond the values predicted by this factor is observed for the measured mean Nusselt numbers for this measurement campaign. To enable the reader to reproduce the resulting measurements of a smooth tube, a correlation following the scheme proposed by Sieder and Tate [21] is fitted to the measurement data using the least square method. The resulting fitted correlation for Solar Salt (Re: 14000…222000; Pr: 3.8…10) is:

$$Nu_{m,FIT} = 0.0094 \cdot Re^{0.9} \cdot Pr^{0.4} \cdot \left(\eta/\eta_{t,i}\right)^{0.14} \tag{5.1}$$

This fit predicts 78% of the measured points within ±7% and 95% of the measured points within ±10%.

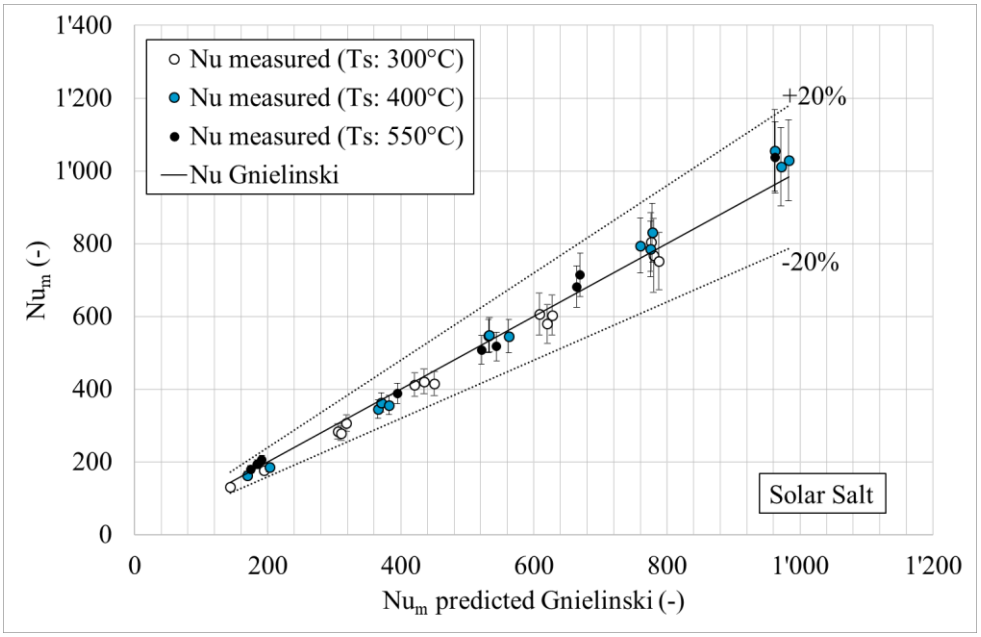


Figure 5-6: Mean measured Nusselt number of Solar Salt over mean expected Nusselt number (Gnielinski) for different salt temperatures (Re: 14000 to 222000; Pr: 3.8 to 10) [22]

One concern in the operation of solar receivers is the impact of local salt degradation due to local overheating of the tube as it was observed by Jiangfeng et al. with HITEC [57]. They observed a rapid decrease of the convective heat transfer as the tube inner wall temperatures approached the maximum operation temperature specified by the manufacturer. Such a rapid decrease would lead to further overheating of the tube and cause stronger decrease of the heat transfer. This is especially critical if the flux reaching the absorber tube cannot be controlled very accurately. Figure 5-7 shows the mean measured Nusselt number as a function of expected Nusselt number for bulk salt temperatures around 550 °C. The highest inner wall temperatures are expected at low Reynolds numbers. The maximum film temperature was around 630 °C. No relevant trend of deviation of the measured Nusselt number from the expected values is observed.

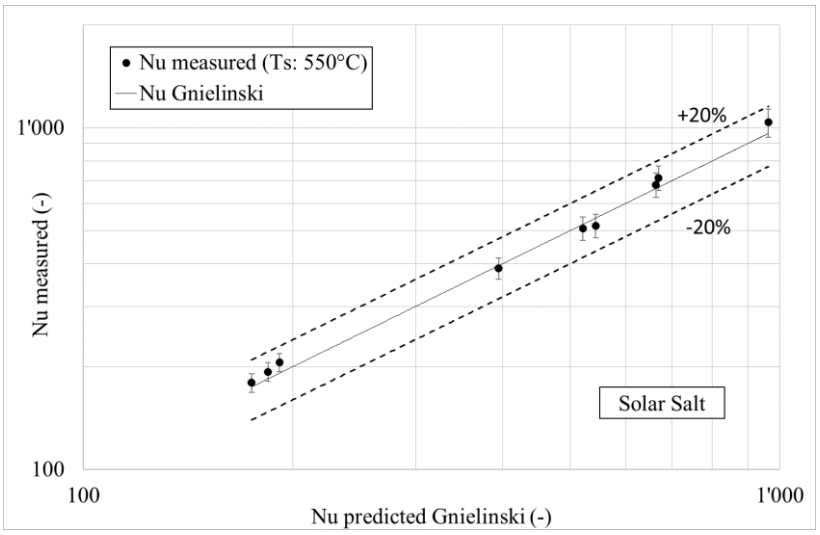


Figure 5-7: Mean measured Nusselt number as a function of predicted Nusselt number for bulk salt temperatures at 550°C (Re: 25000 to 220000, Pr≈4) [22]

Figure 5-8 shows the deviation of the mean measured Nusselt number from the expected one calculated by Gnielinski of all measurement points. For 76% of the measurements, the deviation lies within ±7% and 97% of the measurement lying within ±10% deviation, with no apparent trend of film temperature. Based on these results, this thesis recommends the usage of the Gnielinski correlation (Table 2-1) for the prediction of the mean Nusselt number of Solar Salt in smooth circular tubes for Reynolds numbers ranging between 14000 and 222000, Prandtl numbers ranging between 3.8 and 10 and flux densities ranging between 330 and 930 kW/m².

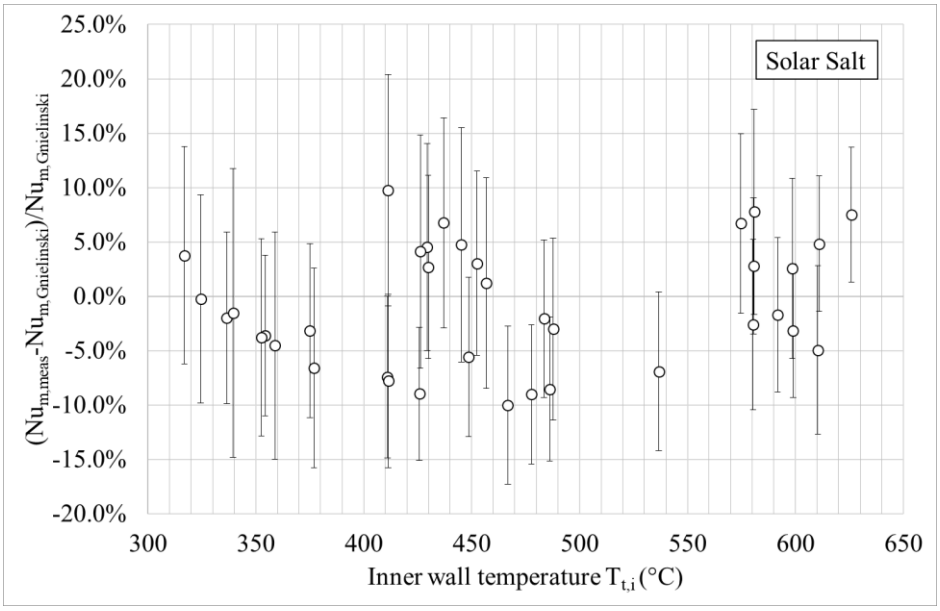


Figure 5-8: Deviation of measured mean Nu number from expected mean Nusselt number calculated by Gnielinski as a function of the inner wall temperature (Re: 14000 to 222000; Pr: 3.8 to 10) [22]

This result is in contradiction to the findings published by Das et al. [58]. This might be caused

by the different setup, as they analyzed annular flow rather than the flow in a tube. However, as the employed Reynolds number range, salt bulk temperature and flux density range are not available, it is currently not possible to identify the cause for this deviation. In this experiment, the inner wall temperature up to 630 °C does not lead to a decrease in heat transfer at the present short dwell times of the salt in the heating section (~ < 1 s). Nevertheless, it cannot be excluded that salt degradation which would lead to a decrease in heat transfer might occur at longer dwell times for Solar Salt. The dwell times in the present experiment are similar to those of Jiangfeng et al. (1-3 s) [57], who did observe a strong decrease of heat transfer and attributed this effect to salt degradation. However, Jiangfeng et al. exceeded the specified upper temperature limit by a higher margin and used a different salt, which might behave differently. Also, it has not been reported by Jiangfeng et al. whether the lowering of heat transfer in their experiment persisted for lower wall temperatures, thus excluding the formation of a low conductance surface layer through corrosion. It must be noted that the high temperature experiments described in the present paper are carried out over a duration of seven days, which might be too short for the development of a corrosive layer. Long term operation at high film temperatures might lead to the formation of a low conductance surface layer and hence to a local decrease of thermal conductivity of the tube. Further research is necessary to gain deeper understanding of the effects at hand.

# 5.3 Spirally grooved tube with Solar Salt

## 5.3.1 Nusselt number

The forced convective heat transfer of Solar Salt in a spirally grooved tube with a relative groove height $e/d_i$=0.017, a relative groove pitch $p/d_i$=0.913 and groove angle α=73.8° is deduced for three main bulk salt inlet temperatures: 300°C, 400°C and 550°C. This leads to bulk Prandtl numbers ranging from 10 to 3.7. At each bulk salt temperature up to 5 different mass flows are assessed. This approach leads to Reynolds numbers ranging between 11000 and 285000. Three different flux densities are applied for each combination of mass flow and temperature: 330 kW/m², 630 kW/m² and 930 kW/m². This subsection is based on an article that was published prior to the completion of this dissertation: [59].

Figure 5-9 shows the resulting mean measured Nusselt number of the spirally grooved tube for the three investigated salt bulk temperatures. As generally observed for Nusselt numbers, the Nusselt number increases for higher Reynolds numbers and decreases for lower Prandtl numbers. A correlation of the form proposed by Sieder-Tate [21] is fitted to the obtained measurement data using a least square algorithm ($Nu_m = C_0 \cdot Re^{C_1} \cdot Pr^{C_3}(\mu/\mu_w)^{0.14}$). The resulting correlation is shown by equation (5.2).

$$Nu_{m,a} = 0.0129 \cdot Re^{0.88} \cdot Pr^{0.38}(\mu/\mu_w)^{0.14} \tag{5.2}$$

For orientation the fitted mean Nusselt number is shown in Figure 5-9 for three representative salt bulk and inner wall temperatures.

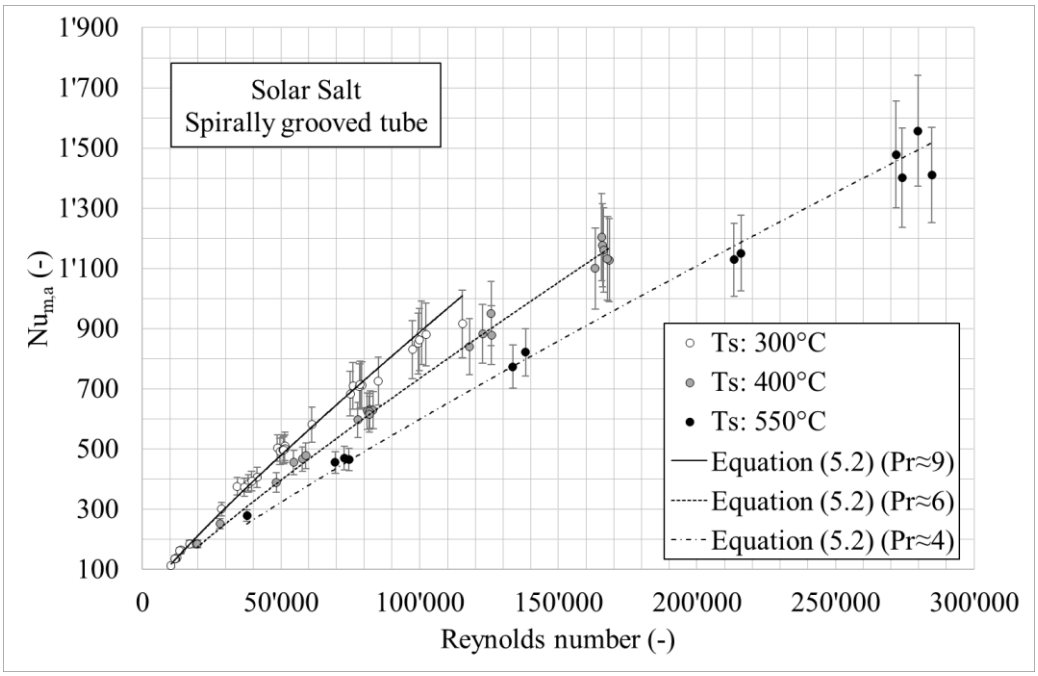


Figure 5-9: Mean Nusselt number of Solar Salt as a function of Reynolds number and salt temperature (Re: 11000 to 285000; Pr: 3.7 to 10) and values calculated with equation (5.2) assuming a constant Prandtl and inner wall temperature [59]

Figure 5-10 shows the comparison of the two heat balances as a function of Reynolds number. It can be observed that 68% of the experimental cases show a deviation of less than ±2.5% of the "calorimetric method" compared to the "electrical method". 96% of the experimental cases show a deviation less than ±5%. Hence good agreement is found between the two methods for measuring the power transferred to the tube.

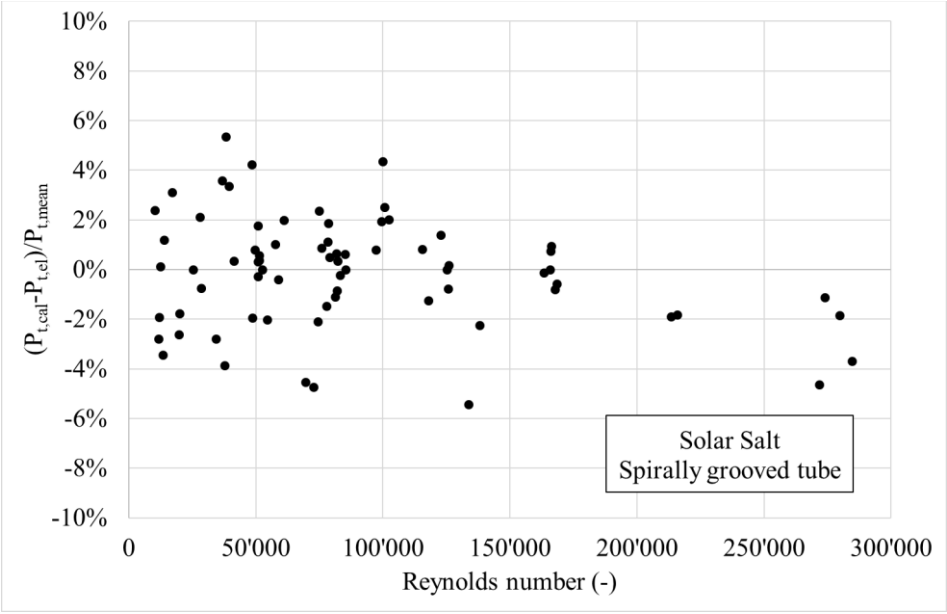


Figure 5-10: Deviation of power transferred to tube using the calorimetric and the electrical method as a function of Re (Re: 11000 to 285000; Pr: 3.7 to 10) [59]

Figure 5-11 shows the measured mean Nusselt number of the spirally grooved tube and the mean Nusselt number predicted by the Gnielinski correlation for the smooth tube as a function of the values predicted by the Gnielinski correlation. The measured Nusselt numbers of the spirally grooved tube at Reynolds number smaller than 25000 are only slightly higher or equal to the values predicted by Gnielinski for the smooth tube. For Reynolds numbers ranging between 27000 up to 285000 the measured Nusselt numbers of the enhanced tube are on average about 20% higher than those expected by the Gnielinski correlation for a smooth tube.

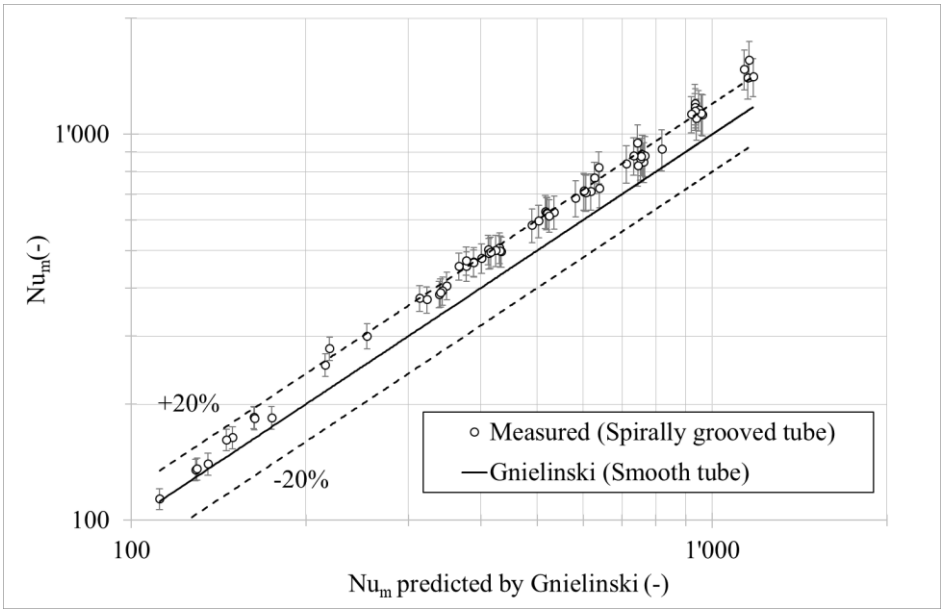


Figure 5-11: Measured mean Nusselt number of Solar Salt as a function of mean Nusselt number predicted by Gnielinski correlation (Re: 11000 to 285000; Pr: 3.7 to 10) [59]

In Figure 5-12 the measured mean Nusselt number for all three temperatures is shown as a function of the mean Nusselt number expected by equation (5.2). Figure 5-13, shows the resulting Nusselt number ratio $Nu_{a,0}$ for all three bulk salt temperatures as a function of Reynolds number. Both graphs show the good agreement between the fitted correlation and the measurement: the fitted correlation (5.2) fits 79% of the measured values within ±5% and 99% of the measured values within ±8%.

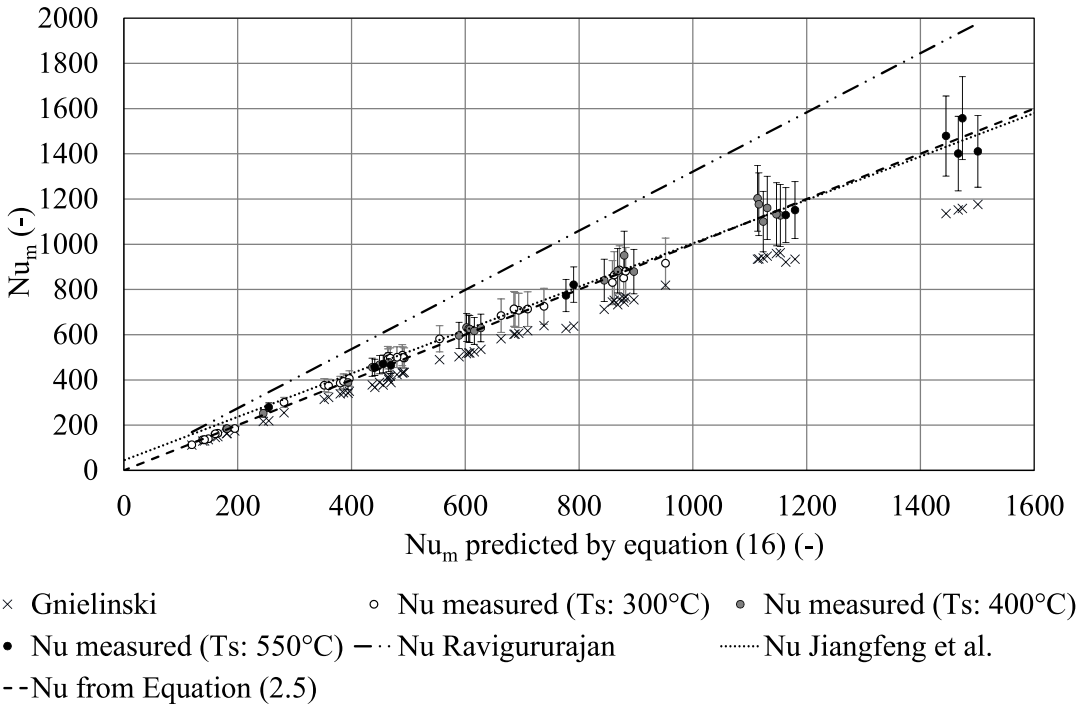


Figure 5-12: Measured mean Nusselt number and mean Nusselt number predicted by several correlations as a function of the Nusselt number predicted by equation (5.2) (Re: 11000…285000; Pr: 3.7…10) [59]

The same figures show the values predicted by the general correlation proposed by Ravigururajan et al. [7]. As also found by other authors, who performed measurements with molten nitrate salts in enhanced tubes, the Ravigururajan correlation seems to overpredict the measured Nusselt numbers by a factor of 1.2 up to 1.4. This is, however within the uncertainty range of ±20% up to ±50% specified by Ravigururajan. Also, as can be seen in Figure 5-13, the Ravigururajan correlation predicts a continuous increase of the Nusselt number ratio $Nu_{a,0}$ with the Re number. ($Nu_{a,0}$ increases 0.15 from Re=25000 to 285000). This can, given the present uncertainty of the high Reynolds number results, not be validated with the present measurements for Re>25000.

Finally, Figure 5-12 and Figure 5-13 show the values expected by the general correlation for enhanced tubes proposed by Jiangfeng et al. [57]. This correlation was validated for Re=10000 - 30000, which roughly corresponds to $Nu_m$=100 – 300, so the values outside this interval must be considered with care. It can be observed that the general correlation of Jiangfeng predicts 62% of the measured values within ±5% and 91% of the measured values within ±10%. The deviations to the Jiangfeng correlation are found for Re numbers below 25000. This is surprising, as the measurements of Jiangfeng were conducted with a spirally grooved tube which had a similar relative pitch angle for this Reynolds number range. However, Jiangfeng et al. used relative groove heights which were 30% larger and lower flux densities (~220 to 240 kW/m²). On the other hand, the relative groove width in the present experiment is 20% larger than the dimensions used by Jiangfeng and approaches values equal to one. Chen et al. [76] found that for a relative groove width equal to one, little to no increase of Nusselt number was observed. However, Chen's experiments were conducted for a transversally grooved tube. Also, it must be noted that both

Chen and Jiangfeng used a ternary nitrate salt, which has Prandtl numbers which are roughly double the Pr numbers of the present binary nitrate salt. Furthermore, it could be argued, that the effect might be caused by local overheating of the salt.

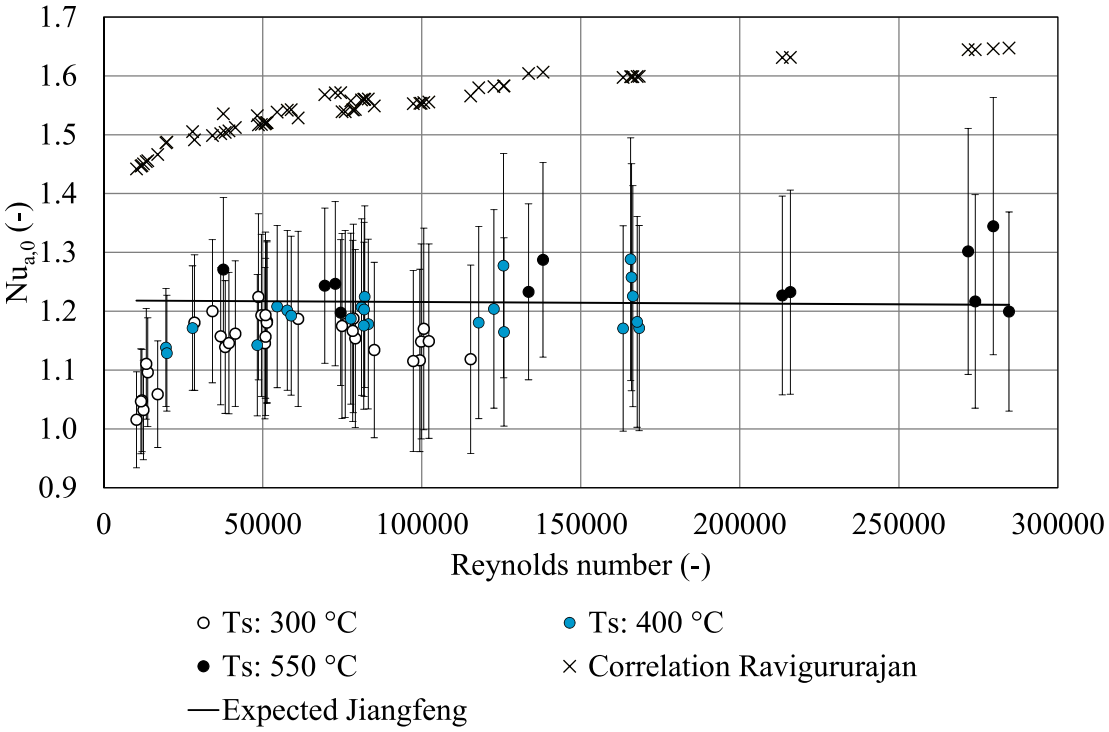


Figure 5-13: Measured and expected Nusselt number ratio $\frac{Nu_a}{Nu_0}$ of two different authors as a function of Reynolds number (Re: 11000 to 285000; Pr: 3.7 to 10) [59]

Local salt degradation due to local overheating of the tube is a concern during the operation of heat exchangers using molten salts. This effect was observed by Jiangfeng et al. with the ternary nitrate salt HITEC [57]: They measured a rapid decrease of the convective heat transfer as the tube inner wall temperatures approached the maximum operation temperature specified by the manufacturer. This rapid decrease leads to further overheating of the tube and probably would entail further decrease of the heat transfer. Figure 5-14 shows the deviation of the measured Nusselt number of the spirally grooved tube from the Nusselt number predicted by the Gnielinski correlation for a smooth tube. From this figure, no obvious trend of the variation of Nusselt number compared to Gnielinski can be deduced as a function of inner wall temperature for $T_{t,i}$=315 - 633°C. However, some outliers can be observed; these measurements are obtained at low Reynolds numbers, which show a considerable reduction of heat transfer compared to the measurements at higher Nusselt numbers, as already seen in the previous graphs.

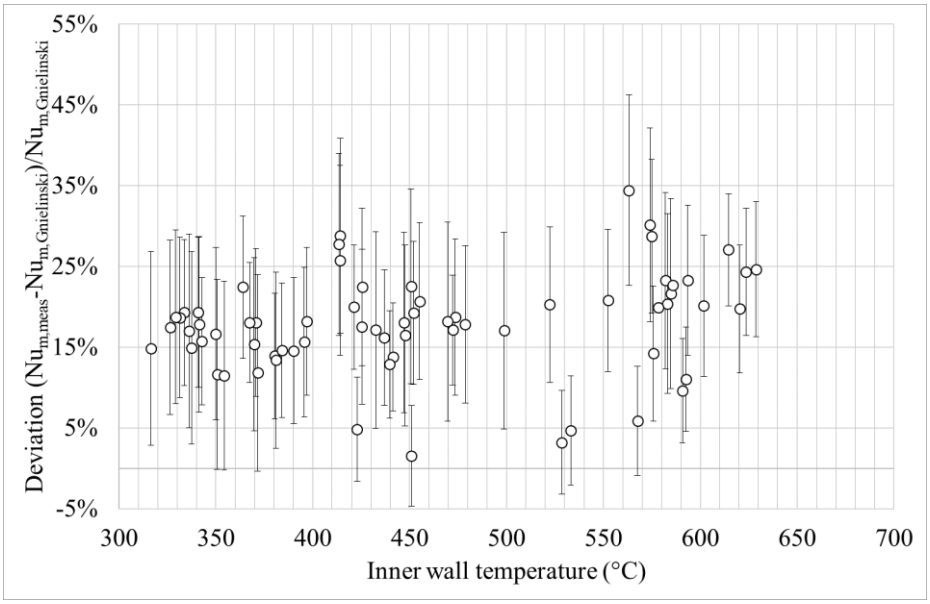


Figure 5-14: Deviation of measured mean Nu number (spirally grooved tube) from the Gnielinski mean Nusselt number (smooth tube) as a function of the inner wall temperature (Re: 11000…285000; Pr: 3.7…10)

Based on Figure 5-14 it can be concluded that inner wall temperatures up to 633 °C alone do not lead to a decrease in heat transfer in the present experiment. It must however be pointed out that the systematic decrease in heat transfer towards lower Reynolds numbers could be caused by local salt degradation. On the one hand, the salt has a higher dwell time in the tube at lower Reynolds numbers leaving more time for the gaseous products to form and disturbing the heat transfer. On the other hand, it could be, that beside the increase of local fluid velocity through the grooves, the grooves might also locally decrease the fluid velocity (for example shortly before and after the groove). This could cause local overheating beyond the measured inner wall temperatures and entail local salt degradation (see chapter 3.4). The formation of a low conductive film can be excluded, because the low Reynolds number experiments were repeated at the very beginning and at the end of the measurement campaign and yielded the same results. Further research is necessary to quantify the observed Nusselt number behavior for Re= 10000 to 25000 in the spirally grooved tube and derive its origin with certainty. Furthermore, the present experiments were only carried out over a duration of a few weeks. Therefore, it cannot be excluded that long-term operation at high film temperatures would lead to the formation of a low conductance surface layer and to a local decrease of thermal conductivity of the tube. Further research is required to yield data in long-term operation.

### 5.3.2 Friction factor

In order to evaluate the performance enhancement properties of the spirally grooved tube, the friction factor ratio needs to be assessed beside the Nusselt number ratio. For this purpose, the pressure difference over the test section is deduced on one hand for the spirally grooved tube and on the other hand for a smooth tube. Figure 5-15 shows the measured pressure difference of the setup with a smooth tube and the setup with a spirally grooved tube for three bulk salt

temperatures as a function of bulk flow velocity. It can be observed that the pressure difference increases – as expected – in a quadratic fashion with increasing flow velocity. Also, the pressure difference decreases for higher temperatures, which is mainly due to the lower salt density at higher temperatures. In addition, it can be observed that the pressure difference of the spirally grooved tube is generally higher than for the smooth tube. It must be noted that the pressure difference shows considerable scattering, For this reason, only the measurement data for pressure differences greater than 0.3 bar will be evaluated further on.

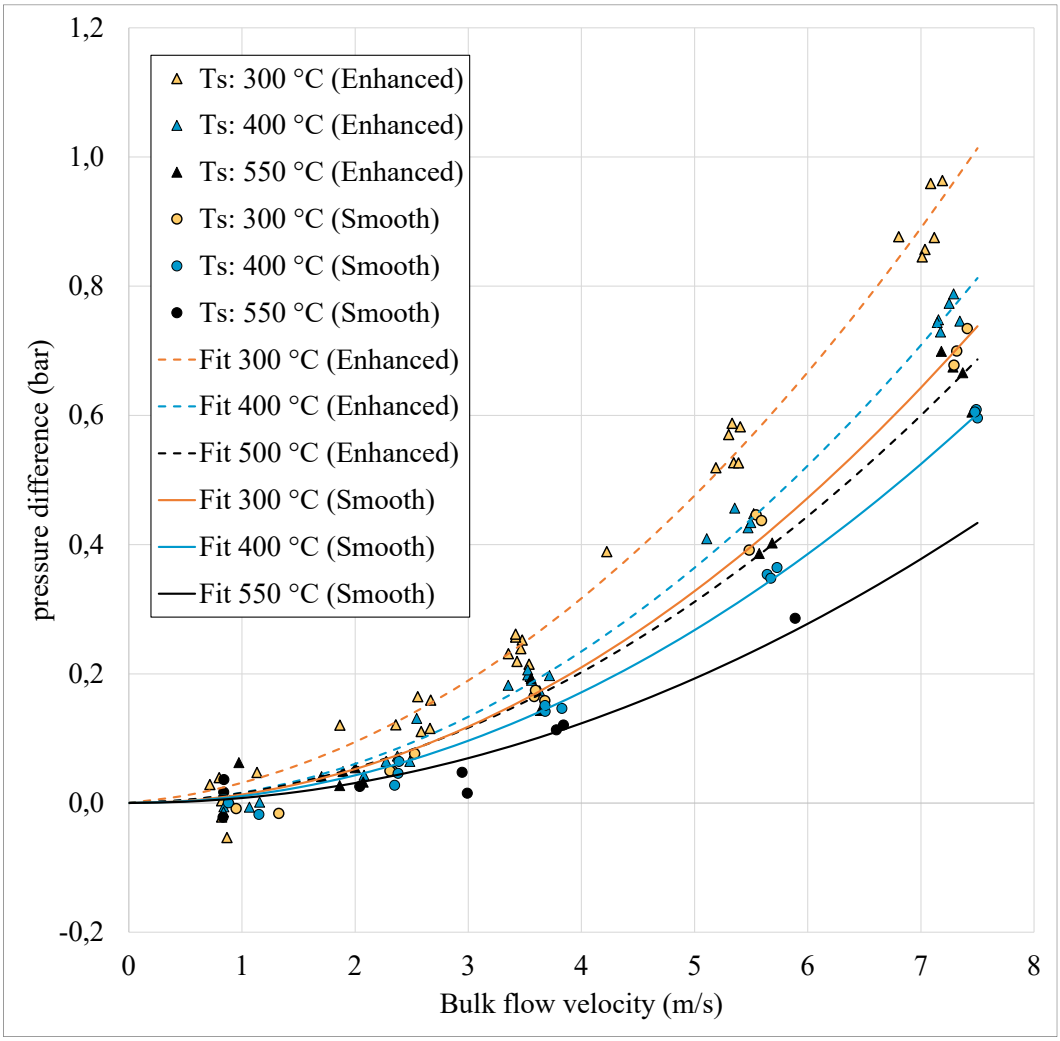


Figure 5-15: Pressure difference over test section as a function of salt temperature for a smooth and the spirally enhanced tube (Re: 11000 to 285000; Pr: 3.7 to 10) (adapted from [59])

Figure 5-16 shows the resulting friction factors deduced using equation (4.21). As expected, the friction factor decreases for higher Reynolds numbers and the friction factor of the spirally grooved tube is generally higher than that of the smooth tube. A power function is fitted to the measurement data following the basic form proposed by Blasius et al. for turbulent flow in a smooth tube [19] using a least square algorithm. Using these fitted functions, the friction factor ratio can be expressed using equation (5.3):

$$\zeta_a/\zeta_0 = \frac{0.7709 \cdot Re^{-0.3022}}{0.8843 \cdot Re^{-0.3415}} \tag{5.3}$$

It is interesting to point out that correlations which account for roughness of the tube (see Figure 2-5 and Prandtl [117]) lead to lower agreement with the measurement data as these correlations predict a lower temperature-dependency as shown by the measurement data. In this experiment, the pressure difference of both the smooth and the enhanced tube are best predicted with formulations of correlations typically used for smooth tubes following the form suggested by Blasius.

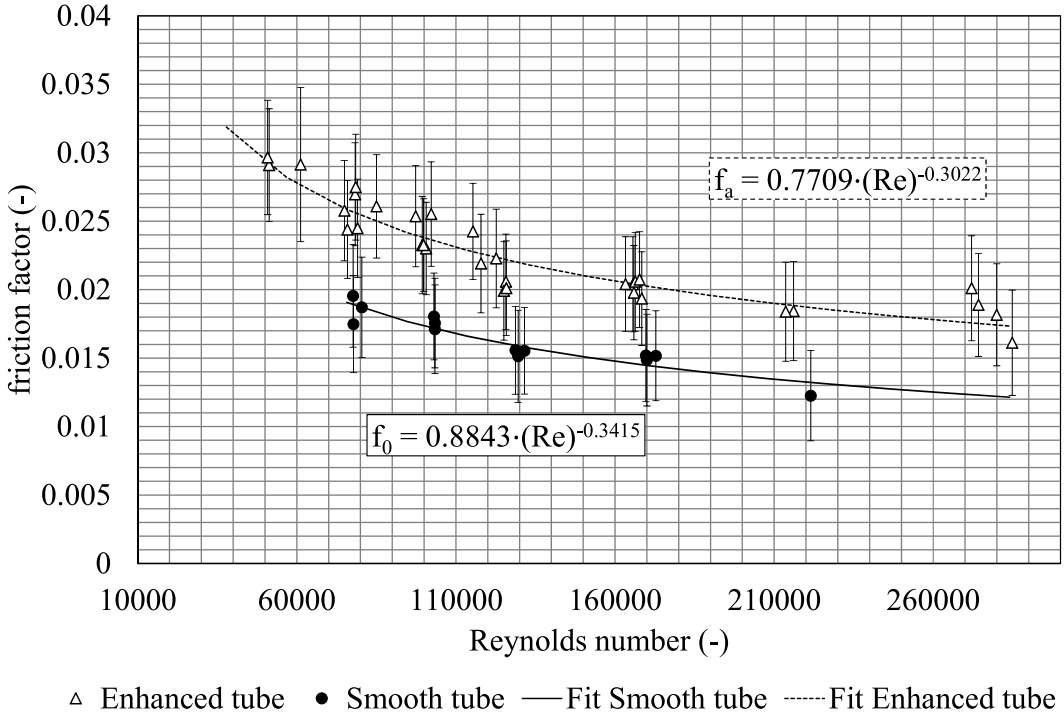


Figure 5-16: Friction factor of smooth and spirally grooved tube and respective fitted power functions as a function of Reynolds number [59]

Figure 5-17 shows the resulting friction factor ratio using equation (5.3) as well as the resulting friction factor when directly calculating the friction factor ratio using equation (4.22) from measurement data of the spirally grooved and smooth tube respectively. As not all measurements were taken at exactly the same salt temperature and Reynolds number, only the useful pairs are shown. It can be seen that the measurements achieved with equation (4.22) do generally agree with the friction factors obtained with equation (5.3) within the measurement uncertainty. Furthermore, Figure 5-17 shows the predicted friction factor ratio by the general equation by Ravigururajan et al. [7]. The general correlation overpredicts the measured friction factor ratio by a factor of 1.8 to 2.9. This result lies considerably outside the uncertainty band given by Ravigururajan et al. of ±50%. The tube investigated in the present study has a groove height more at the lower end of the spectrum investigated by Ravigururajan et al., this might cause the overestimation, as the general correlations were developed to fit a large geometry basis. At the same time, the measurement results of this thesis are in the same order of magnitude as the

deviations measured by Chen et al [54]. It must however be noted that the measurements conducted by Chen are performed using a ternary nitrate salt, with a transversally grooved tube. Further research is necessary to understand the origin of this deviation.

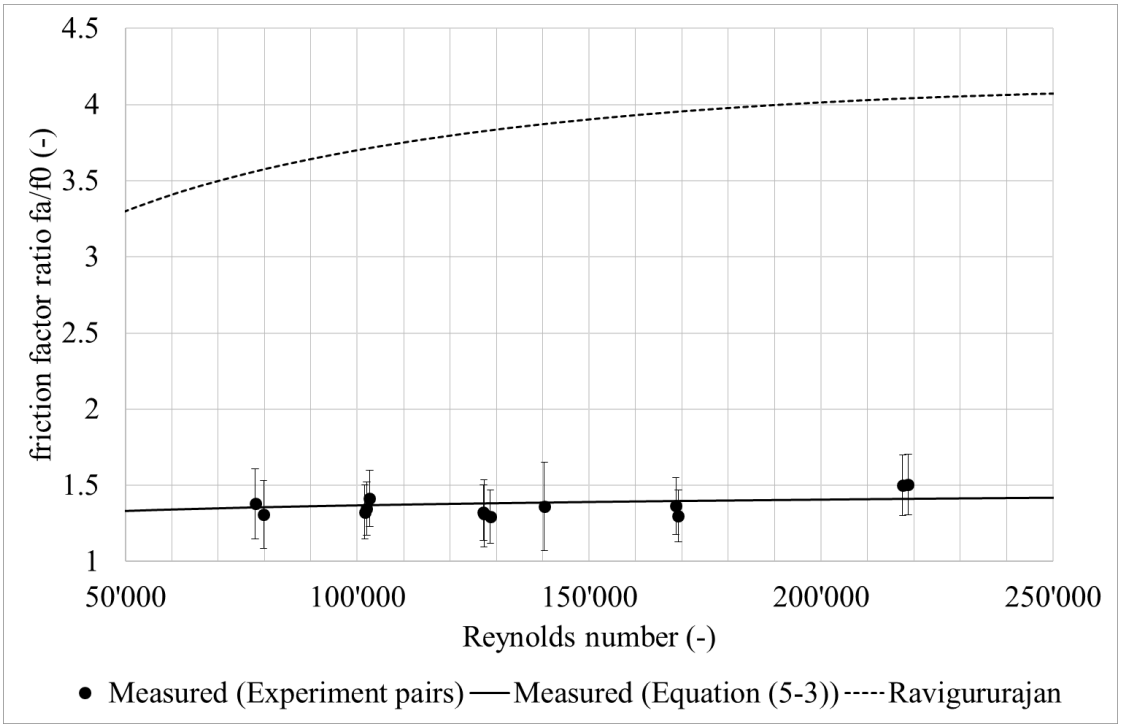


Figure 5-17: Friction factor ratio deduced by two approaches from the measurement data and by a general correlation as a function of Reynolds number [59]

# 6 Conclusion

This thesis evaluates the forced convective heat transfer of the molten nitrate salt "Solar Salt" (60 wt-% $NaNO_3$; 40 wt-% $KNO_3$) in a smooth circular tube and a spirally grooved tube at high Reynolds numbers at varying flux densities and bulk salt temperatures. In a first step, a thorough review on the available literature on forced convective heat transfer of molten salts in circular tubes is performed. In this literature review, it was found that little experimental data exists on the behavior of the Nusselt number at Reynolds numbers greater than 50000 and that the sources at hand concluded that common correlations overestimate the Nusselt number up to a factor of 3.5. Furthermore, the state-of-the-art of the thermophysical properties of Solar Salt is investigated. The review yields correlations for the specific heat capacity, density, dynamic viscosity, and thermal conductivity, including their respective uncertainties. Finally, an innovative experimental setup for evaluating the forced convective heat transfer of Solar Salt employing an induction heater is described. The experimental setup is validated through measurements with water as its forced convective heat transfer properties are well-known. The values measured in the setup with water showed good agreement with the values predicted by the Gnielinski correlation with deviations lower than ±4%.

The forced convective heat transfer with Solar Salt is measured for three main bulk salt inlet temperatures: 300 °C, 400 °C and 550 °C, leading to Prandtl numbers ranging from 10 to 3.8. At each temperature, up to 5 different mass flows are assessed. This approach leads to Reynolds numbers ranging between 14000 and 222000. Three different flux densities are applied for each combination of mass flow and temperature: 330 kW/m², 630 kW/m² and 930 kW/m². To enable reproduction of the measurement results, a correlation was fitted to the measurement data using the least squares method. Good agreement is found between the Nusselt numbers expected by the Gnielinski correlation and the measured mean Nusselt numbers with 76% of the measurements lying within ±7% deviation and 97% of the measurement lying within ±10% deviation. No obvious trend of the applied heat flux on the measured mean Nusselt number beyond the values predicted by Gnielinski is observed. Special focus is put on the impact of inner tube wall temperatures larger than 600 °C on the heat transfer. The measurements show that inner wall temperatures up to 630 °C do not lead to a decrease in convective heat transfer to the salt in the heating section for the dwell times present in this experiment. Hence, it is concluded that the Gnielinski correlation is well-suited for the prediction of Nusselt numbers of Solar Salt in smooth tubes at the conditions presented in this experiment. This result is in contradiction to the findings published by other authors. This might be caused by the different setup, as they analyzed annular flow rather than the flow in a tube. However, as the employed Reynolds number range, salt bulk temperature and flux density range are not given in the reference, it is currently not possible to identify the cause for this deviation.

Furthermore, the forced convective heat transfer and pressure difference of "Solar Salt" in a spirally grooved tube at high Reynolds numbers at varying flux densities is experimentally investigated. In a first step, a literature review on the application of enhanced tubes in nitrate salt heat exchangers is performed: it is found that the commonly used general correlation suggested

by Ravigururajan et al. overpredicts the experimental results of the Nusselt number of four different authors by 15% up to 90%. In addition, the general correlation for the friction factor ratio overpredicts the available experimental data by a factor of 1.7 up to 2.3. The same setup, that was used for the smooth tube, is used to deduce the Nusselt number and the pressure difference over a spirally grooved test tube. The investigated grooved tube has a relative groove height of $e/d_i$=0.017, a relative groove pitch of $p/d_i$=0.913 and a groove angle $\alpha$=73.8°. The measurements of the forced convective heat transfer are undertaken for three main bulk salt inlet temperatures: 300 °C, 400 °C and 550 °C, leading to Prandtl numbers ranging from 10 to 3.7. At each temperature up to 5 different mass flows are assessed. This approach leads to Reynolds numbers ranging between 11000 and 285000. Up to three different flux densities are applied for each combination of mass flow and temperature: 330 kW/m², 630 kW/m² and 930 kW/m². The experiments yielding the friction factors show that the general correlation developed by Ravigururajan for the friction factor ratio overpredicts the measured friction factor ratio by a factor of 1.8 to 2.9. This result lies considerably outside the uncertainty band of ±50% given by the authors of the general correlation. At the same time, the present results are in the same order of magnitude as the deviations measured by Chen et al. Further research is necessary to understand the origin of this deviation.

During the experiments at Reynolds numbers above 25000, an increase of Nusselt number of roughly 1.19±0.14 is observed with increasing Re numbers. However, the deduced Nusselt number ratios of the spirally enhanced tube are considerably lower than the values predicted by the general correlations developed by Ravigururajan but are still within the uncertainty range of ±20% up to ±50% specified for the general correlations. The measurements in the Re number region 11000-25000 show little to no increase of heat transfer for the spirally grooved tube compared to the smooth tube. This is in contradiction to the measurements conducted by other authors. Film temperatures up to 630 °C are investigated in the spirally grooved tube experiment. Based on the measurements it can be concluded that inner wall temperatures up to 633 °C alone do not lead to a decrease in heat transfer in the present experiment. It must however be pointed out that the systematic decrease in heat transfer towards lower Reynolds numbers could be caused by local salt degradation. On the one hand, the salt has a higher dwell time in the tube at lower Reynolds numbers leaving more time for gaseous products to form and disturbing the heat transfer. On the other hand, it could be that the grooves not only cause a local increase of fluid velocity but can also cause a local decrease in fluid velocity (for example shortly before and after the groove). This could cause local overheating and entail local salt degradation. The formation of a low conductive film on the inner tube wall can be excluded, because the low Reynolds number experiments were repeated at the very beginning and at the end of the measurement campaign and yielded the same results. Further research is necessary to quantify the observed Nusselt number behavior for Re= 10000 to 25000 in the spirally grooved tube and define its origin with certainty. Furthermore, the present experiments were only carried out over a duration of a few weeks. Consequently, it cannot be excluded that long-term operation at high film temperatures would lead to the formation of a low conductance surface layer and to a local decrease of thermal conductivity of the tube. Further research is required to yield data in long-term operation.

# 7 Bibliography

[1] G. Janz, "Thermodynamic and transport properties for molten salts: correlated equations for critically evaluated density, surface tension, electrical conductance, and viscosity data," *J. Phys. Chem. Ref. Data (Supplement 2) 17,* p. 1–320, 1988.

[2] P. Falcone, A Handbook for Solar Central Receiver Design, Sandia National Laboratories Livermore SAND 86-8009, 1986.

[3] A. Kuchibhotla, D. Banerjee and V. Dhir, "Forced convection heat transfer of molten Salts: A review," *Nuclear Engineering and Design 362,* 2020.

[4] M. Mehos, C. Turchi, J. Vidal, M. Wagner, Z. Ma, C. Ho, W. Kolb, C. Andraka and A. Kruizenga, "Concentrating Solar Power Gen3 Demonstration Roadmap," National Renewable Energy Laboratory, Golden, Colorado, 2017.

[5] D. C. Smith, "Design and optimization of tube-type receiver panels for molten salt application," *Solar Engineering Vol. 2,* ASME 1992.

[6] R. Uhlig, C. Frantz and R. Buck, "Using corrugated tubes in external molten salt receivers," *AIP Conference Proceedings 2126,* 2019.

[7] R. M. Manglik, "Chapter 11: Enhancement of Convective Heat Trans," in *Handbook of Thermal Science and Engineering*, Springer International Publishing AG, 2018, pp. 447-477.

[8] C. Frantz, M. Ebert, M. Binder, M. Muhr, A. Heinrich and C. Schuhbauer, "Basic engineering of a high performance molten salt tower receiver system," *AIP Conference Proceedings 2445,* 2022.

[9] A. Bonk, M. Braun, V. A. Sötz and T. Bauer, "Solar Salt – Pushing an old material for energy storage to a new limit," *Applied Energy 262,* 2020.

[10] S. Giuliano , M. Puppe, C. Frantz, R. Uhlig, R. Flesch and T. Baumann, "High Performance Molten Salt Tower Receiver System Entwicklung eines hocheffizienten Receiversystems für Salzturmkraftwerke," German Aerospace Center (DLR), Stuttgart, 2016.

[11] O. Reynolds, "An Experimental Investigation of the Circumstances Which Determine Whether the Motion of Water Shall Be Direct or Sinuous and of the Law of Resistance in Parallel Channels," *Philosophical Transactions Royal Society London 174,* vol. 174, pp. 935-982, 1883.

[12] W. Polifke and J. Kopitz, Wärmeübertragung, Germany: Pearson Studium, 2009.

[13] H. D. Baehr and K. Stephan, Wärme- und Stoffübertragung, Berlin: Springer Vieweg Berlin, Heidelberg, 2016.

[14] T. L. Bergman, A. S. Lavine, F. P. Incropera and D. P. Dewitt, Fundamentals of Heat and Mass Transfer, USA: John Wiley & Sons, Inc., 2011.

[15] H. Schlichting and K. Gersten, Grenzschicht-Theorie, Germany: Springer-Verlag Berlin Heidelberg, 2006.

[16] B. S. Petukhov, "Heat Transfer and Friction in Turbulent Pipe Flow with Variable Physical Properties," *Advances in Heat Transfer,* vol. 6, pp. 503-564, 1970.

[17] S. Kakac, R. K. Shah and W. Aung, Handbook of single-phase convective heat transfer, United States, 1987.

[18] V. Gnielinski, "Neue Gleichungen für den Wärme- und den Stoffübergang in turbulent durchströmten Rohren und Kanälen," *Forschung auf dem Gebiet des Ingenieurwesens,* vol. 41, no. 1, pp. 8-16, 1975.

[19] V. D. I. V.-G. V. u. Chemieingenieurwesen, VDI-Wärmeatlas 10. Auflage, 2006.

[20] R. H. S. Winterton, "Where did the Dittus and Boelter equation come from?," *International Journal of Heat and Mass Transfer,* vol. 41, pp. 809-810, 1998.

[21] E. N. Sieder and G. E. Tate, "Heat transfer and pressure drop of liquids in tubes," *Ind. Eng. Chem.,* vol. 28, pp. 1429 - 1435, 1936.

[22] C. Frantz, R. Buck, M. Röger and B. Hoffschmidt, "Experimental Analysis of Forced Convective Heat Transfer of Nitrate Salt in a Circular Tube at High Reynolds Numbers and Temperatures," *International Journal of Heat and Mass Transfer,* no. 201, 2023.

[23] L. F. Moody, "Friction Factors for Pipe Flow," *Transactions of the ASME,* vol. 66, pp. 671-684, 1944.

[24] J. Davies and P. Simpson, Induction Heating Handbook, New York (USA): McGraw-Hill, 1979.

[25] B. Nacke and E. Baake, Induktives Erwärmen, Germany: Vulkan Verlag GmbH, 2014.

[26] S. Lupi, M. Forzan and A. Aliferov, Induction and Direct Resistance Heating, Switzerland: Springer International Publishing, 2015.

[27] S. Zinn and S. L. Semiatin, Elements of Induction Heating - Design, Control, and Applications, Ohio, USA: Electric Power Research Institute, Inc., 2002.

[28] J. Pacheco, "Final Test and Evaluation Results from the Solar Two Project," Sandia National Laboratories, Albuquerque, New Mexico, 2002.

[29] N. E. Bergan, "Testing of the Molten Salt Electric Experiment Solar Central Receiver in an External Configuration," Sandia National Laboratories (SAND 86-8010), Livermore, 1986.

[30] A. Amri, M. Izygon, B. Tedjiza and C. Etievant, "Central Receiver Plant Evaluation III) Themis Receiver Subsystem Evaluation," Sandia National Laboratories (SAND88-8101), Albuquerque, New Mexico (USA), 1988.

[31] J. Dersch, M. Binder, C. Frantz, G. Giuliano, F. Gross and H. Hasselbach, "Blueprint for Molten Salt CSP Power Plant," German Federal Ministry for Economic Affairs and Energy, Germany, 2021.

[32] J. Lata, M. Rodriguez and M. Alvarez de Lara, "High Flux Central Receivers of Molten Salts for the New Generation of Commercial Stand-Alone Solar Power Plants," *Journal of Solar Energy Engineering,* vol. Vol. 130, 2008.

[33] SolarReserve, *CSP Project Fact Sheet,* Nevada, USA: SolarReserve, September 2013.

[34] S. Relloso and Y. Gutierrez, "SENER molten salt tower technology. Ouarzazate NOOR III case," *AIP Conference Proceedings,* vol. 1850, 2017.

[35] CSP Plaza, "Michel Lalmand, Vice president of CMI Solar Talking about CSP Tower Receiver," *Focus, Viewpoint,* 24 12 2015.

[36] L. Vant-Hull, "The role of Allowable Flux Density in the Design and Operation of Molten-Salt Solar Central Receivers," *Journal of Solar Energy Engineering,* vol. Vol. 124, 2002.

[37] R. Flesch, C. Frantz, D. Maldonado Quinto and P. Schwarzbözl, "Towards an optimal aiming for molten salt power towers," *Solar Energy,* vol. 155, pp. 1273-1281, 2017.

[38] C. Frantz, M. Ebert, B. Schlögl, M. Binder and C. Schuhbauer, "Experimental Receiver Setup of a High Performance Molten Salt Test Receiver System," in *SolarPaces 2021*, Albuquerque, 2021.

[39] A. Bonk, M. Braun, A. Hanke, V. A. Sötz and T. Bauer, "Enhancing the thermal stability of solar salt up to 600°C in extended lab-scale experiments," *AIP Conference Proceedings SolarPaces2019,* p. 2303, 2020.

[40] H. Hoffman, "Turbulent Forced Convection Heat Transfer in Circular Tubes Containing Molten Sodium Hydroxide," Oak Ridge National Laboratory, USA, 1952.

[41] M. Grele and L. Gedeon, "Forced-convection heat-tansfer characteristics of molten sodium hydroxide," National Advisory Commitee for Aeronautics, Washington, USA, 1953.

[42] H. Hoffman and J. Lones, "Fused salt heat transfer part II: Forced Convection Heat Transfer in Circular Tubes Containing NaF-KF-LiF Eutectic," Oak Ridge National Laboratory, USA, 1955.

[43] M. D. Grele and L. Gedeon, "Forced-Convection Heat Transfer Characteristics of Molten FLINAK Flowing in an Inconel X System," National Advisory Committee for Aeronautics, Washington, USA, 1958.

[44] B. Vriesema, "Aspects of Molten Fluorides as Heat Transfer Agents for Power Generation," Dissertation, Technische Hogeschool Delft, Delft, Netherlands, 1979.

[45] J. Ambrosek, M. Anderson, K. Sridharan and T. Allen, "Current Status of Knowledge of the Fluoride Salt (FLiNaK) Heat Transfer," *Nuclear Technology 165:2,* pp. 166-173, 2009.

[46] V. Ignat'ev, S. V. Keronovskii, A. I. Surenkov, O. P. Shcherbanyuk, S. Manchkha and Y. B. Smirnov, "Heat Exchange during the Flow of a Melt of LiF-NaF-KF Fluoride Salts in a Circular Tube," *Translated from Atomnaya Energiya Vol. 57 No. 2,* pp. 123-124, 1984.

[47] J. W. Cooke and B. Cox, "Forced-Convection Heat-transfer measurements with a molten fluoride salt mixture flowing in a smooth tube," Oak Ridge National Laboratory, USA, 1973.

[48] M. D. Silverman, W. Huntley and H. Robertson, "Heat Transfer Measurements in a Forced Convection Loop with Two Molten-Fluoride Salts: LiF-BeF2-ThF2-UFq and Eutectic NaBF4-NaF," Oak Ridge National Laboratory, USA, 1976.

[49] L. Bin, W. Yu-ting, M. Chong-fang, Y. Meng and G. Hang, "Turbulent convective heat transfer with molten salt in a circular pipe," *International Communications in Heat and Mass Transfer 36,* pp. 912-916, 2009.

[50] W. Yu-ting, L. Bin, M. Chong-fang and G. Hang, "Convective heat transfer in the laminar–turbulent transition region with molten salt in a circular tube," *Experimental Thermal and Fluid Science ,* vol. 33, p. 1128–1132, 2009.

[51] H. W. Hoffman and S. I. Cohen, "Fused Salt Heat Transfer - Part III: Forced-Convection Heat Transfer in Circula Tubes Containing The Salt Mixture NaNO2-NaNO3-KNO3," Oak Ridge National Laboratory, USA, 1960.

[52] W. E. Kirst, W. M. Nagle and J. B. Castner, "A new heat transfer medium for high temperatures," *Trans. Am. Inst. Chem. Eng. 36,* pp. 371-394, 1940.

[53] Y.-T. Wu, C. Chen, B. Liu and C.-F. Ma, "Investigation on forced convective heat transfer of molten salts in circular tubes," *International Communications in Heat and Mass Transfer 39,* p. 1550–1555, 2012.

[54] Y. S. Chen, Y. Wang, J. H. Zhang, X. F. Yuan, J. Tian and Z. F. Tang, "Convective heat transfer characteristics in the turbulent region of molten salt in concentric tube," *Applied Thermal Engineering 98,* pp. 213-219, 2016.

[55] Y.-L. He, Z.-J. Zheng, B.-C. Du, K. Wang and Y. Qiu, "Experimental investigation on turbulent heat transfer characteristics of molten salt in a shell-and-tube heat exchanger," *Applied Thermal Engineering 108,* p. 1206–1213, 2016.

[56] S. Xiangyang, J. Lu, J. Ding and J. Yang, "Convective heat transfer of molten salt in circular tube with nonuniform heat flux," *Experimental Thermal and Fluid Science 55,* p. 6–11, 2014.

[57] L. Jianfeng, X. Shen, J. Ding, Q. Pan and Y. Wang, "Convective heat transfer of high temperature molten salt in transversely grooved tube," *Applied Thermal Engineering 61,* pp. 157-162, 2013.

[58] A. Das, M. M. Clark, B. C. Teigen, W. A. Fiveland and M. H. Anderson, "Heat Transfer Behavior of Molten Nitrate Salt," *AIP Conference Proceedings 1734,* 2016.

[59] C. Frantz, R. Buck, M. Röger and B. Hoffschmidt, "Experimental analysis of forced convective heat transfer of nitrate salt in a spirally groove d tub e at high Reynolds numb ers and temperatures," *International Journal of Heat and Mass Transfer,* no. 204, 2023.

[60] A. E. Bergles, R. L. Webb, G. H. Junkhan and V. Nirmalan, "Bibliography on augmentation of convective heat and mass transfer - II," Iowa State Univesity, Ames, 1983.

[61] S. K. Saha, M. Tiwari, B. Stundén and Z. Wu, Advances in Heat Transfer Enhancement, India: Springer Briefs in Applied Sciences and Technology, 2016.

[62] T. S. Ravigururajan and A. E. Bergles, "Development and Verification of General Correlations for Pressure Drop and Heat Transfer in Single-Phase Turbulent Flow in Enhanced Tubes," *Experimental Thermal and Fluid Science,* pp. 55-70, 1996.

[63] G. Y. Min, "The studies on the transversally corrugated tubes strengthening heat-transfer and resisting fouling in the evaporation station of sugar factory," *J. Qiqihar Light Ind. Inst.,* vol. 10, no. 1, pp. 19-25, 1994.

[64] T. S. Ravigururajan and T. J. Rabas, "Turbulent Flow in Integrally Enhanced Tubes, Part 2: Analysis and Performance Comparison," *Heat Transfer Engineering,* vol. 17:2, pp. 30-40, 1996.

[65] R. M. Manglik, A. E. Bergles, A. J. Dongaonkar and S. Rajendran, "Limitations of Compiling the Global Literature on Enhanced Heat and Mass Transfer," *Journal of Enhanced Heat Transfer,* vol. 20, no. 1, pp. 83-92, 2013.

[66] R. I. Webb, "Principles of Enhanced Heat Transfer," in *Wiley Interscience first ed.*, New York, 1994.

[67] R. L. Webb, E. R. G. Eckert and R. J. Goldstein, "Heat Transfer and Friction in Tubes with Repeated-Rib Roughness," *Int. J. Heat Mass Transfer,* vol. 14, no. 4, pp. 601-618, 1971.

[68] D. L. Gee and R. L. Webb, "Forced Convection Heat Transfer in Helically Rib-Roughened Tubes," *Int. J. Heat Mass Transfer,* vol. 23, pp. 1127-1136, 1980.

[69] H. M. Li, K. S. Ye, Y. K. Tan and S. J. Deng, "Investigation on Tube-Side Flow Visualization, Friction Factors and Heat Transfer Characteristics of Helical-Ridging Tubes,," *7th International Heat Transfer Conference,* vol. 3, pp. 75-80, 1982.

[70] A. García, P. Vicente and A. Viedma, "Experimental study of heat transfer enhancement with wire coil inserts in laminar-transition-turbulent regimes at different Prandtl numbers," *International Journal of Heat and Mass Transfer,* vol. 48, p. 4640–4651, 2005.

[71] W.-T. Ji, A. M. Jacobi, Y.-L. He and W.-Q. Tao, "Summary and evaluation on single-phase heat transfer enhancement techniques of liquid laminar and turbulent pipe flow," *International Journal of Heat and Mass Transfer,* vol. 88, pp. 735-754, 2015.

[72] J. F. Fan, W. K. Ding, J. F. Zhang, Y. L. He and W. Q. Tao, "A performance evaluation plot of enhanced heat transfer techniques oriented for energy-saving," *International Journal of Heat and Mass Transfer,* vol. 52, p. 33–44, 2009.

[73] W.-T. Ji, A. M. Jacobi, Y.-L. He and W.-Q. Tao, "Summary and evaluation on the heat transfer enhancement techniques of gas laminar and turbulent pipe flow," *International Journal of Heat and Mass Transfer,* vol. 111, p. 67—483, 2017.

[74] L. Jiangfeng, X. Sheng, J. Ding and J. Yang, "Transition and turbulent convective heat transfer of molten salt in spirally grooved tube," *Experimental Thermal and Fluid Science,* vol. 47, pp. 180-185, 2013.

[75] L. Jiangfeng, J. Ding, T. Yu and X. Shen, "Enhanced heat transfer performances of molten salt receiver with spirally grooved pipe," *Applied Thermal Engineering,* vol. 88, pp. 491-498, 2015.

[76] C. Chen, Y.-T. Wu, S.-T. Wang and C.-f. Ma, "Experimental investigation on enhanced heat transfer in transversally corrugated tube with molten salt," *Experimental Thermal and Fluid Science,* vol. 47, p. 108–116, 2013.

[77] S. Xiangyang, J. Ding and J. Lu, "Enhanced heat transfer characteristics of molten salt in half-circumferentially heated horizontally corrugated tubes," *CIESC Journal,* vol. 70, no. 12, pp. 4546-4555, 2019.

[78] BASF SE, "https://chemicals.basf.com," BASF SE, 30 01 2022. [Online]. Available: https://chemicals.basf.com/global/en/Monomers/chemicals-and-servcies-for-solar-industries.html.

[79] SQM International N.V., "https://www.sqm.com/," 30 01 2022. [Online]. Available: https://www.sqm.com/en/producto/sales-termo-solares/.

[80] R. W. Bradshaw and R. W. Carling, "A review of the chemical and physical properties of molten alkali nitrate salts and their effect on materials used for solar central receivers," *Report SAND87-8005; Sandia National Laboratories: Albuquerque, New Mexico, USA,* 1987.

[81] A. Bonk, M. Braun, A. Hanke, J. Forstner, V. A. Sötz and T. Bauer, "Influence of Different Atmospheres on Molten Salt Chemistry and its Effect on Steel Corrosion," *AIP Conference Proceedings 2033, 090003,* 2017.

[82] V. A. Sötz, A. Bonk, J. Forstner and T. Bauer, "Microkinetics of the reaction NO3- ⇌NO2- +0.5 O2 in molten sodium nitrate and potassium nitrate salt," *Thermochim Acta,* p. 678, 2019.

[83] A. Kruizenga, W. Kolb, R. J. Briggs, J. M. Christian, D. A. Ray, D. Gill, J. W. Kelton and K. M. Chisman, "Loop for the Observation of Film Temperature Effects on Decomposition (LOFTED)," Sandia National Laboratories (SAND2014-18103), Albuquerque, New Mexico (USA), 2014.

[84] D. Nissen and D. Meeker, "Nitrate-nitrite chemistry in NaNO3-KNO3 melts," *Inorg Chem,* 1983.

[85] M. Walczak, F. Pineda, A. G. Fernández, C. Mata-Torres and R. A. Escobar, "Material corrosion for thermal energy storage systems in concentrated solar power plants," *Renewable and Sustainable Energy Reviews 86,* pp. 22-44, 2018.

[86] F. Sutter, C. Oskay, M. Galetz, T. Diamantino, F. Pedrosa, I. Figueira and et al., "Dynamic corrosion testing of metals in solar salt for concentrated solar power," *Solar Energy Materials and Solar Cells 232,* 2021.

[87] M. Li, R. Endo, M. Akoshima, H. Tanei, H. Okada and M. Susa, "Thermal Conductivity of Oxide Scale Thermally Grown on Iron Substrate Corrected by Temperature-dependent Interfacial Thermal Resistance in Laser Flash Measurement," *ISIJ International,* vol. Vol. 59, no. No. 3, pp. 398-403, 2019.

[88] R. Endo, T. Yagi, M. Ueda and M. Susa, "Thermal Diffusivity Measurement of Oxide Scale Formed on Steel during Hot-rolling Process," *ISIJ International,* vol. Vol. 54, no. No. 9, pp. 2084-2088, 2014.

[89] B. Muñoz-Sánchez, J. Nieto-Maestre and J. González-Aguilar, "Round robin test on the measurement of the specific heat of solar salt," *AIP Conference Proceedings 1850,* (2017.

[90] B. D'Aguanno, M. Karthik, A. N. Grace and A. Floris, "Thermostatic properties of nitrate molten salts and their solar and eutectic mixtures," *Sci Rep,* 2018.

[91] A. Bonk and T. Bauer, "Report on thermo-physical properties of binary NaNO3-KNO3 mixtures in a range of 59-61 wt% NaNO3," German Aerospace Center (DLR), Germany, 2021.

[92] TA Instruments, "Making Accurate DSC and MDSC Specific Heat Capacity Measurements with the Q1000 Tzero DSC," TA Instruments, New Castle, USA.

[93] T. Bauer, N. Pfleger, N. Breidenbach, M. Eck, D. Laing and S. Kaesche, "Material aspects of Solar Salt for sensible heat storage," *Applied Energy, Volume 111,* pp. Pages 1114-1119, 2013.

[94] D. J. Rogers and G. J. Janz, "Melting-Crystallization and Premelting Properties of NaN03-KN03 Enthalpies and Heat Capacities," *J. Chem. Eng. Data, 27,* pp. 424-428, 1982.

[95] C. Jung, "Heat Capacity of Molten Solar Salt," in *SolarPACES 2021*, Albuquerque, 2021.

[96] T. Bauer, N. Pfleger, D. Laing, W.-D. Steinmann, M. Eck and S. Kaesche, "Chapter 20: High temperature molten salts for solar power application," in *Molten Salt Chemistry: From Lab to Applications*, ed. by F. Lantelme, H. Groult (Elsevier, Amsterdam, 2013).

[97] G. J. Janz, U. Krebs, H. F. Siegenthaler and R. P. T. Tomkins, "Molten salts: volume 3 nitrates, nitrites, and mixtures: electrical conductance, density, viscosity, and surface tension data.," *J. Phys. Chem. Ref. Data 1,* p. 581–746, 1972.

[98] D. Nissen, "Thermophysical properties of the equimolar mixture sodium nitrate-potassium nitrate from 300 to 600°C," *J. Chem. Eng. Data 27,* p. 269–273, 1982.

[99] T. Bauer and A. Bonk, "Semi-empirical Density Estimations for Binary, Ternary and Multicomponent Alkali Nitrate–Nitrite Molten Salt Mixtures," *International Journal of Thermophysics,* pp. 39-134, 2018.

[100] Q. Zhao, C.-X. Hu, S.-J. Liu, H. Guo and Y.-T. Wu, "The thermal conductivity of molten NaNO3, KNO3, and their mixtures," *Energy Procedia 143,* p. 774–779, 2017.

[101] H. Bloom, A. Doroszkowski and S. B. Tricklebank, "Molten salt mixtures - The thermal conductivities of molten nitrate systems," *Australian Journal of Chemistry 18,* pp. 1171-1176, 1965.

[102] T. Foosnæs, "Thermal Conductivity of Nitrate Mixtures," Sandia National Laboratories Report SAND80-8191, 1982.

[103] T. Omotani, Y. Nagasaka and A. Nagashima, "Measurement of the Thermal Conductivity of KNO3-NaNO3 Mixtures Using a Transient Hot-Wire Method with a Liquid Metal in a Capillary Probe," *International Journal of Thermophysics 3,* pp. 17-26, 1982.

[104] R. Tufeu, J.-P. Petitet, L. Denielou and B. Le Neindre, "Experimental Determination of the Thermal Conductivity of Molten Pure Salts and Salt Mixtures," *International Journal of Thermophysics, Vol. 6, No. 4,* 1985.

[105] Q.-G. Zhao, S.-J. Liu, H. Guo and X. Chen, "A theoretical model for predicting the thermal conductivity of binary molten salts," *International Journal of Heat and Mass Transfer 92,* pp. 639-642, 2016.

[106] A. B. Zavoico, "Design Basis Document," Sandia National Laboratories SAND2001-2100, Albuquerque, 2001.

[107] K. A. Tasidou, C. D. Chliatzou, M. J. Assael, K. D. Antoniadis, S. K. Mylona, M. L. Huber and W. A. Wakeham, "Reference Correlations for the Viscosity of 13 Inorganic Molten Salts," *Journal of Physical and Chemical Reference Data, 48,* 2019.

[108] I. Murgulescu and S. Zuca, "Viscosity of binary mixtures of molten nitrates as a function of ionic radius," *Electrochimica Acta Vol 14.,* pp. 519-526, 1969.

[109] C. H. Hamann and W. Vielstich, Elektrochemie, Weinheim: WILEY-VCH Verlag GmbH & Co, 2005.

[110] J. Zhang, "A review of steel corrosion by liquid lead and lead–bismuth," *Corrosion Science,* vol. 51, p. 1207–1227, 2009.

[111] Y. Dai, X. Zheng and P. Ding, "Review on sodium corrosion evolution of nuclear-grade 316 stainless steel for sodium-cooled fast reactor applications," *Nuclear Engineering and Technology,* vol. 53, pp. 3474-3490, 2021.

[112] A. Gomes, M. Navas, N. Uranga, T. Paiva, I. Figueira and T. C. Diamantino, "High-temperature corrosion performance of austenitic stainless steels type AISI 316L and AISI 321H, in molten Solar Salt," *Solar Energy Volume 177,* pp. 408-419, 2019.

[113] D. Rückle, Das Oxidationsverhalten und die elektrochemische Charakterisierung von Stählen in Nitratschmelzen bei hohen Temperaturen, Dissertation, Universität Stuttgart, 2019.

[114] A. Kruizenga and D. Gill, "Corrosion of Iron Stainless Steels in Molten Nitrate Salt," *Materials Science,* 2014.

[115] N. Breidenbach, C. Martin, H. Jockenhöfer and T. Bauer, "Thermal Energy Storage in Molten Salts: Overview of Novel Concepts and the DLR Test Facility TESIS," *Energy Procedia,* vol. 99, pp. 120-129, 2016.

[116] 100:2008 JCGM, *Evaluation of measurement data — Guide to the expression of uncertainty in measurement (GUM 1995 with minor corrections),* Joint Committee for Guides in Metrology, 2010.

[117] L. Prandtl, Führer durch die Strömungslehre, 3. Auflage, Braunschweig, 1950.

[118] A. H. Harvey, "Reference Correlations for Thermophysical Properties of Liquid Water at 0.1 MPa," National Institute of Standards and Technology, J. Phys. Chem. Ref. Data, Vol. 38, No. 1, 2009.

[119] International Association for the Properties of Water and Steam, "Guideline on the Use of Fundamental Physical Constants and Basic Constants," available at www.iapws.org, 2008.

[120] R. S. Graves, T. G. Kollie, D. L. McElroy and K. E. Gilchrist, "The Thermal Conductivity of AISI 304L Stainless Steel," *International Journal of Thermophysics, Vol. 12, No. 2, 1991.*

[121] J. Matolich Jr., "Thermal conductivity and electrcical resistivity of type 316 Stainless Steel from 0 to 1800F," *NASA CR-54151,* 1965.

[122] Sandmeyer Steel Company, "Specification Sheet: Alloy 321/321H," 2014.

[123] Hans Kohler AG, "Werkstofftabelle Kapitel 7," 2012.

[124] VDM Metals, *VDM® Alloy 800 Nicrofer 3220,* Germany: VDM Metals, 2017.

[125] Penn Stainless Products, *Alloy 347/347H Specifications: UNS S34700/S34709,* 2022.

[126] Haynes International, *HAYNES® 230® alloy,* Haynes International, 2021.

[127] Y. Wang, X. Hu, M. Jiang, J. Wang, M. Wei and L. Zhang, "Temperature field characterization and optimization of temperature field distribution in pipe lining process based on electromagnetic induction heating system," *Case Studies in Thermal Engineering,* vol. 28, 2021.

[128] D. Peckner and I. M. Bernstein, Handbook of Stainless Steel, USA: McGraw-Hill Book Company, 1977.

[129] J. A. Malina and E. M. Sparrow, "Variable-property, constant-property, and entrance-region heat transfer results for turbulent flow of water and oil in a circular tube," *Chemical Engineering Science,* vol. 19, no. 12, pp. 953-962, 1964.

[130] R. W. Bradshaw and S. H. Goods, "Effect of Temperature on Corrosion of Type 316 SS by Molten NaNO3-KNO3," Sandia National Laboratories, Livermore, CA 94551-0969.

# Appendix

## Table of Contents Appendix

Appendix A:

Table A-1: Flow conditions in Central Solar Receivers ..... 92

Appendix B:Figure B-1: Uncertainty of specific isobaric heat capacity $\Delta c_p/c_p$ ..... 93

Figure B-2: Relative deviation of the specific isobaric heat capacity at 0.1 MPa from the IAPWS-95 correlation ..... 93

Figure B-3: Material composition from material certificate of test tube ..... 94

Figure B-4: Thermal conductivity of several austenitic stainless steels as a function of temperature. The deduced correlation is shown in dashed lines. Error bars indicate ±7% [118], [119], [120], [121]. ..... 94

Figure B-5: Electric resistivity of a selection of austenitic steels and nickel-base alloys [121], [120], [119], [122], [123], [124], [118] ..... 95

Appendix C:Figure C-1: Schematic setup single electrode electrolysis test ..... 97

Table C-2: Test matrix single electrode electrolysis experiment ..... 97

Figure C-3: Left: Schematic setup of cyclic voltammetry experiment; Right: Pictures of cyclic voltammetry experiment ..... 98

Table C-4: Test matrix cyclic voltammetry experiment ..... 99

Table C-5: Test procedure cyclic voltammetry experiment with Solar Salt ..... 99

Appendix D:Figure D-1: CAD drawing of test section ..... 100

Figure D-2: Isometric view of the solenoid multiturn coil ..... 100

Figure D-3: Screenshot of control system molten salt Test Setup ..... 101

Figure D-4: Top view TESIS:com test section ..... 101

Figure D-5: Side view TESIS:com test section ..... 102

Figure D-6: Picture of molten salt Test Section during installation (before insulation) ..... 102

Figure D-7: Picture of molten salt Test Section after insulation ..... 102

Table D-8: Test matrix test setup with Solar Salt and smooth tube ..... 104

Table D-9: Test matrix test setup with Solar Salt and spirally grooved tube ..... 106

Figure D-10: Simplified piping and instrumentation diagram of water test setup ..... 107

Figure D-11: CAD drawing of water test setup ..... 107

Figure D-12: Picture of water test setup ..... 108

Table D-13: Test matrix validation tests with water and smooth tube ..... 108

Appendix E:Figure 0-1: Left: Exemplary spirally grooved tubes with one thread (top) and three threads (bottom); Right: Geometry definition of spirally grooved tube ..... 109

Table 0-2: Evaluated enhanced tube geometries ..... 110

Figure 0-3: Nusselt number ratio (left) and friction factor ratio (right) calculated for different enhanced tube geometries using the general correlations by Ravigururajan ..... 110

Figure 0-4: Measured surface geometry of spirally grooved tube (left) and deduced geometry factors ..... 111

Appendix F:Figure F-1: Left: Test tube before mounting; Right: Close-up of outer wall thermocouples with one spot welded thermocouple at the center of the image and two laser welded thermocouples at the sides of the tube ..... 112

Figure F-2: Comparison of thermocouple before and after application of laser weld ..... 113

Figure F-3: Left: Exemplary radial temperature profiles for a constant applied heating flux density and convective cooling rate for all four heat conductivity assumptions; Right: Deviation of expected outer wall temperature at different heat conductivity assumptions from ideal assumptions ..... 114

Figure F-4: Exemplary result of FEM analysis of tank deformation (150 mm salt level, 560°C salt temperature) ..... 116

Figure F-5: Correction factors curves and correlations for salt level measurement ..... 116

Figure F-6: Relative uncertainty of mean mass flow measurement using the radar level sensors as a function of measured height difference in the salt tank ..... 116

Figure F-7: Validation of mean mass flow measurement using radar level sensors with high temperature Coriolis sensor ..... 117

Figure F-8: Exemplary mass flow measurements showing the qualitative measurement of the ultrasonic mass flow sensors ..... 118

Figure F-9: Phase angle as a function of tube outer wall temperature ..... 119

Table F-10: Summary of assumptions for the phase angle ..... 119

Appendix G:Table G-1: Deduction of expected active power induced in the Solar Salt..... 120

Figure G-2: p and q functions for a solid cylinder [23]..... 121

Figure G-3: Results of transient thermal FEM simulation of inner (T_t,i) and outer tube wall temperature (T_t,o) of the test section and outer insulation temperature (T_ins,o) as a function of time since start of salt flow at $T_s$: 560 °C (left) and after a 50 K temperature step (right) ..... 122

Figure G-4: Results of transient thermal FEM simulation of heat losses to ambient and temperature gradient rate as a function of time since start of salt flow at $T_s$: 560 °C (left) and after a 50 K temperature step (right) ..... 123

Table G-5: Assumptions for optimistic and conservative peripheral pressure drop [19]..... 124

Figure G-6: Proportion of $\Delta p_{per}$ on total measured pressure difference $\Delta p_{s,total}$..... 125

Figure G-7: Relative deviation between the calculated pressure difference assuming optimistic and conservative assumptions as a function of bulk flow velocity and salt temperature..... 125

# A. Flow Conditions in Central Solar Receivers

The geometric and thermal specifications prevalent in molten salt receivers are collected for demonstration plants and commercial plants from the literature. For this purpose, the publicly available data of several different molten salt receivers is analyzed: Solar Two [28], MSEE [29], Thémis [30], HPMS-I external receivers [10], CSP Reference plant [31], Gemasolar [32], Crescent Dunes [33], NOOR III [34] and Atacama 1 [35]. The available data is summarized in Table A-1

| | **Solar Two [28]** | **MSEE [29]** | **Thémis [30]** | **Gema-solar [32]** | **Crescent Dunes [33]** | **CSP Reference plant [31]** | **HPMS-I [10]** | **NOOR III [34]** |
|---|---|---|---|---|---|---|---|---|
| Heat transfer fluid | Solar Salt | Solar Salt | HITEC | Solar Salt | Solar Salt | Solar Salt | Solar Salt | Solar Salt |
| Bulk inlet temperature Receiver (°C) | 290 | 290 | 250 | 290 | 287 | 290 | 290 | 300 |
| Bulk outlet temperature Receiver (°C) | 565 | 566 | 450 | 565 | 565 | 565 | 565 | 565 |
| Reynolds number Inlet (-) | 37000 | 22000 | 29000 | 46000 | | | 81000 | |
| Reynolds number Outlet (-) | 121000 | 73000 | 85000 | 150000 | | | 266000 | |
| Irradiated height (m) | 6.2 | 3.5 | 4 | 10 | 22 | 22.8 | 25.7 | |
| Inner diameter tube (mm) | 18.6 | 15.7 | 15 | 21.7 | | | 32.8 | |
| Outer diameter tube (mm) | 21 | 19 | 18 | 25 | 50 | | 38 | |
| Peak Flux ($kW/m^2$) | 850 | 630 | 800 | 1000 | | | | |
| Mean Flux ($kW/m^2$) | 430 | 260 | 390 | | | 536 | | |
| Thermal rating ($MW_{th}$) | 42.2 | 5 | 9 | 120 | | 700 | 700 | 660 |
| $L/d_i$ | 333 | 223 | 267 | 461 | | 792 | 784 | |

Table A-1: Flow conditions in Central Solar Receivers

# B. Thermophysical Properties of Water and Test Tube

This subsection contains the summary of the selected thermophysical properties of liquid water (appendix B.1) and of the test tube (appendix B.2).

## B.1. Thermophysical Properties of Liquid Water

The thermophysical properties of the main water flow and the cooling water flow is computed using the reference correlations of liquid water published by Harvey et al. [118]. The validity of these formulas is given in the following interval: -20 to 110°C and 1 to 3 bara. These formulas are based for pure $H_2O$ with the standard isotopic composition for hydrogen and oxygen given by Vienna Standard Mean Ocean Water (VSMOW) [119]. Natural water does have an isotopic composition differing slightly from that of the VSMOW, however the difference is negligible for all properties, with exception of the density, where isotopic composition could affect the most precise measurements [118]. The used water is in contact with the atmosphere in the tank and can therefore be fully or partially saturated with air at atmospheric pressure. This has a negligible effect on all properties, again except for the density [118].

Estimates of the uncertainty of the isobaric heat capacity between the IAPWS-95 correlations in the liquid region are assumed to be in the range of ±0.1% (see Figure B-1) The additional uncertainty caused by usage of the simplified correlations is shown in Figure B-2.

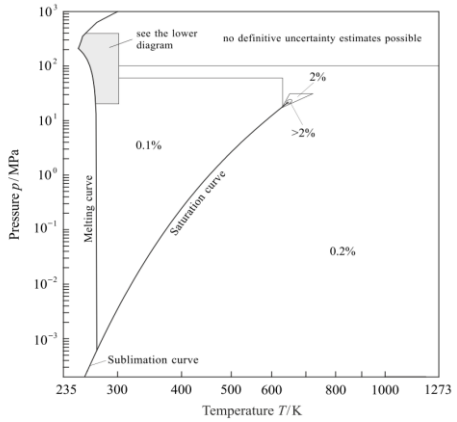


Figure B-1: Uncertainty of specific isobaric heat capacity $\Delta c_p/c_p$

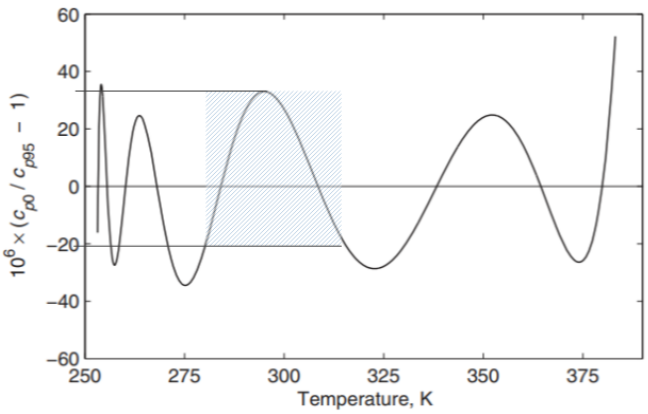


Figure B-2: Relative deviation of the specific isobaric heat capacity at 0.1 MPa from the IAPWS-95 correlation

It can be found that for the considered temperature range the additional uncertainty is roughly 0.004% and hence more than one order of magnitude smaller than the estimated IAPWS-95 correlation. The water pressure has not been monitored during the experiment and will be accounted for as an uncertainty. A maximum deviation of ±0.02% is found at a pressure of 3 bara [118]. This value is accounted for as an uncertainty resulting in an overall relative uncertainty of $\delta c_p = \pm 0.1\ \%$.

The relative uncertainty of the IAPWS correlation for thermal conductivity of liquid water lies between ±1.5% and ±2% [119]. The additional uncertainty caused by usage of the simplified correlations is <±0.0025% over the relevant temperature range. Also, the variation of pressure up to 3 bara only leads to a change in value, which is more than an order of magnitude lower than the order of magnitude of the property itself. This means that approximating the thermal conductivity by the Harvey correlations adds negligible additional uncertainty to the thermal conductivity calculation [118].

## B.2. Thermophysical Properties of the Test Tube

The test section is composed of a seamless stainless steel tube of the material 1.4878. The tubes were solution annealed at 1185°C then rapidly cooled in water. Figure B-3 shows the chemical composition of the material certificate of the tube.

**Chemical composition, % / chemische Zusammensetzung / Composition chimique en % / Массовая доля элементов в %**

| Heat # / Schmelze # / Coulée / № плавки | Melting process / Erschmelzungsart / Process de fabrication de l'acier / Метод выплавки | State / Probe / Etat / Проба | C | Mn | P | S | Si | Cr | Ni | N | Ti |
|---|---|---|---|---|---|---|---|---|---|---|---|
| | | | 0.040 - 0.080 | max 2.00 | max 0.040 | max 0.015 | max 1.00 | 17.00 - 19.00 | 9.00 - 12.00 | max 0.100 | 4*(C+N) - 0.700 |
| 54419 | IM + AOD | Ladle / Schöpfprobe / Poche de coulée / Ковшевая | 0.044 | 1.83 | 0.031 | 0.009 | 0.44 | 17.12 | 9.10 | 0.017 | 0.370 |
| | - | Product / Produkt / Produit / Труба | 0.043 | 1.84 | 0.029 | 0.008 | 0.43 | 17.16 | 9.15 | 0.016 | 0.370 |

Figure B-3: Material composition from material certificate of test tube

For the thermal conductivity of $\lambda_t$, literature data for the used austenitic stainless steel (1.4878) as well as for several similar austenitic steels is collected [120], [121], [122], [123]. The documented thermal conductivity as a function of temperature is shown in Figure B-4.

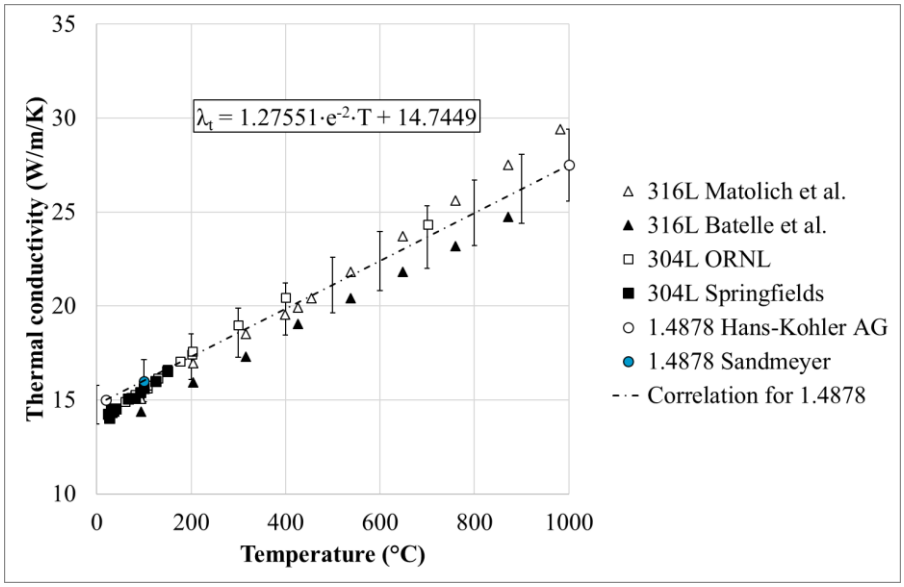


Figure B-4: Thermal conductivity of several austenitic stainless steels as a function of temperature. The deduced correlation is shown in dashed lines. Error bars indicate ±7% [120], [121], [122], [123].

Based on the data found for 1.4878, a linear correlation is deduced using the least square method. The resulting correlation is defined as: $\lambda_t(T) = 1.27551E-2 \cdot T\ (°C) + 14.7449$. It can be seen that almost all given measurement points are found in an interval of ±7% of the correlation. Hence, the following uncertainty is assumed for the tube thermal conductivity uncertainty $\delta_{\lambda_t} = \frac{\pm 7\%}{\sqrt{3}} \cong \pm 4\%$.

The electrical resistivity $\rho_{el}$ quantifies the ability of a material to conduct electric current. Figure B-5 gives an overview of the electric resistivity of a selection of austenitic steels and nickel-based alloys found in the literature and based on manufacturer data as a function of temperature. It can be observed that the electrical resistivity increases with temperature for austenitic steels. This behavior is less pronounced for nickel-based alloys. In this work, the values published by Graves et al. [120] will be used for the test tube. Intermediate values are obtained trough linear interpolation.

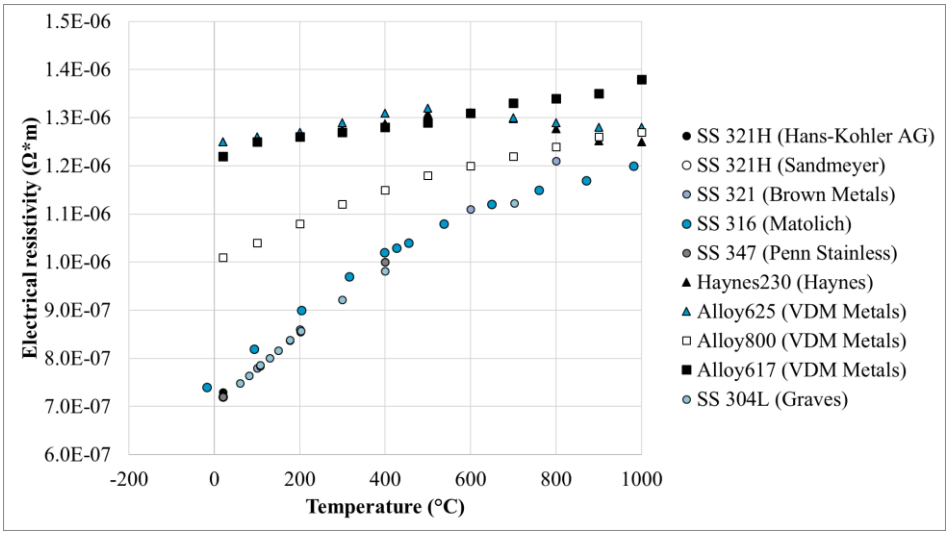


Figure B-5: Electric resistivity of a selection of austenitic steels and nickel-base alloys [123], [122], [121], [124], [125], [126], [120]

The relative magnetic permeability $\mu_r$ quantifies the ability of a material to conduct the magnetic flux in comparison to vacuum or air. Based on their magnetization ability, materials can be divided into three distinct groups: paramagnetic, diamagnetic, and ferromagnetic materials. Paramagnetic and diamagnetic materials show a magnetic permeability slightly higher than one ($\mu_r>1$) and slightly lower than one ($\mu_r<1$) respectively and are generally referred to as non-magnetic materials. In contrast, ferromagnetic materials exhibit magnetic permeability $\mu_r>>1$. Austenitic stainless steel is usually classified as paramagnetic, with permeabilities ranging between 1.003 to 1.05. Ferritic and martensitic steels are usually classified as magnetic, as they possess permeabilities >>1. The relative magnetic permeability of ferromagnetic workpieces gradually decreases for higher temperatures and drops by 5 to 1000 times near the Curie point (~ around 700 °C) [26]. In addition, the relative permeability of ferromagnetic steels depends on the local magnetic field intensity. For non-magnetic materials, the permeability does not change with

temperature or field intensity [127]. In this work, a relative magnetic permeability of $\mu_r$=1.008 is assumed for the austenitic stainless steel 1.4878 (Peckner, [128]).

# C. Preliminary Experiments

Preliminary experiments are carried out to clarify the occurance of ion conduction in a single electrode setup and to quantify the maximum allowable applied potential difference in a setup with molten salt. Appendix chapter C.1 summarizes experimental setup and experimental parameters of the single electrode experiment and appendix chapter C.2 gives additional information about the cyclic voltammetry experiment.

## C.1. Single electrode experiment

The goal of this experiment is to demonstrate experimentally whether ion conduction can principally take place if a potential difference is applied over the length of a tube through which an electrolyte flows. In a classical electrolysis setup, a potential difference is applied to two electrodes (cathode and anode) which are separated by an electrolyte. In the case of the pipe, however, the tube represents a single electrode over which the potential difference decreases continuously from one end to the other. In the case of the pipe it can be argued that no electrolysis reactions would take place because the local potential difference is not high enough. To confirm the single electrode concept in principle, a simple experiment was carried out using a wire to represent the tube and a saline solution to represent the salt: A single NiCr (NiCr6015) wire is placed in a saline solution (Water + NaCl) to which a DC potential difference is applied and both the potential difference and the current through the wire is measured. Figure C-1 shows a schematic of the single electrode experimental setup. The test matrix of the test series is summarized in Table C-2.

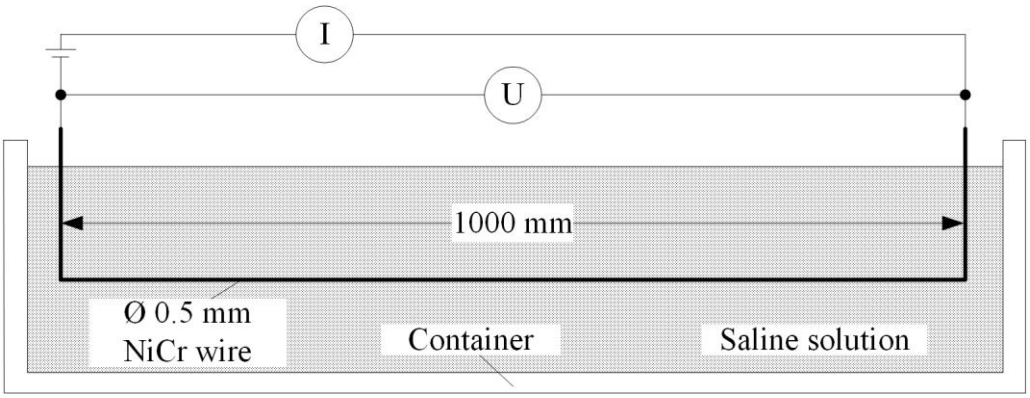


Figure C-1: Schematic setup single electrode electrolysis test

| Wt-% Salt | Applied potential difference (V) | Wt-% Salt | Applied potential difference (V) |
|---|---|---|---|
| 0% | 3, 4, 5, 6, 7.6, 8.7, 11 | 5% | 3, 4, 5, 6, 7.6, 8.7, 11 |
| 2% | 3, 4, 5, 6, 7.6, 8.7, 11 | 6% | 3, 4, 5, 6, 7.6, 8.7, 11 |
| 4% | 3, 4, 5, 6, 7.6, 8.7, 11 | 8% | 3, 4, 5, 6, 7.6, 8.7, 11 |

Table C-2: Test matrix single electrode electrolysis experiment

## C.2. Cyclic voltammetry experiment

The decomposition potential of a system with Solar Salt shall be determined experimentally. For this purpose, a cyclic voltammetry experiment is selected. Cyclic voltammetry is an analytical method that is commonly used to examine various electrode processes. In cyclic voltammetry, first a linearly increasing and then a decreasing potential is applied to a pair of electrodes immersed in an electrolyte. This process is repeated several times, while the current and applied potential difference are measured as a function of time [109]. Figure C-3 shows the schematic setup as well as pictures of the actual setup in the laboratory.

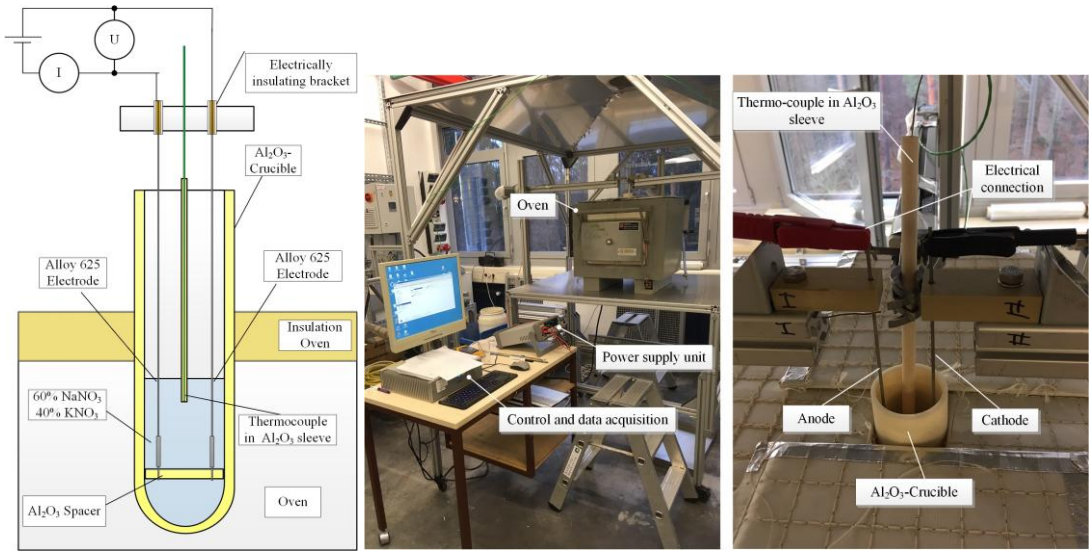


Figure C-3: Left: Schematic setup of cyclic voltammetry experiment; Right: Pictures of cyclic voltammetry experiment

The tests were conducted for two different salt temperatures (290 °C and 600 °C) and for applied peak potential differences ranging between 0.5 and 7.0 V. The triangular potential-time curve is repeated ten times for each combination of potential difference and salt temperature. Table C-4 gives an overview over the conducted test parameters. The measurements are all conducted following the procedure described in Table C-5.

| Salt temperature | Applied peak voltage | Duration of experiment | Number of cycles |
|---|---|---|---|
| 290 °C | 0.5 V | 11 min. | 10 |
| 290 °C | 1.0 V | 11 min. | 11 |
| 290 °C | 2.0 V | 12 min. | 12 |
| 290 °C | 2.7 V | 21 min. | 10 |
| 290 °C | 4.2 V | 21 min. | 10 |
| 560 °C | 0.5 V | 10 min. | 10 |
| 560 °C | 0.9 V | 10 min. | 10 |
| 560 °C | 1.4 V | 11 min. | 10 |

| Salt temperature | Applied peak voltage | Duration of experiment | Number of cycles |
|---|---|---|---|
| 560 °C | 2.1 V | 20 min. | 10 |
| 290 °C | 0.5 V | 10 min. | 10 |
| 290 °C | 2.7 V | 20 min. | 10 |
| 290 °C | 4.2 V | 20 min. | 10 |
| 290 °C | 6.1 V | 23 min. | 11 |
| 290 °C | 5.8 V | 21 min. | 10 |
| 290 °C | 7.0 V | 28 min. | 11 |
| 560 °C | 2.0 V | 20 min. | 10 |
| 560 °C | 3.2 V | 26 min. | 10 |

Table C-4: Test matrix cyclic voltammetry experiment

| Test procedure |
|---|
| Prepare electrodes, crucible and salt:<br>- Polish sample with sandpaper (first coarse then up to 1000-2000)<br>- Rinse electrode with distilled water, then with isopropanol and air dry<br>- Rinse $Al_2O_3$ crucible with distilled water and air dry<br>- Mix salt (60 wt-% $NaNO_3$, 40% $KNO_3$) at ambient temperature and fill into crucible<br>- Place crucible in oven and heat to desired temperature (290 °C, 400 °C and 560 °C)<br>- Wait until all salt has melted<br>- Immerse electrodes in salt and adjust distance between electrodes |
| Cyclic voltammetry test<br>- Increase voltage continuously from 0 to set point voltage (~ 1.5 minutes) and reduce continuously back to zero (~ 1.5 minute) (triangular function)<br>- Repeat at least 10 times |
| After test<br>- Remove and air-cool electrodes<br>- Clean electrodes with distilled water |

Table C-5: Test procedure cyclic voltammetry experiment with Solar Salt

# D. Test Setup and Test Matrix

This appendix section shows additional figures and drawings of the molten salt and water test setup as well as the carried out test matrix of each test campaign. The subchapters are divided into the so-called “Test Section” (appendix D.1), which is used in both the water test setup and the molten salt test setup. In appendix D.2 more information is given about the Solar Salt Test Setup and in appendix D.3 more details are given about the Water Test Setup.

## D.1. Test Section

The so-called Test Section is used in both the Water and the molten salt Test Setup. Figure D-1 shows a CAD drawing of the heat transfer measurement test setup with all relevant dimensions. Figure D-2 is an isometric drawing of the used solenoid induction heater coil. A screenshot of the used control system user interface of the heat transfer measurement setup can be seen in Figure D-3.

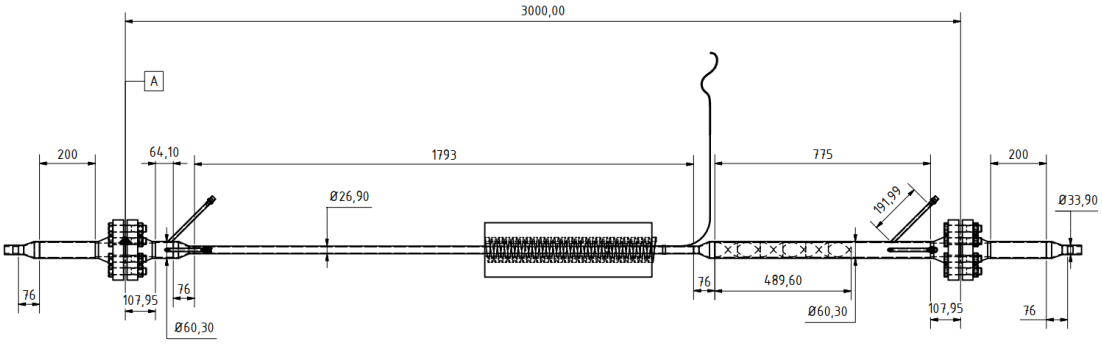


Figure D-1: CAD drawing of test section

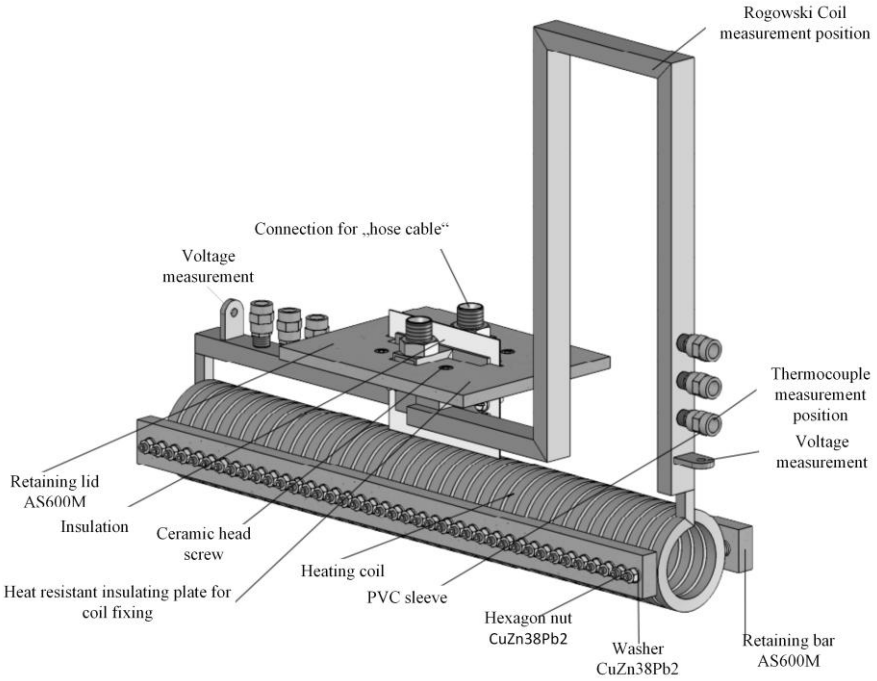


Figure D-2: Isometric view of the solenoid multiturn coil

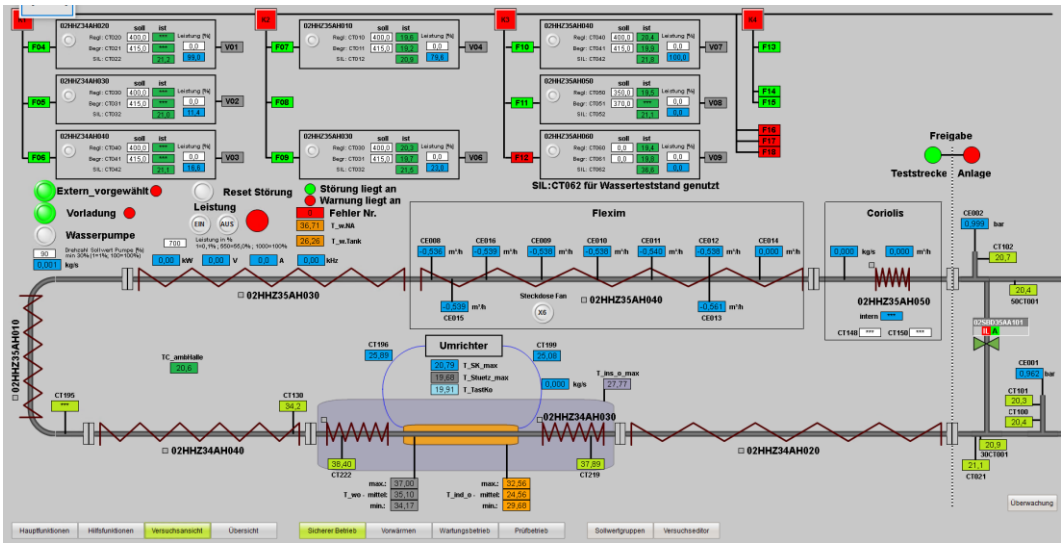


Figure D-3: Screenshot of control system molten salt Test Setup

## D.2. Solar Salt Test Setup

In this subsection additional information is given about the Solar Salt Test Setup. Figure D-4 and Figure D-5 show a schematic of the TESIS:com test section with all relevant dimensions. Figure D-6 and Figure D-7 show pictures of the heat transfer measurement setup with Solar Salt before and after insulation. Table D-8 and Table D-9 summarize the main parameters of the Solar Salt test campaign with the Smooth and the Spirally grooved tube.

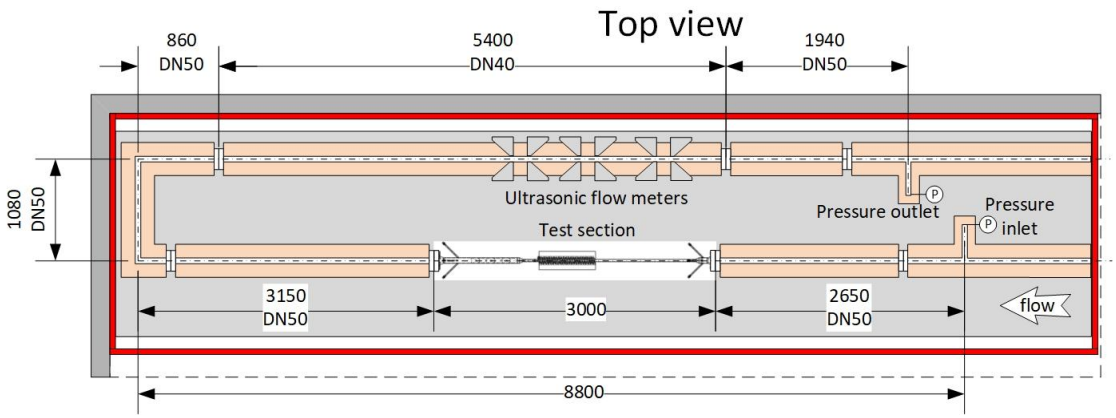


Figure D-4: Top view TESIS:com test section

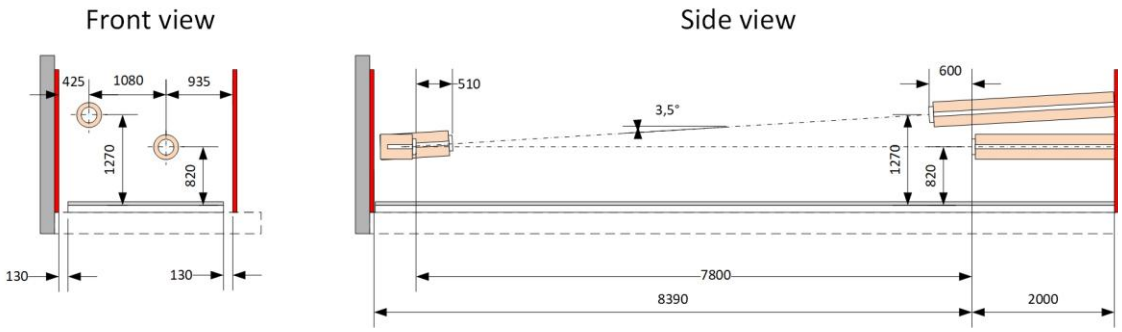


Figure D-5: Side view TESIS:com test section

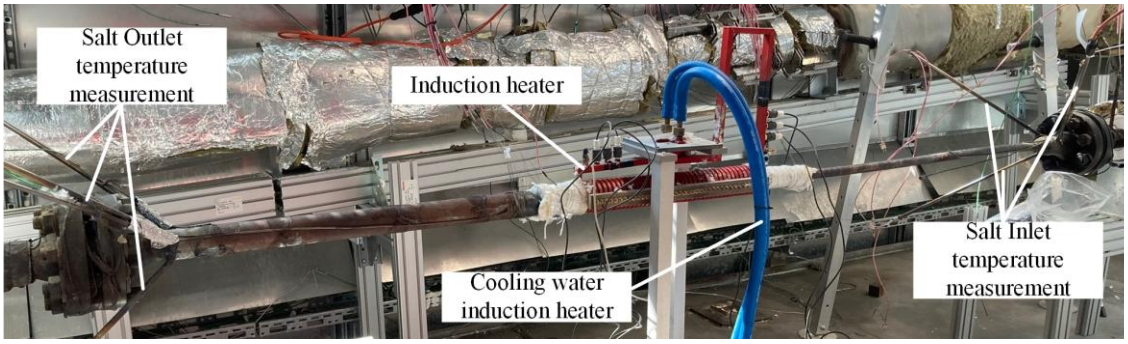


Figure D-6: Picture of molten salt Test Section during installation (before insulation)

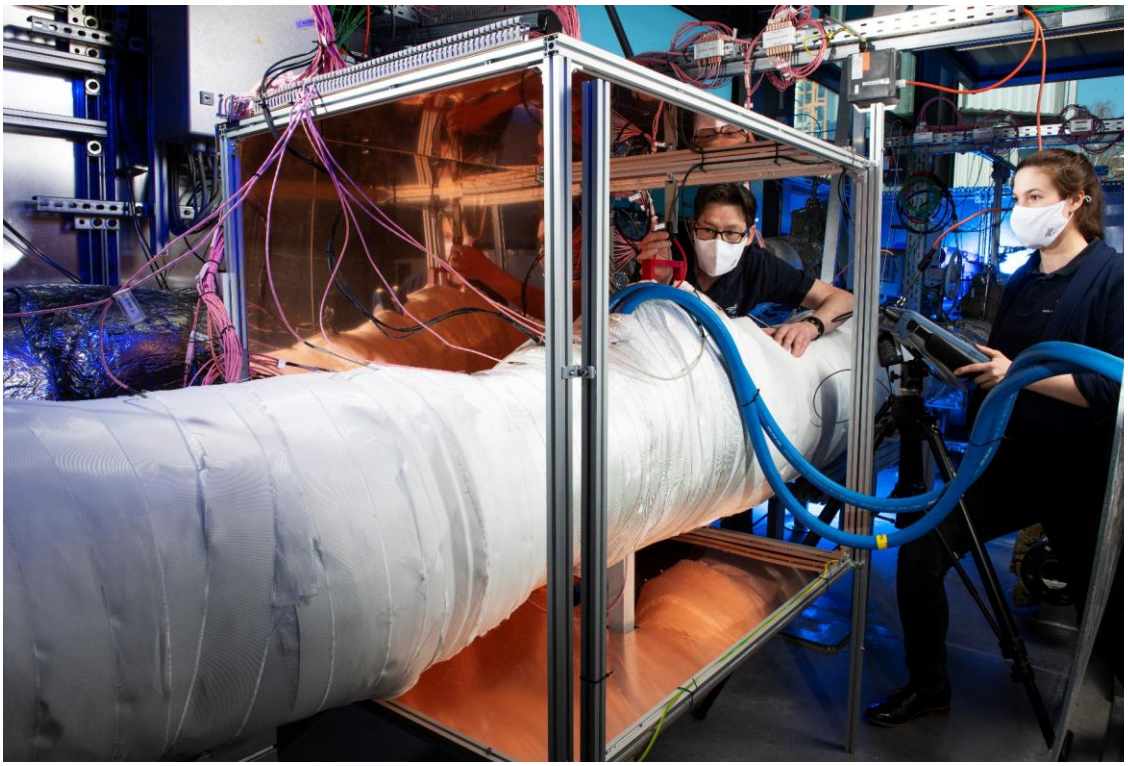

Figure D-7: Picture of molten salt Test Section after insulation

| Test identification | Main mass flow $\dot{m}_s$ (kg/s) | Main fluid temperature $T_s$ (°C) | Reynolds number (-) | Prandlt number (-) | Flux density to main fluid $\dot{q}_{th\,2\,salt}$ (kW/m²) |
|---|---|---|---|---|---|
| SALT_SM_T300_m6_q300 | 5.81 | 297.0 | 103094 | 10.0 | 330 |
| SALT_SM_T300_m5_q300 | 4.35 | 298.2 | 77685 | 9.9 | 326 |
| SALT_SM_T300_m3_q300 | 2.81 | 298.2 | 50169 | 9.9 | 325 |
| SALT_SM_T300_m1_q300 | 0.74 | 304.3 | 13720 | 9.6 | 326 |
| SALT_SM_T300_m2_q300 | 1.98 | 302.6 | 36305 | 9.7 | 325 |
| SALT_SM_T300_m6_q700 | 5.71 | 300.3 | 103448 | 9.8 | 616 |
| SALT_SM_T300_m5_q700 | 4.38 | 302.8 | 80476 | 9.7 | 614 |
| SALT_SM_T300_m3_q700 | 2.81 | 303.4 | 51901 | 9.6 | 619 |
| SALT_SM_T300_m2_q700 | 1.82 | 304.1 | 33813 | 9.6 | 619 |
| SALT_SM_T300_m1_q700 | 1.04 | 305.0 | 19326 | 9.6 | 627 |
| SALT_SM_T300_m6_q1000 | 5.73 | 299.7 | 103424 | 9.9 | 915 |
| SALT_SM_T300_m5_q1000 | 4.30 | 300.4 | 77795 | 9.8 | 912 |
| SALT_SM_T300_m3_q1000 | 2.88 | 304.3 | 53382 | 9.6 | 911 |
| SALT_SM_T300_m2_q1000 | 1.80 | 306.7 | 33968 | 9.5 | 915 |
| SALT_SM_T400_m5_q300 | 4.26 | 396.6 | 128695 | 6.2 | 393 |
| SALT_SM_T400_m3_q300 | 2.78 | 399.3 | 85017 | 6.1 | 326 |
| SALT_SM_T400_m2_q300 | 1.77 | 400.2 | 54409 | 6.1 | 326 |
| SALT_SM_T400_m1_q300 | 0.87 | 396.7 | 26267 | 6.2 | 323 |
| SALT_SM_T400_m6_q700 | 5.67 | 395.1 | 170308 | 6.2 | 616 |
| SALT_SM_T400_m5_q700 | 4.33 | 398.2 | 131805 | 6.1 | 631 |
| SALT_SM_T400_m3_q700 | 2.78 | 394.0 | 83188 | 6.2 | 629 |
| SALT_SM_T400_m2_q700 | 1.81 | 395.5 | 53777 | 6.2 | 644 |
| SALT_SM_T400_m6_q1000 | 5.66 | 399.4 | 173083 | 6.1 | 923 |
| SALT_SM_T400_m5_q1000 | 4.29 | 396.8 | 129802 | 6.2 | 921 |
| SALT_SM_T400_m1_q700 | 0.66 | 401.8 | 20559 | 6.0 | 628 |
| SALT_SM_T400_m3_q1000 | 2.89 | 401.2 | 89102 | 6.1 | 922 |

| | | | | | |
|---|---|---|---|---|---|
| SALT_SM_T400_m2_q1000 | 1.79 | 403.7 | 56020 | 6.0 | 923 |
| SALT_SM_T400_m6_q300 | 5.65 | 395.4 | 169729 | 6.2 | 329 |
| SALT_SM_T550_m3_q300 | 2.74 | 548.8 | 145643 | 3.8 | 333 |
| SALT_SM_T550_m1_q300 | 1.46 | 544.3 | 76747 | 3.8 | 333 |
| SALT_SM_T550_m2_700 | 2.13 | 544.1 | 111918 | 3.8 | 619 |
| SALT_SM_T550_m1_300 | 0.61 | 538.2 | 31362 | 3.9 | 327 |
| SALT_SM_T515_m1_300 | 0.60 | 518.9 | 29083 | 4.1 | 325 |
| SALT_SM_T475_m1_300 | 0.61 | 484.8 | 25765 | 4.5 | 324 |
| SALT_SM_T550_m5_700 | 4.20 | 547.5 | 222554 | 3.8 | 625 |
| SALT_SM_T550_m3_700 | 2.70 | 547.9 | 143069 | 3.8 | 625 |
| SALT_SM_T515_m2_700 | 2.13 | 513.3 | 101395 | 4.2 | 626 |

Table D-8: Test matrix test setup with Solar Salt and smooth tube

| **Test identification** | **Main mass flow $\dot{m}_s$ (kg/s)** | **Main fluid temperature $T_s$ (°C)** | **Reynolds number (-)** | **Prandlt number (-)** | **Flux density to main fluid $\dot{q}_{th\ 2\ salt}$ (kW/m²)** |
|---|---|---|---|---|---|
| SALT_SG_T300_m3_1000 | 2.68 | 309.7 | 51358 | 9.3 | 905 |
| SALT_SG_T300_m5_1000 | 4.18 | 307.7 | 79123 | 9.4 | 904 |
| SALT_SG_T300_m2_1000 | 1.85 | 303.8 | 34175 | 9.6 | 904 |
| SALT_SG_T300_m1_1000 | 0.70 | 315.7 | 13839 | 9.0 | 916 |
| SALT_SG_T300_m6_1000 | 5.51 | 299.6 | 99411 | 9.9 | 890 |
| SALT_SG_T300_m6_700 | 5.49 | 302.4 | 100644 | 9.7 | 615 |
| SALT_SG_T300_m5_700 | 4.22 | 299.2 | 75928 | 9.9 | 615 |
| SALT_SG_T300_m3_700 | 2.62 | 304.2 | 48667 | 9.6 | 616 |
| SALT_SG_T300_m2_700 | 2.08 | 302.4 | 38194 | 9.7 | 617 |
| SALT_SG_T300_m1_700 | 0.64 | 312.7 | 12500 | 9.2 | 614 |
| SALT_SG_T300_m6_300 | 5.58 | 298.4 | 99835 | 9.9 | 320 |
| SALT_SG_T300_m5_300 | 4.06 | 303.5 | 74943 | 9.6 | 321 |
| SALT_SG_T300_m3_300 | 2.71 | 301.9 | 49601 | 9.7 | 321 |
| SALT_SG_T300_m2_q300 | 2.02 | 300.8 | 36765 | 9.8 | 321 |
| SALT_SG_T300_m1_q300 | 0.64 | 306.4 | 12052 | 9.5 | 321 |

| | | | | | |
|---|---|---|---|---|---|
| SALT_SG_T300_m1_q1000b | 0.68 | 315.5 | 13402 | 9.0 | 911 |
| SALT_SG_T300_m3_q1000b | 2.77 | 302.1 | 50707 | 9.7 | 896 |
| SALT_SG_T300_m6_q1000b | 5.33 | 301.8 | 97342 | 9.7 | 892 |
| SALT_SG_T300_m1_q1000c | 0.84 | 318.4 | 16975 | 8.9 | 933 |
| SALT_SG_T300_m3_q1000c | 2.72 | 305.8 | 50895 | 9.5 | 918 |
| SALT_SG_T300_m6_q1000c | 5.59 | 322.3 | 115379 | 8.7 | 915 |
| SALT_SG_T300_m5_q1000c | 4.20 | 318.8 | 85075 | 8.9 | 917 |
| SALT_SG_T300_m2_q1000c | 1.98 | 324.9 | 41543 | 8.6 | 921 |
| SALT_SG_T300_m1_q700c | 0.62 | 309.7 | 11717 | 9.3 | 629 |
| SALT_SG_T300_m3_q700c | 2.67 | 310.2 | 51317 | 9.3 | 619 |
| SALT_SG_T300_m6_q700c | 5.54 | 303.3 | 102257 | 9.7 | 616 |
| SALT_SG_T300_m5_q700c | 4.14 | 307.3 | 78314 | 9.4 | 617 |
| SALT_SG_T300_m2_q700c | 2.08 | 307.2 | 39371 | 9.4 | 618 |
| SALT_SG_T300_m1_q300c | 0.56 | 316.0 | 10329 | 9.0 | 332 |
| SALT_SG_T300_m3_q300c | 2.67 | 308.6 | 50854 | 9.4 | 328 |
| SALT_SG_T300_m4_q300c | 3.30 | 304.0 | 61144 | 9.6 | 327 |
| SALT_SG_T300_m2_q300c | 1.45 | 313.8 | 28559 | 9.1 | 328 |
| SALT_SG_T300_m5_q300c | 4.17 | 306.8 | 78512 | 9.5 | 327 |
| SALT_SG_T400_m6_q300 | 5.39 | 400.1 | 165652 | 6.1 | 330 |
| SALT_SG_T400_m6_q300b | 5.41 | 399.9 | 165930 | 6.1 | 325 |
| SALT_SG_T400_m5_q300b | 4.17 | 396.0 | 125712 | 6.2 | 325 |
| SALT_SG_T400_m3_q300b | 2.68 | 399.1 | 82068 | 6.1 | 325 |
| SALT_SG_T400_m6_q1000 | 5.54 | 397.8 | 168347 | 6.1 | 915 |
| SALT_SG_T400_m5_q1000 | 3.85 | 399.4 | 117916 | 6.1 | 913 |
| SALT_SG_T400_m3_q1000 | 2.53 | 400.3 | 77696 | 6.1 | 913 |
| SALT_SG_T400_m2_q1000a | 1.79 | 398.4 | 54557 | 6.1 | 922 |
| SALT_SG_T400_m1_q700b | 0.63 | 402.1 | 19602 | 6.0 | 625 |
| SALT_SG_T400_m3_q700b | 2.68 | 397.1 | 81082 | 6.2 | 618 |
| SALT_SG_T400_m3_q1000b | 2.74 | 397.6 | 83178 | 6.1 | 918 |
| SALT_SG_T400_m6_q1000b | 5.39 | 397.1 | 163325 | 6.2 | 915 |
| SALT_SG_T400_m2_q1000b | 1.57 | 400.9 | 48306 | 6.1 | 921 |
| SALT_SG_T400_m5_q1000b | 4.15 | 397.5 | 125850 | 6.1 | 915 |

| | | | | | |
|---|---|---|---|---|---|
| SALT_SG_T400_m1_q1000b | 0.87 | 410.6 | 27921 | 5.8 | 937 |
| SALT_SG_T400_m1_q700c | 0.63 | 406.2 | 19846 | 5.9 | 630 |
| SALT_SG_T400_m3_q700c | 2.66 | 400.9 | 81891 | 6.1 | 623 |
| SALT_SG_T400_m6_q700c | 5.47 | 398.0 | 166370 | 6.1 | 623 |
| SALT_SG_T400_m2_q700c | 1.87 | 401.2 | 57710 | 6.1 | 623 |
| SALT_SG_T400_m5_q700c | 4.04 | 397.7 | 122700 | 6.1 | 622 |
| SALT_SG_T400_m2_q1000c | 1.92 | 400.3 | 58939 | 6.1 | 928 |
| SALT_SG_T400_m3_q1000c | 2.66 | 400.7 | 81800 | 6.1 | 927 |
| SALT_SG_T400_m6_q1000c | 5.50 | 398.6 | 167696 | 6.1 | 922 |
| SALT_SG_T550_m3_q700 | 2.52 | 548.1 | 133576 | 3.8 | 635 |
| SALT_SG_T550_m1_q700 | 1.42 | 544.9 | 74500 | 3.8 | 636 |
| SALT_SG_T550_m1_q700b | 1.32 | 546.5 | 69532 | 3.8 | 634 |
| SALT_SG_T550_m6_q700 | 5.09 | 550.2 | 271794 | 3.8 | 637 |
| SALT_SG_T550_m1_q700c | 1.35 | 553.4 | 72785 | 3.8 | 638 |
| SALT_SG_T550_m6_q1000 | 5.17 | 547.8 | 273998 | 3.8 | 939 |
| SALT_SG_T550_m1_q300 | 0.71 | 547.2 | 37645 | 3.8 | 338 |
| SALT_SG_T550_m6_q300 | 5.22 | 551.2 | 279698 | 3.8 | 337 |
| SALT_SG_T550_m3_q300 | 2.57 | 552.1 | 138137 | 3.8 | 338 |
| SALT_SG_T550_m5_q700 | 4.03 | 551.4 | 215894 | 3.8 | 634 |
| SALT_SG_T550_m1_q700d | 1.48 | 557.1 | 80420 | 3.7 | 634 |
| SALT_SG_T550_m6_q700d | 5.27 | 553.7 | 284656 | 3.7 | 630 |
| SALT_SG_T550_m4_q700d | 3.94 | 555.0 | 213360 | 3.7 | 629 |

Table D-9: Test matrix test setup with Solar Salt and spirally grooved tube

## D.3. Water Test Setup

This section includes additional information about the Water Test Setup. Figure D-10, Figure D-11 and Figure D-12 show a simplified piping and instrumentation diagram, 3D CAD drawing and a picture of the final installation of the water test setup respectively. Table D-13 gives an overview over the main parameters during the water test campaign.

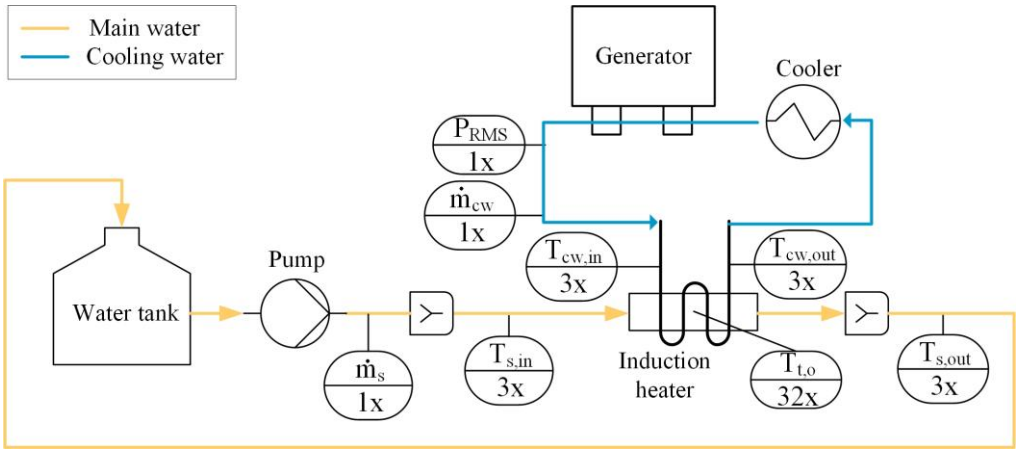


Figure D-10: Simplified piping and instrumentation diagram of water test setup

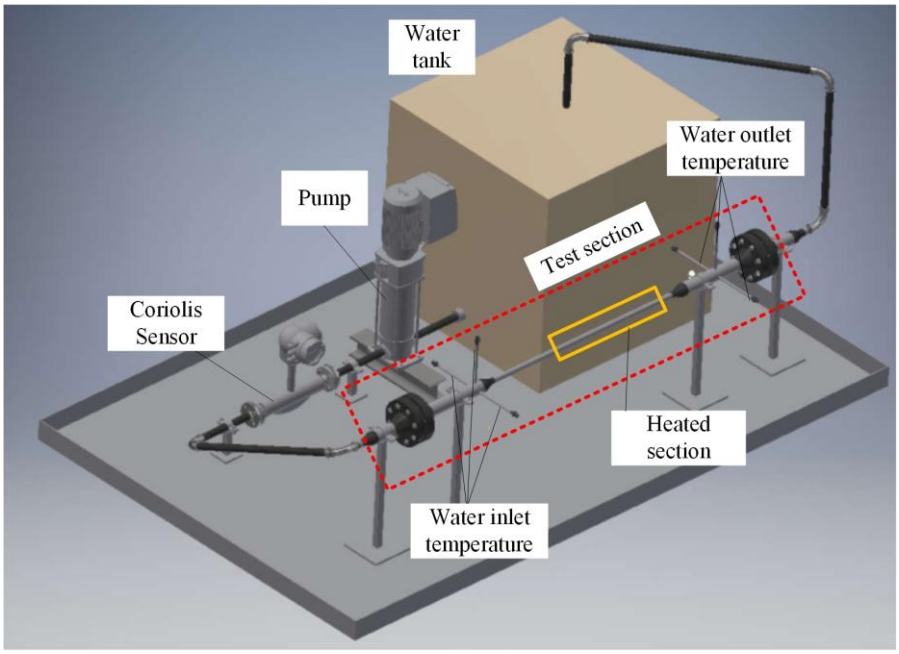


Figure D-11: CAD drawing of water test setup

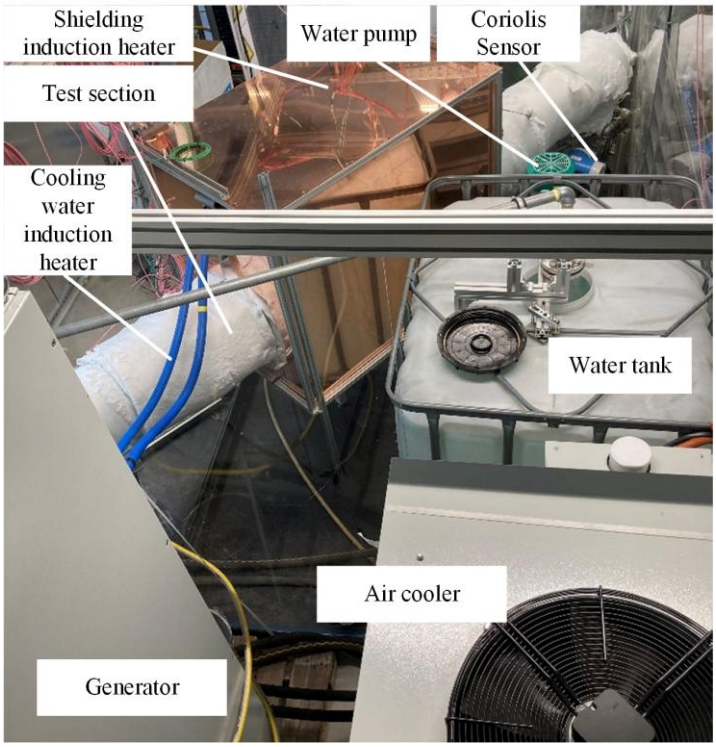


Figure D-12: Picture of water test setup

| Test identification | Main mass flow $\dot{m}_s$ (kg/s) | Main fluid temperature $T_s$ (°C) | Reynolds number (-) | Prandlt number (-) | Flux density to main fluid $\dot{q}_{th\,2\,water}$ (kW/m²) |
|---|---|---|---|---|---|
| WAT_m1_q700 | 0.94 | 14.4 | 45347 | 8.3 | 651 |
| WAT_m2_q700 | 1.82 | 22.5 | 106143 | 6.6 | 649 |
| WAT_m3_q700 | 3.18 | 31.6 | 227041 | 5.2 | 649 |
| WAT_m1_q600 | 0.95 | 13.2 | 43608 | 8.5 | 548 |
| WAT_m2_q600 | 1.83 | 20.1 | 100616 | 7.0 | 547 |
| WAT_m3_q600 | 3.18 | 28.1 | 210442 | 5.7 | 547 |
| WAT_m1_q460 | 0.96 | 35.5 | 75116 | 4.8 | 411 |
| WAT_m2_q460 | 1.84 | 40.9 | 158843 | 4.2 | 411 |
| WAT_m3_q460 | 3.18 | 46.9 | 305237 | 3.8 | 410 |
| WAT_m1_q900 | 0.95 | 16.2 | 47373 | 7.8 | 820 |
| WAT_m1_q1000 | 1.27 | 25.1 | 77849 | 6.1 | 955 |
| WAT_m2_q1000 | 2.52 | 32.7 | 182627 | 5.1 | 953 |
| WAT_m3_q1000 | 3.18 | 41.8 | 275872 | 4.2 | 954 |

Table D-13: Test matrix validation tests with water and smooth tube

# E. Enhanced tube geometry

This appendix chapter gives additional information about the selection process of the spirally grooved tube geometry and the final geometry of the selected spirally grooved tube.

The geometry of the enhanced grooved tube is defined based on the following two criteria:

- Expected increase in Nusselt number of more than 20 %
- Expected increase in pressure difference of maximum 200%
- Manufacturability

Using the correlations introduced by Ravigururajan et al. [62] the expected increase in Nusselt number and pressure difference is computed for different groove heights *e*, groove angles *α* and number of threads *G*. Figure 0-1 shows on the left two exemplary grooved tubes with two different number of threads. Table 0-2 summarizes the evaluated tube enhanced tube geometries. Figure 0-3 shows the Nusselt number ratio and friction factor ratio for the different enhanced tube geometries. In general, it can be observed that both the Nusselt number ratio and the friction factor ratio increase for higher groove heights and for lower groove pitch (e.g., higher number of threads). Both ratios are highest for transversely grooved tubes ($\alpha$=90°) and decrease for lower groove angles. However, it occurs that the friction factor ratios achieve values above a factor of two already for relatively low groove heights. The variant with one thread, a groove angle of 73.7° and a groove height of 0.4 mm is selected together with the manufacturer. This variant promises a Nusselt number ratio of more than 1.5 at a friction factor ratio of roughly 2.0.

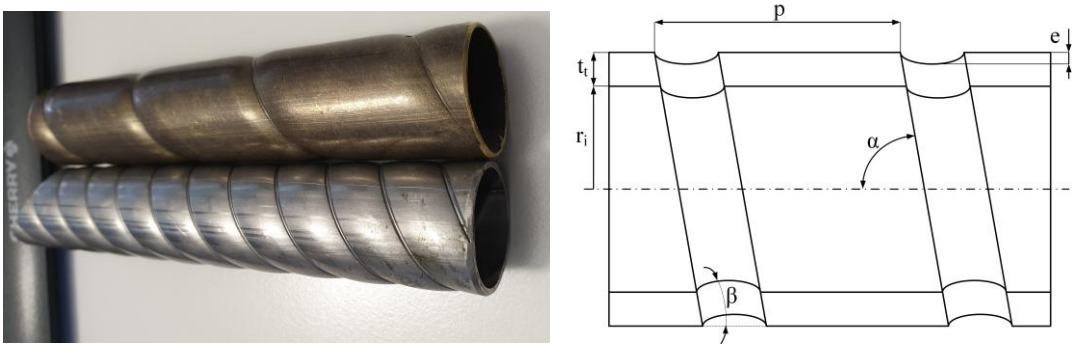


Figure 0-1: Left: Exemplary spirally grooved tubes with one thread (top) and three threads (bottom); Right: Geometry definition of spirally grooved tube

| Geometry identification | Inner tube diameter (mm) | Groove heigth (mm) | Number of threads (-) | Groove angle (°) | Pitch length (mm) |
|---|---|---|---|---|---|
| p = 5 mm; α=90° | 22.9 mm | *e*: 0.25 mm | / | 90 | 5 |
| p = 10 mm; α=90° | | | / | 90 | 10 |
| p = 15 mm; α=90° | | 0.5 mm | / | 90 | 15 |

| | | | | | |
|---|---|---|---|---|---|
| G=1; α=60° | | 0.75 mm | 1 | 60 | 41.5 |
| G=2; α=60° | | 1.0 mm | 2 | 60 | 20.8 |
| G=3; α=60° | | 2.0 mm | 3 | 60 | 13.8 |
| G=1; α=30° | | | 1 | 30 | 124.6 |
| G=2; α=30° | | | 2 | 30 | 62.3 |
| G=3; α=30° | | | 3 | 30 | 41.5 |
| G=3; α=49° | | | 3 | 49.0 | 20.8 |
| G=1; α=73,7° | | | 1 | 73.7 | 21.0 |

Table 0-2: Evaluated enhanced tube geometries

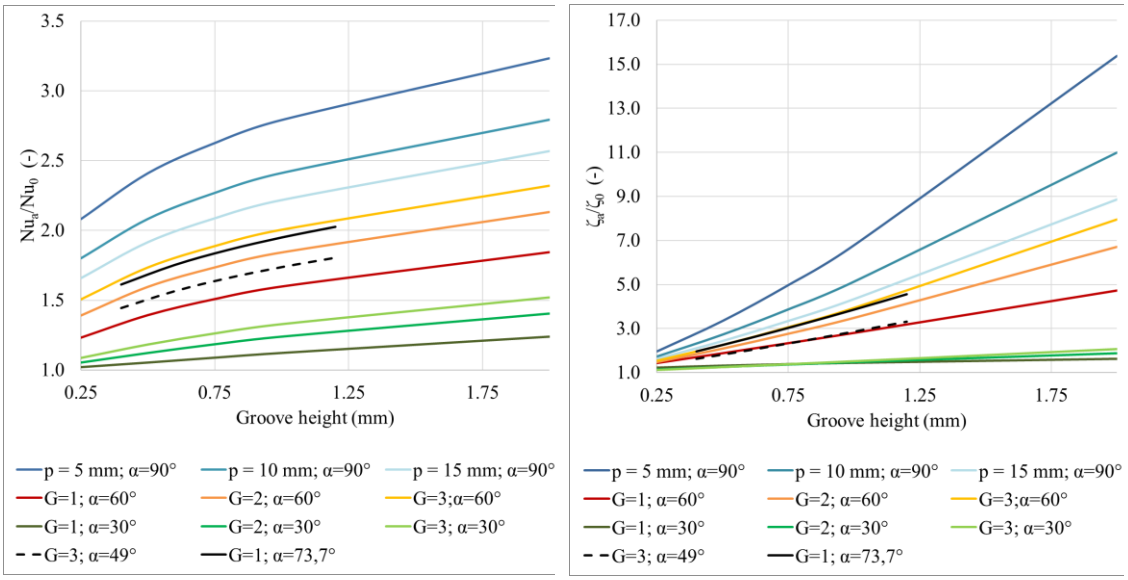


Figure 0-3: Nusselt number ratio (left) and friction factor ratio (right) calculated for different enhanced tube geometries using the general correlations by Ravigururajan

Before mounting the spirally grooved tube in the test setup and attaching the outer wall thermocouples the tube dimensions are controlled. Figure 0-4 shows the results of the measured surface geometry over an axial length of 100 mm. Based on the position of the minima, the tube geometry factors are deduced (see table on the right). The final mean groove pitch, groove height and groove angle are deduced by calculating the mean average and can be found in Table 4-2 in chapter 4.2.

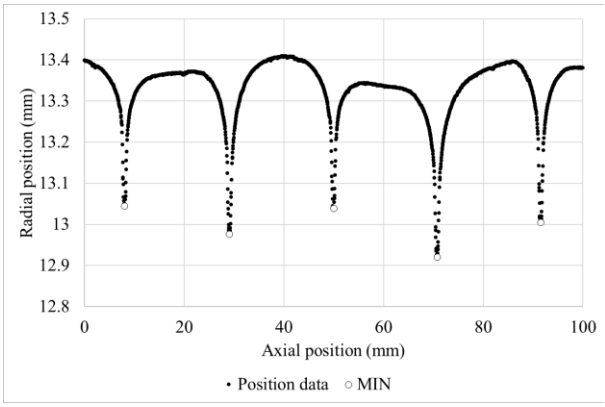


| Position | Groove pitch p (mm) | Groove height e (mm) | Grove angle α (°) |
|---|---|---|---|
| MIN 1 | | 0.36 | |
| MIN 2 | 21.1 | 0.42 | 73.6 |
| MIN 3 | 20.9 | 0.36 | 73.8 |
| MIN 4 | 20.8 | 0.48 | 73.8 |
| MIN 5 | 20.8 | 0.40 | 73.8 |

Figure 0-4: Measured surface geometry of spirally grooved tube (left) and deduced geometry factors

# F. Measurement equipment and uncertainty

This appendix chapter gives additional information about the taken assumptions for the uncertainty analysis of the outer wall tube temperature, main molten salt mass flow and of the phase angle.

## F.1. Assumptions for Uncertainty of Outer Wall Tube Temperature $T_{t,o}$

In the smooth tube, there are two main types of tube surface temperature measurement.

- Thermocouple connected by laser welding
- Thermocouple connected by spot weld

In the spirally grooved tube setup, all outer wall thermocouples were fixed by laser welding.

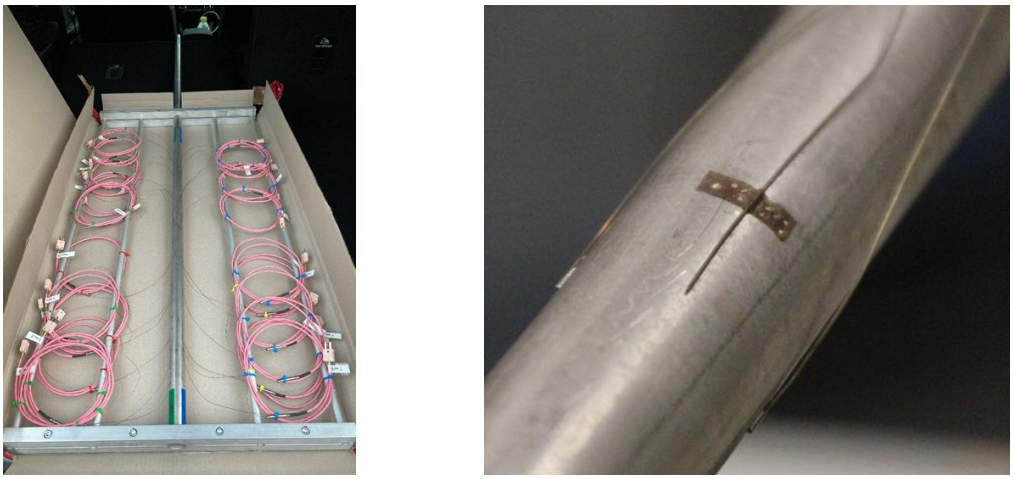

Figure F-1: Left: Test tube before mounting; Right: Close-up of outer wall thermocouples with one spot welded thermocouple at the center of the image and two laser welded thermocouples at the sides of the tube

The overall measurement uncertainty of the outer tube wall temperature $\sigma_{T_{t,o}}$ is defined as follows:

$$\sigma_{T_{t,o}}^2 = \left( \underbrace{\sqrt{\sigma_{T_{t,o},weld}^2 + \sigma_{T_{t,o},calibration}^2 + \sigma_{T_{t,o},x}^2 + \sigma_{T_{wo,\lambda(T)}}^2}}_{measurement\ equipment\ uncert.} \right)^2 + \underbrace{\sigma_{T_{t,o},read}^2}_{measurement\ reading\ uncert.}$$

Where $\sigma_{T_{t,o},weld}$ is the uncertainty caused by applying a laser weld on the thermocouple, $\sigma_{T_{wo},calibration}$ is the uncertainty of temperature sensor equipment after calibration and is assumed to be $= \pm 0.06$ K. $\sigma_{T_{t,o},x}$ is the standard deviation between the temperature readings of the four thermocouples at the same axial location and $\sigma_{T_{wo,\lambda(T)}}$ is the uncertainty of the temperature-dependence of the thermal conductivity of the tube. $\sigma_{T_{t,o},read}$ is the measurement reading uncertainty, which is deduced using the standard deviation of the measurement data over a time interval of 10 s.

The impact of applying a laser weld on the thermocouples $\sigma_{T_{t,o},weld}$ is evaluated by applying a laser weld onto two test thermocouples with the same welding boundary conditions as have been used later on for welding the thermocouples to the tube. The heat-affected zone of the laser weld has been specified with 0.05 mm by the manufacturer and lies therefore one order of magnitude below the diameter of the thermocouple (0.5 mm). The two thermocouples have been calibrated using the AMETEK calibrator once before and once after applying the laser weld. Figure F-2 (right) shows the measured standard deviation of the two thermocouples before and after application of the weld. It can be seen that for both sensors a similar or lower standard deviation was measured after applying the weld. This confirms that the welding process did not impact the measurement quality of the sensor.

Figure F-2 (left) shows the absolute deviation of the sensor readings before and after application of the weld. For temperatures below 100 °C, $\sigma_{T_{t,o},weld}$=+0,15 K is assumed, for temperatures below 500 °C $\sigma_{T_{t,o},weld}$=+1 K is assumed.

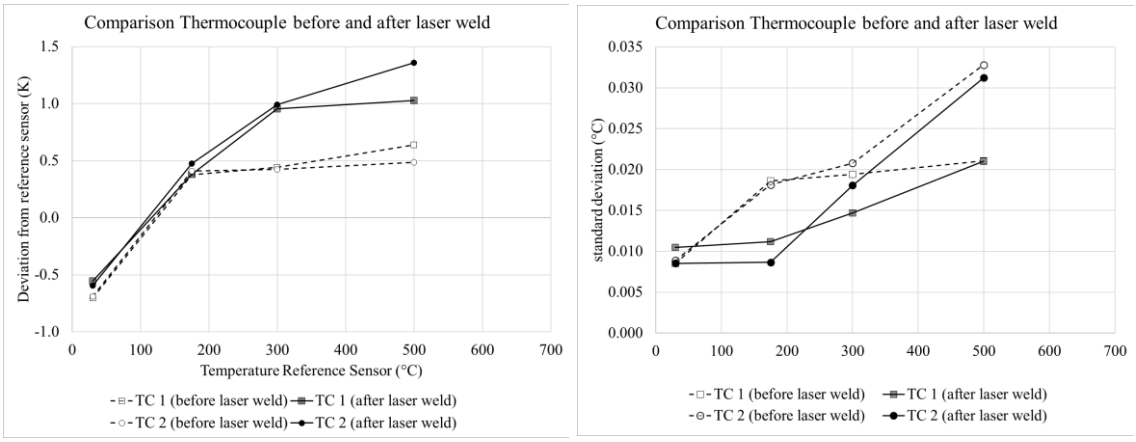


Figure F-2: Comparison of thermocouple before and after application of laser weld

The impact on measurement uncertainty of the temperature-dependence of the thermal conductivity of the tube $\sigma_{T_{wo,\lambda(T)}}$ is quantified using an FEM simulation of a tube slice. The simulations were performed assuming a mass flow of 1 kg/s and 900 kW/m² for both the water test setup and the salt setup at 290°C. It is assumed that the effect is reduced for higher thermal conductivities of the tube and lower flux densities. The results of the FEM simulation are compared to the four cases:

1. Constant thermal conductivity of $\lambda_t$=20 W/(m K)
2. Radially constant thermal conductivity computed using the measured outer tube temperature $T_{t,o}$: $\lambda_t=f(T_{t,o})$
3. Radially constant thermal conductivity computed using the mean of the measured outer tube temperature $T_{t,o}$ and the resulting tube film temperature $T_{t,i}$: $\lambda_t =f((T_{t,o} + T_{t,i})/2)$
4. Ideal assumption: Thermal conductivity as a function of local radial tube temperature $\lambda_t=f(T_t)$

Figure F-3 (left) shows exemplary resulting radial temperature profiles for a constant applied heating flux density and convective cooling rate. Figure F-3 (right) shows the resulting deviation for all resulting outer wall temperatures and the reference case with a locally temperature dependent thermal conductivity. It can be seen that the lowest deviations are found when assuming $\lambda_t = f((T_{t,o} + T_{t,i})/2)$ for which a maximum deviation of wall temperature of ±0.18 K is found. This will be accounted for as a general uncertainty:

$$\sigma_{T_{wo,\lambda(T)}} = \frac{\pm 0.18\ \mathrm{K}}{\sqrt{3}} = 0.1\ \mathrm{K}$$

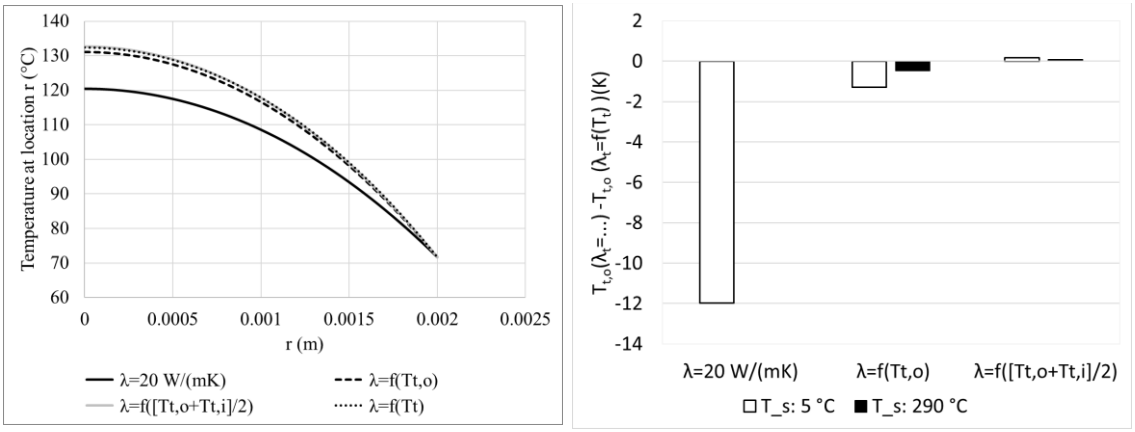


Figure F-3: Left: Exemplary radial temperature profiles for a constant applied heating flux density and convective cooling rate for all four heat conductivity assumptions; Right: Deviation of expected outer wall temperature at different heat conductivity assumptions from ideal assumptions

## F.2. Assumptions for Uncertainty of Main Fluid Mass Flow in Salt Setup

The clamp-on ultrasonic flow meters deduce the mean flow velocity of the salt in the tube based on the transit time of an ultrasonic signal in the tube. The measured output of the sensors is the volumetric flow rate, which is calculated with the tube diameter. The bulk salt mass flow is hence defined as: $\dot{m}_{s,UFM} = \dot{V}_{s,UFM} \cdot \rho(T_s)$. It is found that these sensors give good qualitative measurements but show an offset from the reference measurement. This offset suffers from poor repeatability from one measurement day to another.

The mean mass flow is deduced from the level measurement using the following correlation:

$$\dot{m}_{s,RADAR} = \frac{1}{\Delta t}\int_t^{t+\Delta t} \frac{\partial m(t)}{\partial t}\,\mathrm{d}t = \frac{1}{\Delta t}\int_t^{t+\Delta t} \frac{\partial\left(V_t(t)\cdot\rho\left(\bar{T}_{s,tank}\right)\right)}{\partial t}\,\mathrm{d}t$$

Where $V_t(t)$ is the fluid volume in the salt tank at time t and $\rho(\bar{T}_{s,tank})$ is the salt density at the bulk salt tank temperature of all salt tank temperature sensors immersed in the salt tank. It is found that using the radar level sensors for mean mass flow measurement leads to a more reliable mean mass flow measurement than using the clamp-on sensors.

The deduction of mass flow based on the level measurement in the hot and cold salt tank is influenced by the following factors:

- Correlation between salt tank level and volume
- Impact of tank deformation at high temperature
- Impact of salt density

The correlation between tank volume and level measurement has been evaluated empirically[VII]: for this purpose, each of the tanks was filled with water at ~4°C. The water volume in the tank was simultaneously measured by the radar level sensors and a Proline Promass 83F Coriolis Sensor by Endress+Hauser. In a final step, a correlation of the type $V_t = f(H_{tank})$ was deduced based on a 10th order polynomial. The fit exposed a maximum deviation from the measurement data of ±40 liters. To evaluate the impact of higher temperature operation on the level measurement, a coupled thermal and structural FEM simulation of the storage tank, salt content and insulation was performed[VII]. The salt tank geometry at 300 °C and 560 °C is simulated for three different salt levels and the relative displacement of the level measurement is deduced. The main observed effects are:

- Bending of the salt tank caused by the weight of the tank, insulation and salt and temperature-dependent steel properties leading on the one hand to a reduction of distance between level sensor and salt and on the other hand an increase of distance between salt and level sensor
- Thermal expansion of the metallic components of the salt tank

Figure F-5 shows the correction factor for the temperature and salt level dependent deformation of the salt tank $\Delta H_{tank}$. The deviation increases with higher temperatures and with lower salt level. This is caused by the overlap of two main effects: a higher temperature leads to thermal expansion of the tank; therefore the radar level sensor is moved further away from the salt level, compared to the water tests. This effect is higher for higher temperatures. As salt levels increase, the salt tank bends under the salt load: this leads to a lower measured salt level, because of the stronger bending of bottom half of the tank. At the same time, the level sensor is also moved towards the salt level. Finally, this leads to the following correction equation:

$$H_{tank,corr} = H_{tank,meas} + \Delta H_{tank}(\overline{T}_{s,tank}, H_{tank,meas})$$

Where $H_{tank,meas}$ is the measured fluid level in the tank and $\Delta H_{tank}$ is a correction for the temperature and salt level dependent deformation of the salt tank.

[VII] The author would like to express her sincere thanks to Dr. Odenthal and his team for providing the corrrelation.

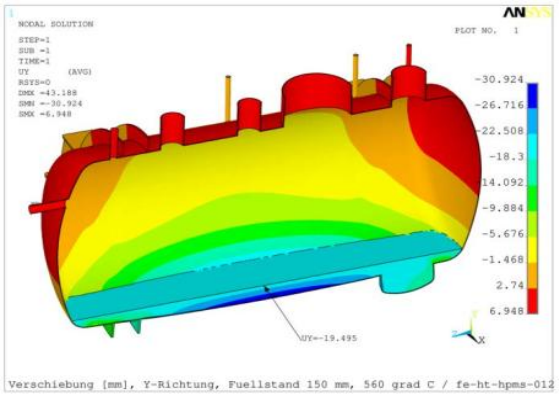


Figure F-4: Exemplary result of FEM analysis of tank deformation (150 mm salt level, 560°C salt temperature)

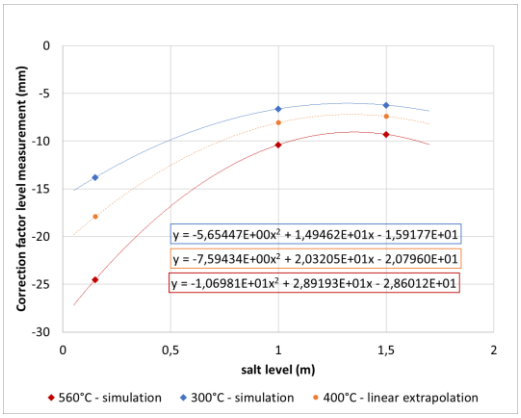


Figure F-5: Correction factors curves and correlations for salt level measurement

In order to minimize the impact of salt level scattering due to salt movement in the tank, a second order polynomial is fitted to the measured mass in the salt tank over the selected measurement interval and an average mass flow over the measurement interval is computed. Figure F-6 shows the expected relative uncertainty of the mean mass flow measurement using the radar level sensors. For this calculation, a conservative measurement uncertainty of 20 mm of the salt level (the manufacturer specifies < 2 mm), the uncertainty of the salt density (see chapter 3.5) as well as the uncertainty of the correlation linking volume of salt to measured height ($V_t = f(H_{tank})$; ±40 l) are assumed. The main influence factor on the relative uncertainty is the measured height difference in the salt tank. The resulting correlation from Figure F-6 is assumed as an uncertainty for the mean mass flow measurement of the radar level sensors.

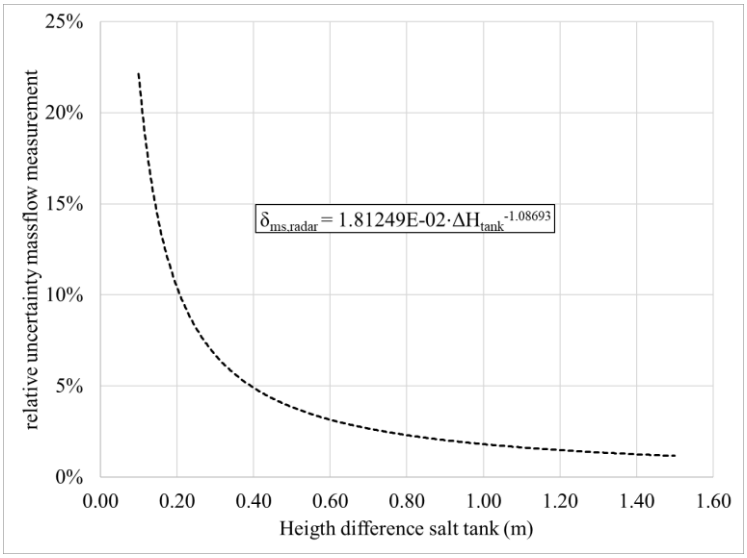


Figure F-6: Relative uncertainty of mean mass flow measurement using the radar level sensors as a function of measured height difference in the salt tank

Figure F-7 shows the results of a validation measurement campaign using a high temperature Coriolis sensor of the type OPTIMASS 6400 by the company KROHNE. It can be observed that

the mean measured mass flow by both methods agrees within ±2.5%. The measured height difference in the tank range between 0.3 and 1.1 meters. It can be concluded that the mean mass flow measurement method using the radar level sensors is well-suited and that the assumed relative uncertainty discussed above is conservative.

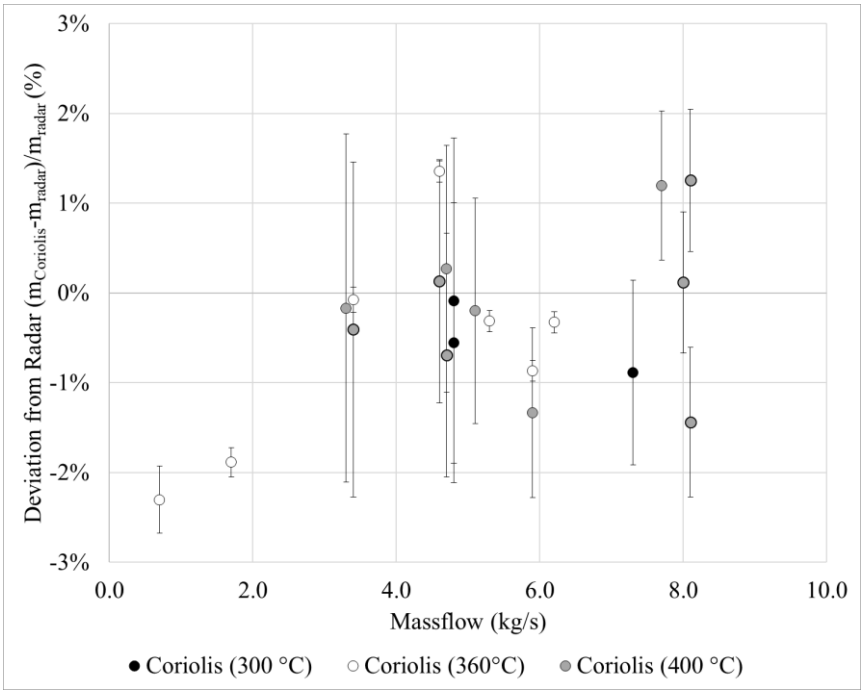


Figure F-7: Validation of mean mass flow measurement using radar level sensors with high temperature Coriolis sensor

Figure F-8 shows an exemplary measurement of the measured mass flow with the Coriolis sensor, mean mass flow using the radar level sensors and all three ultrasonic flow meters at 360 °C at a mass flow of roughly 3.3 kg/s. Good qualitative agreement is found between the mass flow of the Coriolis sensor and the ultrasonic flow meters. At the same time, the ultrasonic flow meters show an offset relative to the Coriolis mass flow. This offset suffers from relatively low repeatability, especially at low mass flow rates. Figure F-8 (right) shows an exemplary measurement of the ultrasonic flowmeters and the outer wall temperature during a heat transfer experiment. It can be seen that for roughly a second the mass flow is reduced, simultaneously the outer wall temperature increase. Both examples show that the ultrasonic flow meters are well-fitted to measure the mass flow in the test section qualitatively. The final salt mass flow consists of the mean average of all three ultrasonic flow meters, calibrated for each measurement interval by the measured mean mass flow deduced from the radar level sensors.

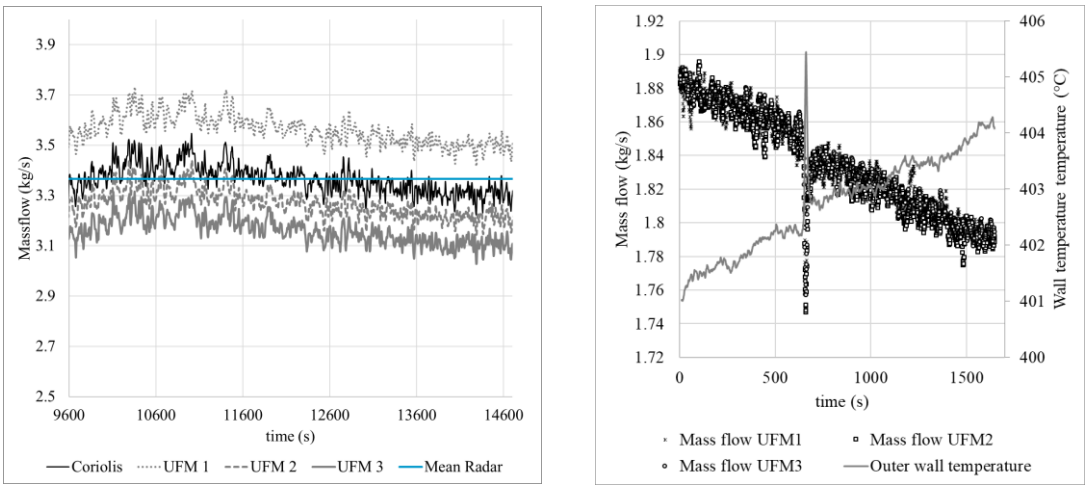


Figure F-8: Exemplary mass flow measurements showing the qualitative measurement of the ultrasonic mass flow sensors

## F.3. Assumptions for Uncertainty of Phase Angle φ

The phase angle is deduced based on equation (4.17). The phase angle is a function of the resistance and reactance of the coil-workpiece system. Both the resistance and reactance of the coil and workpiece are a function of the penetration depth δ, and – in the case of a constant frequency – therefore of the coil and tube temperatures (see equation (2.19)) [24]. The measurements of the phase angle performed by the oscilloscope show that the impact of the coil temperature is inferior ($\sigma < 0.02°$). This is because the temperature of the coil is maintained through the cooling water flow through the induction heater. Hence, the phase angle is expected to mainly depend on the tube temperature. The phase angle is deduced from calorimetric measurements showing a low uncertainty and will be assumed constant for the water and the salt setup respectively. The uncertainty of each phase angle is calculated using the method of error propagation $\sigma_{y(x_1,x_2\ldots x_n)} \equiv \sqrt{\left(\frac{\partial y}{\partial x_1}\right)^2 \cdot \sigma_{x_1}^2 + \cdots + \left(\frac{\partial y}{\partial x_n}\right)^2 \cdot \sigma_{x_n}^2}$. Figure F-9 shows the resulting phase angle as a function of tube wall temperature: the black circles represent the phase angles deduced for the water setup with an uncertainty lower 0.3° and a minimum temperature gradient in the main fluid of at least 5 K, the white circles are the phase angles deduced for the salt setup ($\Delta T_s$>5 K; $\sigma_\varphi$<0.3°). All other measured phase angles are included for reference (black cross). A linear increasing trend with temperature could be derived from Figure F-9. However, as the individual measurements show considerable scattering, a constant phase angle is assumed for the water test and the salt test respectively and a conservative uncertainty is assumed instead.

The mean phase angle $\bar{\varphi}$ is computed as the mean average of all measurements of the salt and water setup exposing an uncertainty lower 0.3° and a minimum temperature difference in the main fluid of at least 5 K respectively. The mean phase angle uncertainty $\sigma_{\bar{\varphi},m}$ consists of the combined measurement uncertainty of the mean phase angle based on the calorimetric measurements $\sigma_{\bar{\varphi},m}$, the measurement reading uncertainty $\sigma_{\varphi,read}$ and the uncertainty for not accounting for a systematic dependency on tube temperature $\sigma_{\bar{\varphi},temperature}$.

$$\sigma_{\bar{\varphi}} = \sqrt{\sigma_{\bar{\varphi},m}^2 + \sigma_{\varphi,read}^2 + \sigma_{\bar{\varphi},temperature}^2}$$

The mean phase angle uncertainty based on calorimetric measurements is defined as follows:

$$\sigma_{\bar{\varphi},m} = \sqrt{\left(\frac{\partial \sigma_{\bar{\varphi}}}{\partial \sigma_{\varphi_1}}\right)^2 \sigma_{\varphi_1}^2 + \left(\frac{\partial \sigma_{\bar{\varphi}}}{\partial \sigma_{\varphi_2}}\right)^2 \sigma_{\varphi_2}^2 + \cdots + \left(\frac{\partial \sigma_{\bar{\varphi}}}{\partial \sigma_{\varphi_n}}\right)^2 \sigma_{\varphi_n}^2}$$

where $\sigma_{\varphi_x}$ is the uncertainty of each calculated measurement interval and $n$ is the number of considered measurement intervals. The measurement reading uncertainty is defined as the maximum deviation observed by the oscilloscope during one measurement interval $\sigma_{\varphi,read} = \Delta\varphi_{MAX}/\sqrt{3}$. The systematic uncertainty due to temperature effects $\sigma_{\bar{\varphi},temperature}$ is defined as the difference between the maximum and minimum measured phase angle over all measurement intervals of the water test and salt test respectively (including measurements with high uncertainty). The resulting uncertainties as well as the phase angle for the different setups is summarized in Table F-10: for the water test a mean phase angle uncertainty $\sigma_{\bar{\varphi},m} = \pm 0.12°$ and for the Solar Salt test a mean phase angle uncertainty $\sigma_{\bar{\varphi},m} = \pm 0.2°$ is assumed.

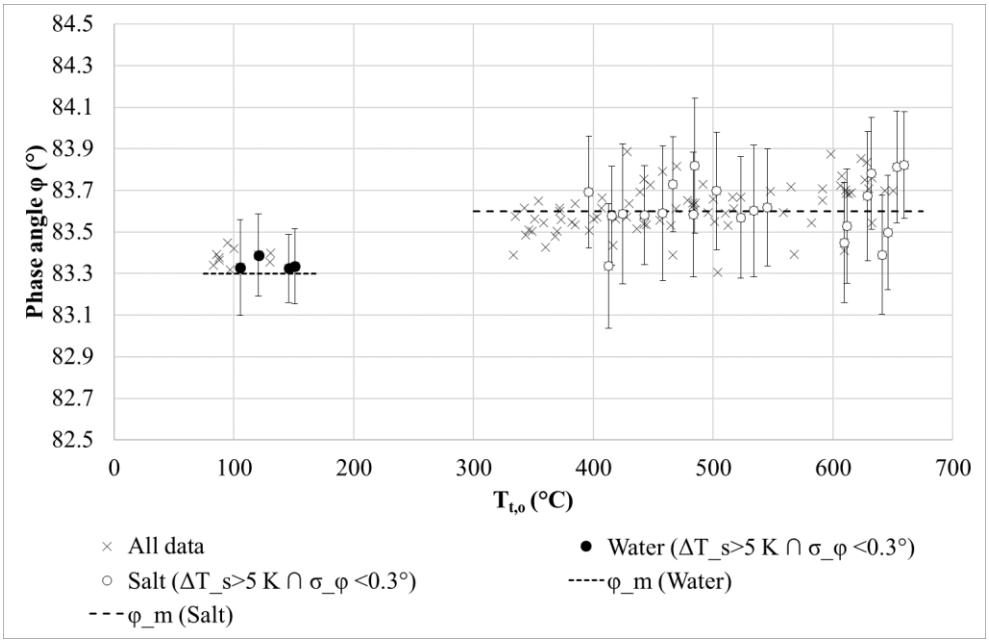


Figure F-9: Phase angle as a function of tube outer wall temperature

| **Measurement setup** | $\boldsymbol{\sigma_{\bar{\varphi},m}}$ | $\boldsymbol{\sigma_{\bar{\varphi},temperature}}$ | $\boldsymbol{\sigma_{\varphi,read}}$ | $\boldsymbol{\bar{\varphi}}$ |
|---|---|---|---|---|
| Water | $\sigma_{\bar{\varphi},m} = 0.10°$ | $\sigma_{\bar{\varphi},temperature} = 0.06°$ | $\sigma_{\varphi,read} \approx 0.02°$ | $\bar{\varphi} = 83.3 \pm 0.12°$ |
| Solar Salt | $\sigma_{\bar{\varphi},m} = 0.07°$ | $\sigma_{\bar{\varphi},temperature} = 0.17°$ | $\sigma_{\varphi,read} \approx 0.02°$ | $\bar{\varphi} = 83.6 \pm 0.2°$ |

Table F-10: Summary of assumptions for the phase angle

# G. Additional calculations

In this appendix chapter several additional calculations are summarized, such as the impact of the heating of the Solar Salt and water in the test section through induction heating, the impact of transient heat conduction and the deduction of peripheral pressure difference.

## G.1. Heating of the Solar Salt and water in the test section through induction heating

Solar Salt is a poor electrical conductor – although much better than water – compared to the test tube. Also, no pronounced magnetic behavior is known for Solar Salt or water (i.e., $\mu_r = 1$ is assumed). The power induced in a non-magnetic cylinder by the sinusoidal electromagnetic field created by solenoid coil can be evaluated using the following formula [24]:

$$P_{s,el} = \mu_0 \mu_r \pi f \left(l_{heat} \pi r_i^2\right) H^2 p$$

Where $H$ is the applied magnetic field strength and $p$ can be extracted from Figure G-2 [24]. Table G-1 summarizes the taken assumptions and results. As the ratio $d_i/\delta$ is close to zero, the resulting active power in the salt or in the water is approximately zero and can be neglected in the calculations.

| **Temperature salt** | **20°C** | **300 °C** | **565 °C** |
|---|---|---|---|
| Fluid | Water | Solar Salt | Solar Salt |
| Relative Magnetic permeability Fluid | 1 | 1 | 1 |
| Frequency $f$ of AC current in solenoid | 8600 Hz | 8600 Hz | 8600 Hz |
| Electrical resistivity of Fluid (see chapter 3.5) | 100 Ωm | 1.4e-2 Ωm | 5.5e-3 Ωm |
| Penetration depth in a semi-infinite body $\delta$ | 54000 mm | 633 mm | 403 mm |
| $d_i/\delta$ | 0.00 | 0.04 | 0.06 |
| p (from Figure G-2) | ≈0 | ≈0 | ≈0 |
| q (from Figure G-2) | ≈1 | ≈1 | ≈1 |
| $P_{s,el}$ | ≈0 | ≈0 | ≈0 |

Table G-1: Deduction of expected active power induced in the Solar Salt

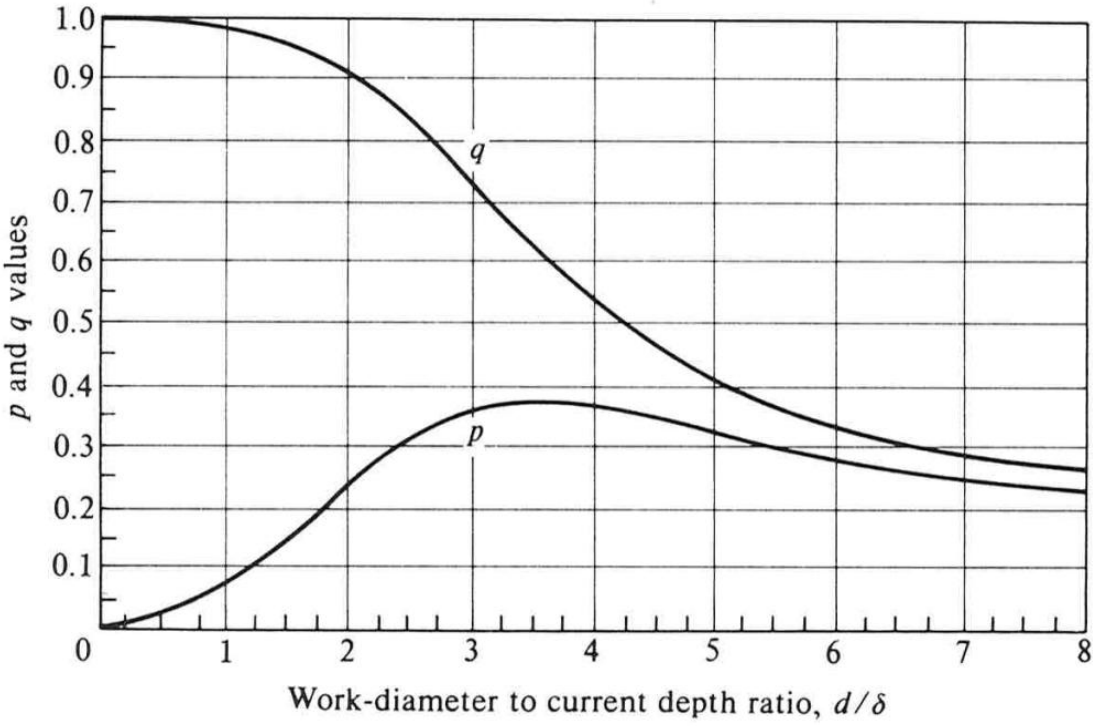


Figure G-2: p and q functions for a solid cylinder [24]

## G.2. Impact of Transient Heat Conduction

In the salt setup, the test section temperature is homogenized during several hours prior to the beginning of the actual test. In the following section, the required homogenization time prior to testing when starting from ambient temperature and the impact of a fluid temperature variation are evaluated and discussed. For this purpose, a transient thermal FEM model of the tube and insulation is set up. A convective heat transfer boundary condition assuming salt fluid temperatures is applied on the inner side of the tube and a convective heat transfer condition is applied on the outer surface of the insulation ($T_\infty = 20\ °C, \alpha_\infty = 7\ W/m^2/K$). In the first case, an initial temperature of the tube and insulation of 20 °C, with salt flow occurring from t=0 s at 560 °C and a convective heat transfer of 25000 W/m²/K (approx. maximum measured heat transfer coefficient) is assumed. In the second case a temperature step from 510 °C to 560 °C of the salt temperature is applied on a stationary temperature profile of insulation and tube. Figure G-3 shows on the left the transient response of the tube inner and outer tube wall ($T_{t,i}, T_{t,o}$) over time for the case of heating the setup from room temperature to 560 °C. The tube temperature assumes values close to the salt temperature a few seconds after starting of flow, while the temperature profile in the insulation is developed over a time scale of more than 16 hours. The right graph shows the results for a salt temperature step of 50 K at t=1 s. After less than ten seconds of flow 560 °C, the tube wall temperatures converge towards the novel salt temperature.

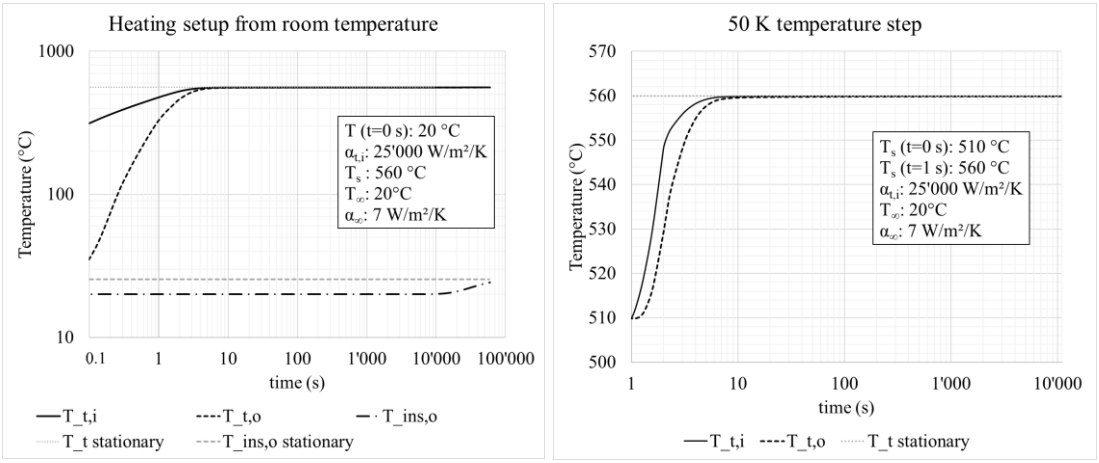


Figure G-3: Results of transient thermal FEM simulation of inner (T_t,i) and outer tube wall temperature (T_t,o) of the test section and outer insulation temperature (T_ins,o) as a function of time since start of salt flow at $T_s$: 560 °C (left) and after a 50 K temperature step (right)

Figure G-4 (left) shows on the left y-axis the heat losses through the tube and insulation as a function of time. In a stationary state, total heat losses of 220 W are expected through the insulation over the test section in this case. In the first seconds after start of flow, the heat losses decrease exponentially. The higher heat losses in the first few seconds of flow are caused by the heating of the metallic tube of the test section, which exposes a moderate Biot-number (Bi≈3) and a relatively high thermal diffusivity (a≈6 mm²/s). After heating of the tube wall, the thermal losses are limited by the low thermal diffusivity (a≈0.4 mm²/s) of the thermal insulation. After roughly three minutes of flow, the heat flow to the insulation are lower than 1000 W and decrease to values close to 220 W over the course of 16 hours. At a mass flow of 0.5 kg/s of fluid, this would translate to a change in temperature gradient between salt inlet and salt outlet from 1.3 K (at 1000 W) to 0.3 K (at 220 W) over the course of 16 hours. Figure G-4 shows on the right y-axis the rate at which the gradient between salt inlet and outlet temperature changes based on the calculated heat losses. It can be seen that after roughly two hours, the expected change in salt inlet to outlet temperature caused by the not yet developed thermal profile in the insulation is less than 0.001 K/min. For a test duration of one hour, this would lead to a total expected change in temperature difference of less than 0.06 K and can be neglected for the measurements. In the case of the temperature step (Figure G-4 right graph), values below 0.001 K/min are found after roughly 17 minutes. For lower fluid temperature and heat transfer cases, these times would be even lower, as on the one hand, the total thermal losses are lower and hence, the impact on the temperature gradient between inlet and outlet is reduced. On the other hand, the thermal equilibrium in the insulation is achieved after a shorter time span. Because of the large salt volume of the salt tanks, the temperature variation of salt inlet temperature will be far below 5 K. Consequently, an initial heating time of at least 8 hours is assumed. Furthermore, a homogenization time of at least 20 minutes is advised after a temperature step. For the salt tests an initial homogenization time of 60 minutes is selected.

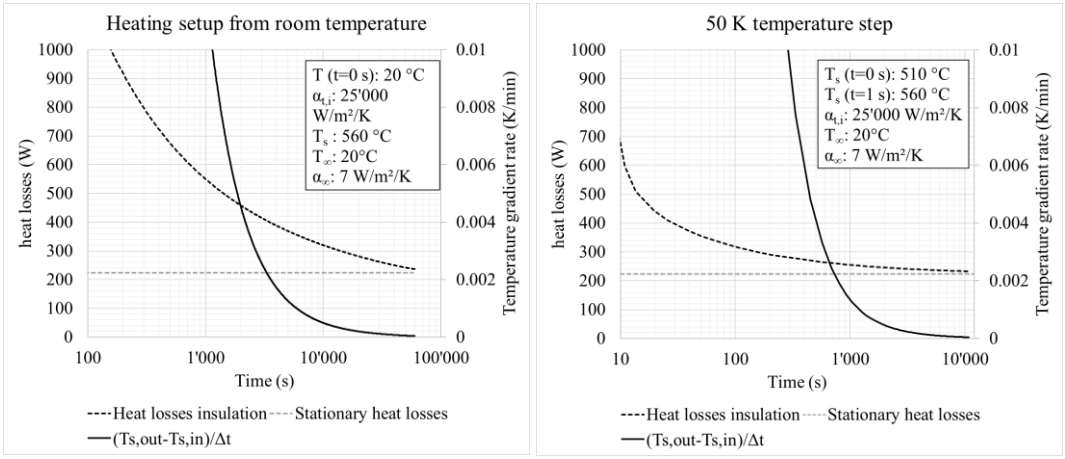


Figure G-4: Results of transient thermal FEM simulation of heat losses to ambient and temperature gradient rate as a function of time since start of salt flow at $T_s$: 560 °C (left) and after a 50 K temperature step (right)

## G.3. Deduction of Peripheral Pressure Difference $\Delta p_{per}$

The pressure difference measurement registers not only the pressure difference between the inlet and outlet of the test tube, but the section in between includes several additional components:

- 10.7 m of DN50 smooth tubing: $\Delta p_{DN50}$
- 505 mm of DN40 smooth tubing: $\Delta p_{DN40}$
- Static mixers inlet and outlet test section: $\Delta p_{static\ mix.}$
- Two Reducers from DN50 to DN40: $\Delta p_{DN50 \leftrightarrow DN40}$
- Two Reducers from DN50 to DN20: $\Delta p_{DN50 \leftrightarrow DN20}$
- Two 90° elbows (DN50): $\Delta p_{90°}$
- 0.45 m of vertical height difference between inlet and outlet: $\Delta p_{\Delta h}$

$\Delta p_{per}$ is the sum of pressure difference of all peripheral components listed above:

$$\Delta p_{per} = \Delta p_{DN50} + \Delta p_{DN40} + \Delta p_{static\ mix.} + \Delta p_{DN50-DN40} + \Delta p_{DN50-DN20} + \Delta p_{90°} + \Delta p_{\Delta h}$$

In a first step, the possible range of $\Delta p_{per}$ has to be deduced. For this purpose, the expected pressure difference of all components is calculated assuming in the first calculation optimistic properties and in the second calculation the most pessimistic properties for the pressure difference in each peripheral component. For this purpose, the general equation (G.1) is assumed. Table G-5 summarizes the assumptions for both the optimistic and the conservative calculation of pressure difference of all other pressure differences other than the test tube.

$$\Delta p = \zeta \cdot a \frac{\rho_{salt} u^2}{2} \tag{G.1}$$

| | **Optimistic assumptions** | **Conservative assumptions** |
|---|---|---|
| DN50 smooth tubing: $\Delta p_{DN50}$ | Smooth tube, Re ≈ 5000 -125000. Friction factor according to Blasius: $\zeta = \frac{0.3164}{\sqrt[4]{Re}}$ | Absolute roughness K=0.1 mm<br>(seamless steel tube, new)<br>friction factor calculated according to VDI heat atlas Lab2, formula (10) (Nikuradse, Prandtl, Karman, Moody, Colebrook) |
| DN40 smooth tubing: $\Delta p_{DN40}$ | Same as for $\Delta p_{DN50}$, Re≈ 6000 -155000 | Same as for $\Delta p_{DN50}$ |
| Static mixers inlet and outlet test section: $\Delta p_{static\ mix.}$ | Expected pressure drop specified by manufacturer for inlet and outlet static mixer as a function of flow velocity. A fitting curve is applied to deduce a correlation of the form $\zeta \cdot a = f(u_s)$:<br>Inlet static mixer: $\zeta \cdot a = 1.59428 \cdot u_s^2 - 5.36477 \cdot u_s + 10.8218$<br>Outlet static mixer: $\zeta \cdot a = 7.17169 \cdot u_s^2 - 23.8790 \cdot u_s + 38.2110$ | |
| Two Reducers from DN50 to DN40: $\Delta p_{DN50 \leftrightarrow DN40}$ | Continuous narrowing: $\zeta \cdot a$=0.04<br>Continuous extension:<br>$\zeta \cdot a = \zeta' \left(1 - \frac{r_1^2}{r_2^2}\right)^2 = 0.35 \cdot \left(1 - \frac{r_1^2}{r_2^2}\right)^2 = 0.05$ | Continuous narrowing: $\zeta \cdot a$=0.04<br>Continuous extension:<br>$\zeta \cdot a = \zeta' \left(1 - \frac{r_1^2}{r_2^2}\right)^2 = 0.45 \cdot \left(1 - \frac{r_1^2}{r_2^2}\right)^2 = 0.06$ |
| Two Reducers from DN50 to DN20: $\Delta p_{DN50 \leftrightarrow DN20}$ | Continuous narrowing: $\zeta \cdot a$=0.04<br>Continuous extension:<br>$\zeta \cdot a = \zeta' \left(1 - \frac{r_1^2}{r_2^2}\right)^2 0.35 \cdot \left(1 - \frac{r_1^2}{r_2^2}\right)^2 = 0.23$ | Continuous narrowing: $\zeta \cdot a$=0.04<br>Continuous extension:<br>$\zeta \cdot a = \zeta' \left(1 - \frac{r_1^2}{r_2^2}\right)^2 0.45 \cdot \left(1 - \frac{r_1^2}{r_2^2}\right)^2 = 0.30$ |
| Two 90° elbows (DN50): $\Delta p_{90°}$ | Smooth 90° elbow: $\zeta \cdot a = 0.1$ | 90° elbow high roughness: $\zeta \cdot a = 0.3$ |

Table G-5: Assumptions for optimistic and conservative peripheral pressure drop [19]

The calculation of the individual components of the peripheral pressure difference shows that for low salt velocities (< 1 m/s) the hydrostatic pressure clearly dominates the calculated pressure difference (>80%). For higher salt velocities (3 m/s), the pressure drop caused by the static mixers and the reducers (DN50 to DN20) is the largest contributor to the overall pressure difference (~ 53 to 70%). Figure G-6 shows the ratio of the sum of pressure difference of all peripheral components $\Delta p_{per}$ on the measured pressure difference $\Delta p_{s,total}$. For flow velocities larger than 3 m/s the peripheral components account for roughly 50 to 75% of the measured pressure difference.

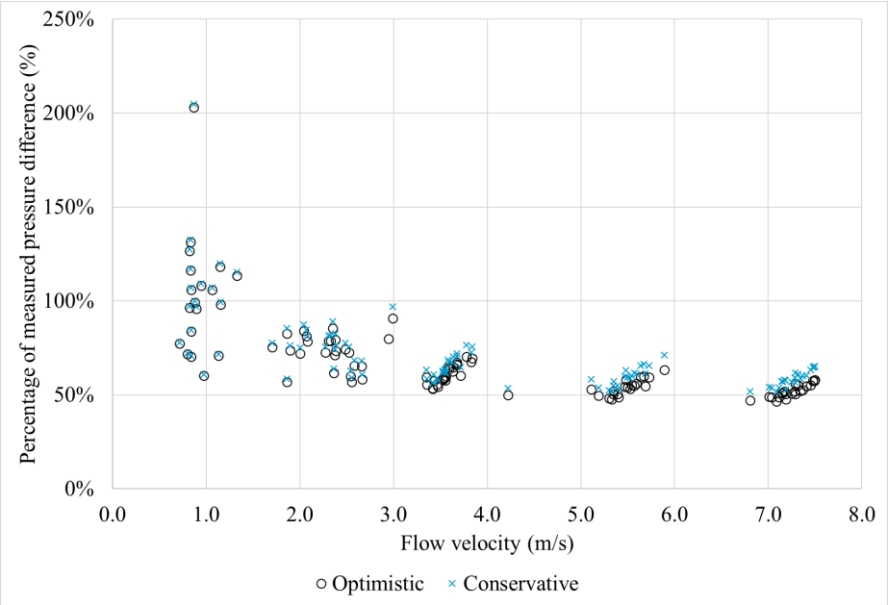


Figure G-6: Proportion of $\Delta p_{per}$ on total measured pressure difference $\Delta p_{s,total}$

The calculated relative deviation between the pressure difference with optimistic assumptions and conservative assumptions is shown in Figure G-7. The deviation between the two assumptions ranges between <1% and 14% of the calculated mean peripheral pressure difference. The uncertainty of the peripheral pressure drop calculation is defined as the difference between the calculated pressure difference using conservative and optimistic assumptions: $\sigma_{\Delta p_{per}} = \Delta p_{per,cons} - \Delta p_{per,optim}$. The peripheral pressure difference is defined as the mean average of the two assumptions: $\Delta p_{per} = 0.5\left(\Delta p_{per,cons} + \Delta p_{per,optim}\right)$.

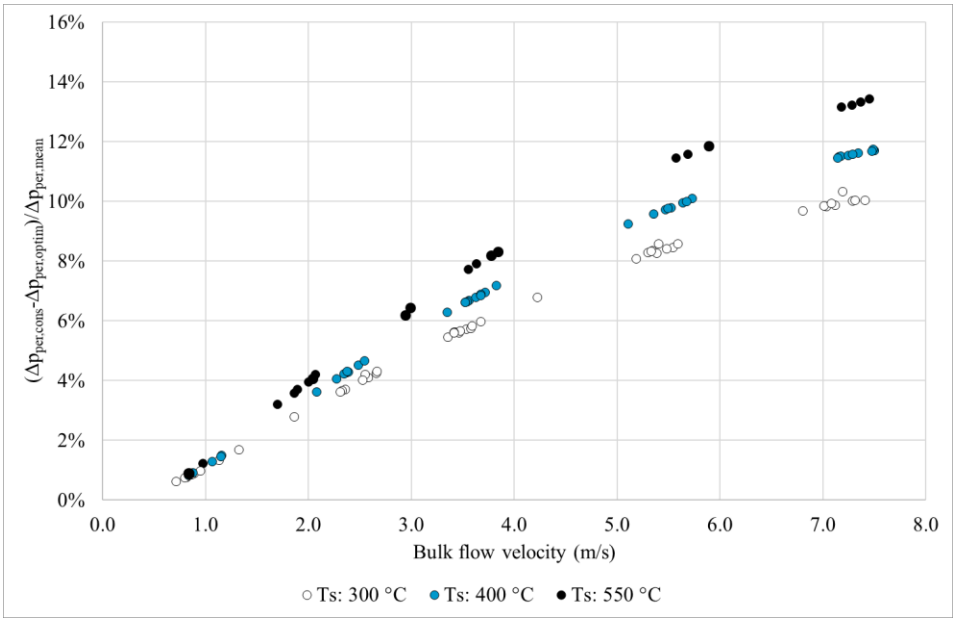


Figure G-7: Relative deviation between the calculated pressure difference assuming optimistic and conservative assumptions as a function of bulk flow velocity and salt temperature